

**LOW TEMPERATURE AQUEOUS SYNTHESIS OF ZnO
NANORODS AND COATING OF Au ON ZnO FOR ENHANCED
RAMAN SPECTROSCOPY STUDIES**

By

Marcia del Rocío Balaguera-Gelves,

A dissertation submitted in partial fulfillment of the requirements for the degree of

DOCTOR OF PHILOSOPHY

in

Applied Chemistry
(Chemistry of Materials)

UNIVERSITY OF PUERTO RICO

MAYAGÜEZ CAMPUS

2013

Approved by:

Samuel P. Hernández Rivera, Ph.D.
President, Graduate Committee

Date

Oscar Perales-Pérez, Ph.D.
Member, Graduate Committee

Date

Jessica Torres, Ph.D.
Member, Graduate Committee

Date

Julio G. Briano-Peralta, Ph.D.
Member, Graduate Committee

Date

Ana J. Navarro-Rodríguez, Ph.D.
Representative of the Office of Graduate Studies

Date

René Vieta, Ph.D.
Chairperson of the Chemistry Department

Date

ABSTRACT

This thesis reports results on the growth-controlled synthesis of zinc oxide nanorods (ZnO NRs) in aqueous phase has been investigated. ZnO NRs were grown on ZnO films previously deposited onto Si (100) and indium tin oxide (ITO) substrates by RF magnetron sputtering. The formation of the rods took place in the presence of hexamethylenetetramine (HMT) as habit-controller reagent. The grains in the base ZnO film acted as seeds that promoted the longitudinal growth of the oxide. As-synthesized base films and rods were characterized by X-ray diffraction, scanning electron microscopy (SEM), field emission SEM, optical absorption, and photoluminescence spectroscopy techniques. The rod thickness was controlled by adjusting in deposited using RF magnetron sputtering parameters such as temperature, and reaction time and afterwards, a wet chemistry procedure was performed for ZnO NRs growth. The precise control of the synthesis conditions was conducive to the formation of ZnO NRs of a relatively narrow distribution of diameters (60-70 nm) with lengths in the 1-3 μm range. ZnO NRs/ZnO base film/ITO exhibits a strong UV absorption around 360 nm. Photoluminescence spectra presented narrow near-band-edge (NBE) dominant peak indicate with a relatively higher oxygen vacancy concentration in the ZnO- NRs grown on ZnO/ITO in comparison with those on the ZnO/Si (100).

The other hands a second goal, was focused in the optimization of conditions to control of Ion beam and UV process for coating the ZnO NRs with gold (Au). Au-coated ZnO NRs were characterized using X-ray diffraction, EDS and field emission scanning electron microscopy (FE-SEM). Au coated/ZnO NRs were developed for the identification to trace levels by surface-enhanced Raman scattering SERS of adenine, 4-nitrobenzenethiol and 2, 4-aminobenznethiol (ABT) and 1, 3, 5-trinitroperhydro-1, 3, 5-triazine (RDX) with a detection limits down in orders of picograms.

Zinc oxide (ZnO) was first deposited using RF magnetron sputtering, and afterwards, a wet chemistry procedure was performed for ZnO NRs growth. Ion beam and UV process were used for coating the ZnO NRs with gold (Au). Au coating on ZnO

NRs were used to evaluate the detection capability by SERS with different analytes. Au-coated ZnO NRs were characterized using X-ray diffraction, EDS and field emission scanning electron microscopy (FE-SEM). Ultraviolet photo-reduction showed a higher SERS than the ion beam method. This Au coating on ZnO NRs could successfully detect analytes such as: adenine, 4-nitrobenzenethiol and 4-aminobenzethiol (4-ABT) and 1, 3, 5-trinitroperhydro-1, 3, 5-triazine (RDX) at low levels. Strong SERS spectrum of Raman was observed for 4-ABT.

ZnO NRs/ZnO base film/ITO was SERS active from a laser wavelength at 785 nm. Therefore, the intensities were normalized to laser power and acquisition time with final units of $\text{counts}\cdot\text{mW}^{-1}\text{s}^{-1}$ at 1076 cm^{-1} . A limit of detection (LOD) of $1\times 10^{-8}\text{ M}$ for ABT was achieved corresponding to a minimum of 5.4×10^5 molecules detected under the experimental conditions at excitation wavelength of 785 nm with a sensitivity of the ZnO NRs in the range of 11 femtogram under laser spot, with a SEF of 7.54×10^8 . Chemical and electromagnetic effects can contribute a high SERS enhancements factor for Au coated ZnO NRs. Results shown here demonstrate a good reproducibility expressed as relative standard deviation 11.8 % for Au coated ZnO NRs/ZnO base film/ITO.

Our studies have demonstrated that these Au-coated nanostructures are highly stable and reproducible and allow for the detection of explosives such as RDX. In addition, our modification of Vayssieres' method has proven its versatility as it has been successfully applied in the preparation of a biosensor for urea.

RESUMEN

Esta disertación muestra los resultados obtenidos en la síntesis de crecimiento controlado de nanobarras (ZnO NRs por sus siglas en inglés) en fase acuosa. Las ZnO NRs crecieron sobre películas de ZnO previamente depositadas sobre sustratos de Si (100) y óxido de indio estaño (ITO) mediante pulverización catódica de RF. La formación de las barras se llevó a cabo en presencia de hexametileno tetraamina (HMT) como reactivo controlador de ambiente. Los granos en la base de la película de ZnO actuaron como semillas que promovieron el crecimiento longitudinal del óxido. Las películas de base sintetizadas fueron caracterizadas por técnicas de difracción de rayos X, microscopía electrónica de barrido (SEM), SEM de emisión de campo (FE-SEM), absorción óptica, y espectroscopía de fotoluminiscencia. El grosor de las barras fue controlada ajustando los parámetros de la pulverización catódica de RF durante la deposición tales como temperatura y tiempo de reacción. Posteriormente, un procedimiento químico se llevó a cabo para el crecimiento de las ZnO NRs. El control preciso de las condiciones de la síntesis resultó en la formación de ZnO NRs con una distribución de diámetros en un intervalo relativamente estrecho (60-70 nm) con longitudes en un intervalo de 1-3 μm . ZnO NRs/ZnO película base/ITO exhibe una absorción fuerte en el espectro UV cerca de 360 nm. Los espectros de fotoluminiscencia presentaron un pico dominante estrecho en el borde de banda cercana (NBE) indicativo de una concentración de vacancias de oxígeno relativamente altas en ZnO NRs crecidos sobre ZnO/ITO en comparación con aquellos crecidos sobre ZnO/Si (100).

Por otro lado, un segundo objetivo se enfocó en la optimización de condiciones para controlar los procesos de haz de iones y UV para recubrir los ZnO NRs con oro (Au). Los ZnO NRs recubiertos con Au fueron caracterizados usando difracción de rayos X, EDS y SEM de emisión de campo (FE-SEM). Las ZnO NRs recubiertos con Au fueron desarrollados para la identificación a nivel de trazas por dispersión Raman mejorada por la superficie (SERS) de adenina, 4-nitrobencenotiol, 2, 4-aminobencenotiol (4-ABT) y 1, 3, 5-trinitroperhidro-1, 3, 5-triazina (RDX) con un límite de detección en el orden de femtogramos.

El óxido de zinc fue primero depositado usando pulverización catódica de RF y luego se obtuvo el crecimiento de las ZnO NRs usando un procedimiento químico. Procesos de haz de iones y UV fueron utilizados para recubrir las ZnO NRs con oro. El recubrimiento con Au de las ZnONRs fue utilizado para evaluar la capacidad de detección por SERS de diversos analitos. Las ZnO NRs recubiertas con Au fueron caracterizadas usando difracción de rayos X, EDS y FE-SEM. Fotoreducción con radiación UV mostró un mayor efecto SERS que el método de haz de iones. Con este recubrimiento con Au de las ZnO NRs se pudo detectar exitosamente analitos tales como adenina, 4-nitrobenzenotiol, 4-aminobenzenotiol (4-ABT) y 1, 3, 5-trinitroperhidro-1, 3, 5-triazina (RDX) a bajos niveles. Se observó un fuerte espectro SERS para 4-ABT.

Las ZnO NRs/ZnO película base/ITO fueron activas en SERS a una longitud de onda de láser de 785 nm. Por lo tanto, las intensidades fueron normalizadas a la potencia del láser y el tiempo de adquisición tiene unidades finales de conteos·mW⁻¹s⁻¹ a 1076 cm⁻¹. Se obtuvo un límite de detección (LOD) de 1x10⁻⁸ M para 4-ABT que corresponde a un mínimo de 5.4 X10⁵ moléculas detectadas bajo las condiciones experimentales a longitudes de excitación de 785 nm con sensibilidad de las ZnO NRs en el intervalo de 11 femtogram bajo el punto láser, con un factor de mejoramiento de superficie (SEF) de 7.54 x10⁸. Efectos químicos y electromagnéticos pueden contribuir a un mayor factor de mejoramiento SERS para las ZnO NRs recubiertas con Au. Nuestros resultados demuestran buena reproducibilidad expresada en términos de una desviación estándar relativa de 10.8 % para las ZnO NRs/ZnO película base/ITO recubiertas de Au.

Nuestros estudios han demostrado que estas nanoestructuras recubiertas de oro (Au) son altamente estables, reproducibles y permiten la detección de explosivos tales como RDX. En adición, nuestra modificación del método de Vayssieres ha comprobado su versatilidad pues se ha aplicado exitosamente en la preparación de un biosensor de urea.

Copyright © by
Marcia del Rocío Balaguera Gelves
2013

To God, my mother Nohemy Gelves Jaimes and my family.

ACKNOWLEDGEMENTS

I thank God who gave me the hope, faith and love to breathe every day and for everything you have done for me.

I would like to express my gratitude to all of whom directly or indirectly contributed to my research during my graduate studies. I have to say that the timely completion of this project would not be possible without them. First of all, I want to sincerely acknowledge my advisor Dr. Samuel P. Hernández-Rivera for allowing me to conduct research under his supervision in his laboratory. He has given me continuous support and guidance, and has directed my career as a researcher. Special thanks I owe to Dr. Oscar Perales for experimental support on ZnO studies, for his boundless patience and constant encouragement. He has been a great guiding force during my research.

I would also like to extend my appreciation to my graduate committee members, Dr. Julio Briano, and Dr. Jessica Torres for being part of my formation process and for their collaboration in the development of this research.

I am grateful to the University of Puerto Rico, Mayagüez Campus, and the Chemistry Department, for giving me the opportunity to complete my PhD degree. Thanks to the professors who contributed to my professional formation Dr. Louisa Hope-Week of Texas Tech University for the opportunity to do research in her lab in the summer of 2009. Also I want to say thanks for the acquired research experience and the opportunity during the summer of 2010 in the lab of Dr. Shekhar Bhansali and Dr. Sunil Arya from Department of Electrical Engineering, University of South Florida, Tampa.

I would like to express my gratitude to J. Ortega and G. Cruz from Chemical Lab of Hewlett Packard-PR for FE-SEM spectra and B. Renteria from NANO-Materials Processing Lab for XRD spectra. I thank Dr. Jose. A. Jiménez and M. Sendova for the

photoluminescence spectra at Optical Spectroscopy and Nano-Materials Lab at New College of Florida, Sarasota, FL.

To my family, my mother Nohemy Gelves, my sister Jacqueline, my brothers, for their understanding and their support all these years. Also to my nieces: Julieth Tatiana and Mónica Dahiana Ariza Balaguera.

Thanks to my friends: Dr. Luis A. Morell, Xiomy Narvaez, Jari Cabarcas, Jackeline Indira Jerez, Amanda Charris, Edwin de la Cruz and Sandra Loydover Peña for their friendship and help.

This work was conducted in collaboration with the Center for Chemical Sensors Development of the University of Puerto Rico–Mayagüez sponsored by the Department of Defense. This work was supported by the U.S. Department of Defense, University Research Initiative Multidisciplinary University Research Initiative (URI-MURI) Program, under grant number: DAAD19-02-1-0257. The U.S. DHS under Award Number 2008-ST-061ED0001 also supported this project.

Finally, I would like to acknowledge the University of Puerto Rico, Mayagüez Campus and Department of Chemistry for the opportunity to study in Puerto Rico.

TABLE OF CONTENTS

ABSTRACT	II
RESUMEN	IV
ACKNOWLEDGEMENTS	VIII
LIST OF FIGURES	XIII
LIST OF TABLES	XVIII
CHAPTER 1: INTRODUCTION	1
1.1 JUSTIFICATION	1
1.2 OBJECTIVES	4
1.2.1 MAIN OBJECTIVE	4
1.2.2 SPECIFIC OBJECTIVES.....	5
1.3 DISSERTATION CONTENTS.....	5
CHAPTER 2: BACKGROUND.....	6
2.1 PHYSICAL PROPERTIES OF ZINC OXIDE	6
2.1.1 CRYSTAL STRUCTURE OF ZINC OXIDE	6
2.1.2 TYPICAL GROWTH STRUCTURES OF ZNO	8
2.1.3 ELECTRONIC BAND STRUCTURE OF ZNO	9
2.1.4 PHOTOLUMINISCENCE (PL)	11
2.2 TECHNIQUES OF DEPOSITION OF ZNO.....	13
2.2.1 MAGNETRON SPUTTERING (MS).....	13
2.2.2. PLASMA-ENHANCED METAL -ORGANIC CHEMICAL VAPOR DEPOSITION (PEMOCVD)	15
2.3 SYNTHESIS OF ZNO NANOSTRUCTURES	17
2.3.1 VAPOR TRANSPORT SYNTHESIS	17
2.3.2 METAL CATALYST.....	18
2.3.2 ELECTRON-BEAM LITHOGRAPHY	21
2.4 OPTICAL PROPERTIES OF METALLIC GOLD NANOSTRUCTURES	23
CHAPTER 3: LITERATURE REVIEW.....	25
CHAPTER 4: METHODOLOGY	30
4.1 EXPERIMENTAL PROCEDURES	30
4.1.1 MATERIALS.....	30
4.1.2 PREPARATION OF SUBSTRATES	30
4.1.3 SYNTHESIS OF ZNO BASE FILMS	30
4.1.4 SYNTHESIS OF ZNO NRs.....	31
4.2 MATERIAL CHARACTERIZATIONS	33
4.2.1 X-RAY DIFFRACTOMETRY (XRD)	33
4.2.3 ABSORPTION SPECTROSCOPY	36
4.2.4 PHOTOLUMINESCENCE	38
4.2.5 SERS AND RAMAN SPECTROMETRY	39
5 RESULTS AND DISCUSSION.....	40
5.1 OPTIMIZATION OF SYNTHESIS PARAMETERS	40
5.2 DEPOSITION ON SUBSTRATE	40

5.3 ZnO NRs FORMATION AT TEMPERATURES BELOW 200 °C	41
5.4 SONICATION TREATMENT FOR UNIFORMITY OF FILMS.	42
5.5 ZnO BASE FILM/ITO	42
5.5.1 EFFECT OF TEMPERATURE ON THE DEPOSITION OF ZnO BASE FILM/ ITO BY SPUTTERING	42
A. XRD ANALYSES	42
B. FIELD EMISSION SEM ANALYSES	44
5.6 EFFECT OF DEPOSITION TIME ON ZnO BASE FILM/ITO BY SPUTTERING	45
A. XRD ANALYSES	45
B. FIELD EMISSION SEM ANALYSES	47
5.7 ZnO BASE FILM/ Si (100)	48
5.7.1 EFFECT OF TEMPERATURE TREATMENT ON PHASE DEPOSITION OF ZnO BASE FILM/ Si (100) BY SPUTTERING.	48
A. XRD ANALYSES	48
B. FIELD EMISSION SEM ANALYSES	49
5.8 EFFECT OF DEPOSITION TIME ON ZnO BASE FILM/Si (100) BY SPUTTERING.....	50
5.9 ZnO NRs/ ZnO BASE FILM/ITO	50
5.9.1 EFFECT OF TEMPERATURE TREATMENT ON GROWTH OF ZnO NRs DEPOSITED ON ZnO BASE FILM/ ITO BY MAGNETRON SPUTTERING.	50
A. XRD ANALYSES	50
B. FIELD EMISSION SEM ANALYSES	51
5.10 EFFECT OF DEPOSITION TIME ON ZnO BASE FILM/ ITO BY SPUTTERING ON THE GROWTH OF ZnO NRs	52
5.11. ZnO RODS DEPOSITED ONTO ZnO BASE FILM/Si (100).....	53
5.11.1 EFFECT OF TEMPERATURE TREATMENT OF ZnO BASE FILM/Si(100) ON THE GROWTH OF ZnO NRs.	53
A. XRD ANALYSES	53
B. FIELD EMISSION SEM ANALYSES	54
5.12 OPTIMUM CONDITIONS FOR GROWTH OF ZnO RODS.	55
5.13 STRUCTURAL CHARACTERIZATION OF ZnO RODS DEPOSITED ONTO ZnO BASE FILM /ITO SUBSTRATES.....	55
5.13.1 XRD ANALYSES	55
5.13.2 UV-VIS ABSORPTION.....	57
5.13.3 PL MEASUREMENTS	58
5.14 STRUCTURE AND CHARACTERIZATION OF ZnO NRs DEPOSITED ONTO ZnO/Si (100) SUBSTRATES UNDER OPTIMIZED CONDITIONS.	59
5.14.1 XRD ANALYSES	59
5.14.2 UV-VIS ABSORPTION.....	61
5.14.3 PL MEASUREMENTS	61
5.15 COMPARATIVE MORPHOLOGICAL ANALYSES FOR ZnO-NRs DEPOSITED ON ZnO/Si (100) AND ZnO/ITO	62
5.16 VARIATION OF THE MOLAR CONCENTRATION OF HMT AND Zn (NO ₃) ₂	65
5.17 VARIATION OF REACTION TIME ON THE GROWTH OF ZnO NRs.	67

5.18 CONCLUSIONS	70
5.19 ZNO NANORODS COATED WITH AU FOR ENHANCED RAMAN SPECTROSCOPY	72
5.19.1 OPTIMIZATION OF SYNTHESIS OF ZNO NRs COATED WITH AU	72
5.19.2 INTRODUCTION.....	72
5.20 EXPERIMENTAL	74
5.20.1 MATERIALS AND METHODS	74
5.20.2 SYNTHESIS OF AU COATING ON ZNO NRs.	75
5.20.3 NORMAL RAMAN AND SERS EXPERIMENTS	76
5.20.4 SAMPLE PREPARATION FOR ANALYSIS BY SERS.....	76
5.20.5 RESULTS AND DISCUSSION	76
5.21 SURFACE ENHANCED RAMAN SPECTROSCOPY	81
5.22 CONCLUSIONS	89
CHAPTER 6: FUTURE WORKS.....	91
CHAPTER 7: GENERAL REFERENCES	92
APPENDIX A: SENSITIVITY CALCULATION FOR AU COATING ZNO NRS/ZNO BASE FILM/SI	105
APPENDIX B: SEF VALUES FOR AU COATING ZNO NRs/ZNO BASE FILM/SI (100).....	106
APPENDIX CHAPTER 8: GOLD-COATED SILICA NANOWIRES FOR IMMUNOASSAY BASED ON SURFACE ENHANCED RAMAN SPECTROSCOPY	107
MARCIA BALAGUERA-GELVES ^A OSCAR PERALES-PÉREZ ^B , SURINDER SINGH ^B , SUNIL K. ARYA ^C , SHEKHAR BHANSALI ^C , EDUARDO MURPHY-PÉREZ ^C AND SAMUEL P. HERNÁNDEZ-RIVERA ^{A,*}	107
8.1 ABSTRACT.....	107
8.2 INTRODUCTION.....	107
8.3 MATERIALS AND METHODS	111
8.4 RESULTS AND DISCUSSION	112
8.5 CONCLUSIONS	115
8.6 REFERENCES.....	116

List of Figures

Figure 1. ZnO crystal structures: (a) rocksalt , (b) zinc blende and (c) wurtzite [41].	7
Figure 2. The wurtzite crystal structure of ZnO with the lattice parameters a and c.....	7
Figure 3. Typical growth morphologies of one-dimensional ZnO nanostructures and the corresponding facets.	9
Figure 4. (a) Bulk band structure of ZnO for various high-symmetry lines in the irreducible part of the bulk Brillouin zone and density of states. The full line shows the total density of states and the dotted line gives the cation contribution to the DOS. [48]; (b) Splitting of the VB in hexagonal ZnO under the influence of crystal field and spin-orbit coupling. (The figure is not drawn to scale) [42].....	10
Figure 5. (a) Controlled synthesis of 6 nm wide ZnO nanobelts. (b) Photoluminescence spectra recorded from ZnO nanobelts with widths of 200 and 6 nm, respectively, showing a blue-shift with a reduction in nanobelt size [54].	12
Figure 6. (a) Schematic diagram of a magnetron-sputtering configuration for simultaneous rf and dc excitation [72] (b) Plasma as is used in magnetron sputtering.....	15
Figure 7. Schematic of the atmospheric plasma source and substrate holder.....	16
Figure 8. (a) A SEM micrograph of ZnO nanohelix structures grown via VS process. (b) A TEM image of ZnO nanobelt grown via VLS process. Inset: structure model of the nanobelt [81]. (c) Hierarchical ZnO nanostructures synthesized by vapor transport and condensation technique [89]. Scale bar: 10 μm . (d) Needle-like ZnO rods [95].....	18
Figure 9. (a) ZnO nanorods grown using gold as a catalyst. (b) An enlarged image of the nanorods, showing gold particles at the tips [99].	19
Figure 10. (a) An optical micrograph of the as-synthesized sample on a silicon substrate, showing two distinct products on the surface. The three circles indicate three TEM copper grids placed on the substrate for collecting samples (b), (c) SEM images recorded from the metallic lustre and white colour regions, presenting the formation of pure Zn nanobelts and ZnO nanobelts, respectively (d) XRD recorded from the metallic region, showing the formation of Zn nanobelts [100].	20
Figure 11. (a) Hexagonal ZnO nanowire array generated by lithographically patterned Au catalysts [102]. (b) Square ZnO nanowires array created using TEM grids [103]. (c) Hexagonal ZnO nanorod array with diameter ~ 60 nm and spacing ~ 110 nm (d) An enlarged hexagonal ZnO nanorod array [104].	22
Figure 12. Schematic diagram of a) Role HMT and b) Exposed to Zn ions	26
Figure 13. System used for ZnO NRs synthesis by wet chemistry method.....	32
Figure 14. Flow diagram from growth-controlled synthesis of ZnO-NRs in aqueous phase has been investigated. ZnO-NRs were grown on ZnO films previously deposited onto Si (100) and indium tin oxide (ITO) substrates by RF magnetron sputtering and then characterized by several techniques.....	32
Figure 15. Schematic diagram of Bragg's diffraction from a set of parallel planes[159].	34
Figure 16. Image of a Philips/ FEI, XL30s, FEG SEM / Phoenix EDAX located at the Lab of Hewlett Packard-PR – Aguadilla.	35
Figure 17. UV-vis spectrometer setup [158].....	37

Figure 18. Renishaw Raman Microspectrometer (RM2000) with Leica objectives with 10x magnification used.	39
Figure 19. FE-SEM images of ZnO NRs on Si (100) without using pre-synthesized ZnO base film by sputtering.	41
Figure 20. FE-SEM images of the solids synthesized by wet chemistry at 200 °C.	41
Figure 21. SEM image of ZnO rods deposited onto ZnO layer on Si (100) substrate. The rod synthesis temperature was 95 °C 7 hours: a) without sonication and b) sonicated.	42
Figure 22. XRD patterns for ZnO base films deposited by sputtering on 15-25 Ω/SQ2 ITO substrates at a) 200 °C, b) 120 °C and 10 min of deposition time.	43
Figure 23. FE-SEM images of the ZnO base film/ITO film deposited by RF magnetron sputtering for 10 min at a) 200 °C; b) 120 °C. Grain Size for the the ZnO base films was 220 nm (SD 105) for 200 °C and 65 nm (SD 24) for 120 °C.	45
Figure 24. XRD patterns of the ZnO NRs/ZnO base film/ITO film deposited by RF magnetron sputtering for 120 °C for: a) 10 min and b) 30 min.	46
Figure 25. FE-SEM images of the ZnO base film/ITO film deposited by RF magnetron sputtering at 120 °C for (a) 30 min and (b) 10 min. Grain Size for the the ZnO base films were 324.02 nm (SD 0.08 for 200 °C and 64.77 nm (SD 23.71) for 120 °C... ..	47
Figure 26. XRD patterns for ZnO base films deposited by sputtering on Si (100) substrates at: (a) 200 °C, (b) 120 °C and 10 min of deposition time in both samples.	48
Figure 27. FE-SEM images of the ZnO base film/ Si (100) film deposited by RF magnetron sputtering for 10 min at a) 200 °C and b) 120 °C. Grain size for the ZnO base films were 148.09 nm (SD 33.91) for 200 °C and 19.65 nm (SD 19.65) for 120 °C.	49
Figure 28. FE-SEM images of the ZnO base film/Si (100) film deposited by RF magnetron sputtering at 120 °C for: (a) 30 min; (b) 10 min. Grain Size for the the ZnO base films were 331 nm (SD 0.059) for 30 min and 20.91 nm (SD 4.73) for 120 °C for 10 min.	50
Figure 29. XRD patterns for ZnO NRs/ ZnO base films deposited by RF magnetron sputtering for 10 minutes at a) 200 °C b) 120 °C. Both samples of ZnO base film were used for the growth of ZnO NRs by wet chemistry, from starting equimolar (0.01M) aqueous solutions of Zn ²⁺ and HMT at 95 °C and 1.5 hours of reaction time.	51
Figure 30. FE-SEM images of the ZnO NRs used on ZnO base film/ITO film deposited by RF magnetron sputtering for 10 minutes a) 200 °C (b) 120 °C. Both samples of ZnO base film were used for the growth of ZnO NRs by wet chemistry, from starting equimolar (0.01M) aqueous solutions of Zn ²⁺ and HMT at 95 °C and 1.5 hours of reaction time. The estimated diameter for the the ZnO NR/ZnO base film/ITO were 95.46 nm (SD 30.02) and a length of 1.5 μm (396.87 nm) for 200 °C. Diameter size was 78.49 nm (SD 21.40 nm) with a length of (419.5) (SD 103.5 nm) for 120 °C.	52
Figure 31. FE-SEM arrays of ZnO NRs deposited onto ZnO base film/ITO film deposited by RF magnetron sputtering at 120 °C for a) 30 min and b) 10 min. Both samples of ZnO base film were used for the growth of ZnO NRs by wet chemistry, from starting equimolar (0.01M) aqueous solutions of Zn ²⁺ and HMT at 95 °C and 1.5 hours of reaction time. Diameter size for the the ZnONR/ ZnO base film/ITO were 19.65 nm (SD 0.058) and a length of 529 nm (SD 153 nm) for 10 min.	53

Figure 32. XRD patterns for ZnO NRs/ ZnO base films used on ZnO base film/Si (100) substrate deposited by RF magnetron sputtering for 10 minutes at (a) 200 °C (b) 120 °C. Both samples of ZnO base film were used for the growth of ZnO NRs by wet chemistry, from starting equimolar (0.01M) aqueous solutions of Zn ²⁺ and HMT at 95 °C and 1.5 hours of reaction time.	54
Figure 33. ZnO NRs/ ZnO base films used on ZnO base film/Si (100) substrate deposited by RF magnetron sputtering for 10 minutes at a) 200 °C b) 120 °C. Both samples of ZnO base film were used for the growth of ZnO NRs by wet chemistry, from starting equimolar (0.01M) aqueous solutions of Zn ²⁺ and HMT at 95 °C and 1.5 hours of reaction time. ZnO NRs obtained at 200 °C had thickness of around 150 nm and diameters of 124.73 nm (SD 31/78). Use of a temperature of 120 °C resulted in ZnO NRs with thickness of around 48 nm and diameters of 50.14 nm, (SD 16.37), length of 319.36 nm (SD 90.52 nm).....	55
Figure 34. XRD patterns for: (a) ZnO base films deposited by sputtering on 15-25 Ω/SQ2 ITO substrates at 120 °C, and 10 min of deposition time; (b) ZnO rod deposited from starting equimolar (0.01M) aqueous solutions of Zn ²⁺ and HMT at 95 °C after 1.5 hours of reaction time.	56
Figure 35. UV-VIS spectrum of ZnO rods deposited onto ZnO/ITO base film. The ZnO rods were grown using equimolar (0.01 M) aqueous solutions of Zn ²⁺ and HMT at 95 °C and 1.5 hours.....	58
Figure 36. PL spectrum for ZnO rods obtained at an excitation wavelength of 350 nm.	59
Figure 37. XRD patterns for: (a) ZnO/ Si (100) base film deposited by sputtering at 120 °C and 12 min of deposition time; (b) ZnO rods deposited onto the ZnO/Si base film. The ZnO rods were formed from equimolar (0.01 M) aqueous solutions of zinc nitrate and HMT at 95 °C and 1.5 hours of reaction time.	60
Figure 38. PL spectra for ZnO rods obtained at an excitation wavelength of 350 nm. a) ZnO rods deposited onto ZnO/Si and ZnO/ITO base film. In both cases ZnO rods were formed by the reaction of the following equimolar (0.01 M) aqueous solutions of Zn ²⁺ and HMT at 95 °C and 1.5 hours. b) Comparison of UV NBE emission band for ZnO rods deposited onto ZnO/Si and ZnO/ITO base film. A weak shoulder is discernible at 382 nm. c) GL band for ZnO rods deposited onto ZnO/Si and ZnO/ITO base film.	62
Figure 39. (a) FE-SEM images of the ZnO base film/Si (100) film deposited by RF magnetron sputtering for 10 min at 120°C. ZnO NRs obtained had thickness of around 20 nm and diameters of 19.85 nm (SD 4.85). (b) Magnification of (a).....	63
Figure 40. (a) FE-SEM images of the ZnO base film/ITO film deposited by RF magnetron sputtering for 10 min at 120°C. ZnO NRs obtained had diameter of around 64.77 nm (SD 23.71). (b) Magnification of (a).....	64
Figure 41. FE-SEM images of ZnO nanorods deposited onto a) ZnO/ Si (100) b) Magnification of a) c) ZnO/ ITO d) Magnification of c). Variation of the HMT and Zn(NO ₃) ₂ mol relation 1:1 at 0.01 M. ZnO NRs deposited onto ZnO base film/ Si (100) had obtained had diameter of around 64.77 nm (SD 23.71). ZnO NRs deposited onto ZnO base film/ITO had diameter size of around 78.49 nm (SD 21.40 nm) with a length of (419.5) (SD 103.5 nm) for 120 °C.....	65

- Figure 42. FE-SEM images for (a) ZnO NRs/ ZnO/Si, a reaction time of 4 hours and 0.001 M HMT and Zn^{2+} at 95 °C (b) ZnO rod/ ZnO/ITO, reaction time of 4 hours at 0.001 M HMT and Zn^{2+} at 95 °C. (c) ZnO NRs/ ZnO /Si films, at reaction time of 4 hours at 0.1 M HMT and Zn^{2+} at 95°C (diameter of 500 nm and 3 μ m lengths) (d) ZnO NRs/ ZnO /Si films, at reaction time of 1.5 hours at 0.01 M HMT (diameter of 75 nm and 500 nm lengths). The same reaction conditions were maintained for both substrates (Si and ITO) with a ratio 1:1 for Zn^{2+} and HMT, at a temperature of 95 °C. 67
- Figure 43 SEM image for ZnO rods collected from (a) a reaction time for 4 hours at 0.1 M HMT and Zn^{2+} at 95°C and (b) shows ZnO rods with a reaction time of 24 hours at 0.1 M HMT and Zn^{2+} at 95 °C..... 68
- Figure 44 FE-SEM images of ZnO NRs on ZnO base film on Si (100) arrays with a diameter of: (a) 60 nm and lengths well exceeding 3 μ m. (b) Approach Micrograph of ZnO NRs on ZnO base film/ Si(100). (c) ZnO rods/ ZnO base film/ Si (100) arrays. (d) ZnO NRs on ZnO base film on ITO film with a diameter of 75 nm and 500 nm lengths. The same reaction conditions were maintained for both substrates (Si and ITO) with a 1:1 ratio of 0.01M for Zn^{2+} and HMT, with a temperature of 95 °C and 1.5 hours of reaction time. 69
- Figure 45. ZnO NR while light micrograph of: (a) ZnO NR/ZnO base film /Si (100), (b) Au-coated on ZnONR/ZnO base film/ Si(100) at 2 hours of UV–irradiation time. (c) Au-coated ZnO NRs/ZnO base film/Si by ion beam sputtering. 75
- Figure 46. XRD a) Au-coated on ZnO NR/ZnO base film/ ITO and b) Au-coated on ZnO NR/ZnO base film/ Si(100). Au coating on ZnONR were formed by the reaction 1×10^{-3} M of $HAuCl_4$ aqueous solution kept at pH 7.2, with 2 hours of UV-irradiation reaction time at room temperature. 77
- Figure 47. EDS Spectra from (a) ZnO NRs/ZnO basefilm/Si (100). (b) Au-coated ZnO NRs/ZnO base film/Si by ion beam sputtering. 78
- Figure 48. FE-SEM images of ZnO NRs/ZnO/Si morphology a) from Au coated on ZnO NRs/ ZnO/ Si (100), at 2 hours of UV–irradiation time. b) Zoom of a). c) Au coated on ZnO NRs/ ZnO/ Si (100), at 4 hours of UV-irradiation time and (d) Approach Micrograph of c). The experimental conditions were: 1×10^{-3} M of $HAuCl_4$ solution kept at pH 7.2..... 79
- Figure 49. (a) EDS spectra for Au-coated ZnO NRs/ZnO base film/Si (100), 1×10^{-3} M $HAuCl_4$ with 4 hours of UV irradiation (b) FE-SEM images of ZnO NRs/ZnO/Si (100) morphology. 80
- Figure 50. FE-SEM image of Au-coated ZnONR/ZnO base film/ITO, 1×10^{-3} M of $HAuCl_4$ solution kept at pH 7.2 with an UV-time reaction of: (a) 0 h (b) 2 h SEM image. . 81
- Figure 51. Raman spectrum of Au-coated on ZnO rods deposited onto base film on Si (100). Acquisitions were obtained at 3 accumulations, 10 s integration time using a laser power of 785.0 nm, 140 mW measured at head. 82
- Figure 52. Comparison of 4-ABT Raman spectrum from (left) (a) 0.1 M 4-ABT on Au coating ZnO NRs/ZnO base film/Si from ion beam method. (b) 2 μ L of a solution 1×10^{-4} M 4-ABT on Au coating ZnO NRs/ZnO base film/Si. (Right) 0.1 M 4-ABT on Au coating ZnO NRs/ZnO base film/Si from UV photo-reduction method. A similar

procedure was used in both samples dissolved in ethanol prepared at an adjusted pH= 7.5 and mixed with 100 μ L of 0.1 M sodium chloride (NaCl). Acquisitions were obtained at 3 accumulation, 10 s integration time using a laser power of 785.0 nm, 98 mW measured at head. 83

Figure 53. SERS of 4-ABT on (left) Au coating ZnO NRs/ZnO base film/Si by ion beam method (32nm) ;(a) 1×10^{-4} M -4ABT, (b) 1×10^{-8} M 4-ABT. (Right) Au coating ZnO NRs/ZnO base film/Si UV light lamp (a) 1×10^{-4} M 4-ABT (b) 1×10^{-8} M 4-ABT on Au-ZnO NRs Spectra were acquired using a 785 nm laser with 98 mW (measured at head) at 3 accumulations, 10 s integration each time. 84

Figure 54. Mapping of 4- ABT on Au coating ZnO NRs/ZnO base film/si. to analyze the reproducibility in ZnO NRs coated with Au..... 85

Figure 55. SERS of 4 Nitrobenzenethiol on Au coating ZnO rods/ZnO base film/Si..... 86

Figure 56. Peak area comparison from SERS spectra of 4-NBT of (a) Au-ZnO NRs and (b) Au-ZnO rods. 87

Figure 57. SERS of analytes on Au coating ZnO NRs/ZnO base film/Si. UV light lamp method. (Left) (a) 1×10^{-4} M adenine (b) 1×10^{-8} M. Right (a) RD 1×10^{-4} M (b) RDX 1×10^{-6} M, A similar procedure was used in both samples dissolved in ethanol prepared at an adjust adjusted pH= 7.5 and mixed with 100 μ L of 0.1 M sodium chloride (NaCl). Acquisitions were obtained at 3 accumulation, 10 s integration time using a laser power of 785.0 nm, 98 mW measured at head. 89

Figure 58. SEM micrographs of gold coated on silica nanowires (A) For SiO₂ NWs deposition 80 μ L of the stock solution was added to 2 mL of acetonitrile, sonicated 1 min followed by apply a step potential of 100 V for 60 s. (B) Higher-magnification image clearly indicating the average diameter size for SiO₂ NWs is of 50 nm..... 113

Figure 59. High ResolutionTEM micrographs of gold coated on silica nanowires (A) For SiO₂ NWs deposition 80 μ L of the stock solution was added to 2 mL of acetonitrile, sonicated 1 min followed by application of a step potential of 100 V for 60 s. (B) Higher-magnification image clearly indicating the average diameter size for SiO₂ NWs is of 50 nm to 90 nm. 113

Figure 60. Gold-coated SiO₂ NWs demonstrating that the substrate is active for SERS implementation. a) antibody. b) blocked with 1% BSA. c) 1 pg/mL PSA. d) 1 ng/mL PSA. e) 50 ng/mL PSA. f) 50 ng/mL PSA. PSA spectra were acquired at 3 scans, 10 s integration time using a laser wavelength of 632 nm. 115

List of Tables

Table 1 Lattice parameters of several epitaxy substrates.....	22
Table 2 Parameters of Sputtering Deposition of Zn	31
Table 3. Average crystallite size of ZnO base film/ITO deposited at different temperatures by magnetron sputtering.	44
Table 4. Average crystallite size of ZnO base/ITO film deposited at different times by magnetron sputtering.	46
Table 5. Average crystallite size of ZnO base/ Si (100) film deposited at different temperatures by magnetron sputtering.....	49
Table 6 Average crystallite size of ZnO NRs/ ZnO base film/ITO film deposited at different temperatures by magnetron sputtering.....	51
Table 7. Average crystallite size of ZnO NRs/ ZnO base/ Si (100) film deposited at different temperatures by magnetron sputtering.....	54
Table 8 Average crystallite size of ZnO thin films deposited on different substrates.....	57
Table 9 Band assignments for SER spectra for the epitope in the PSA molecule. Three residues of amino acids on Au-coated ZnO NRs are most important.....	114

CHAPTER 1: INTRODUCTION

1.1 Justification

The quests for fundamental knowledge, as well as technological interest, have led to intensive research in many fields for production of nanomaterials [1-7]. Studies on zinc oxide (ZnO) conducted for several decades have shown the dependence of the physical properties of the materials obtained on the wet chemistry method for its preparation¹. Chemical-surface requirements of controlled size and shape and chemical roughening as a route to improving optical properties of the semiconductor nanostructures are also of high priority.

Recent developments in nanotechnology, along with the demonstration of various quantum size effects in nanoscale particles have been reported for zinc oxide (ZnO) [1] with a special concern for nanowires or nanorods (NRs) structures. These are of interest due to their potential application in chemical sensors, micro-lasers, cantilevers, optoelectronics, and surface enhanced Raman spectroscopy (SERS)-based biosensors among other device applications [9-10]. Studies on ZnO have shown superior optical material properties. These depend on their NRs morphology and crystalline structure [3], confirming the feasibility for the design of multifunctional ZnO structures. This could be achieved by careful manipulation on the synthetic method employed for its preparation [4]. The properties previously mentioned can be modified with the goal of improving size control, shape and roughening surface of the nanostructures. For ZnO nanostructure growth, various methods such as vapor phase synthesis, low-temperature thermal deposition and high-temperature vapor phase transport (VPT) have been employed [11-13]. For ZnO NRs growth, various methods including hydrothermal growth and template-assisted growth have been reported [14]. Chemical bath deposition (CBD) and electrophoresis [15] have been also utilized. However, (CBD) is a relatively time-consuming technique, with a deposition time reported up to 50 h [15]. During such long deposition times, to avoid the NRs agglomeration into a thin film, it is necessary to use surfactants to cap the lateral facets of the ZnO crystals [16, 17]. In contrast, VPT techniques such as the carbothermal reduction one are relatively fast and clean,

depositing higher optical quality NRs, with reasonable lengths (1-3 μm) in growth times of approximately 1 h [18]. The results of this process were similar to the hydrothermal/wet chemistry technique used to prepare ZnO rod/NRs, but the difference consisted in a reduction of the proportions in ZnO NRs between 100-200 nm diameter sizes [19]. The hydrothermal growth process is commonly used and involves an epitaxial anisotropic crystal growth in a solution at lower temperature [16, 18]. Further use of ZnO base films layer has clearly showed the scalability of this technique [14, 15].

Vayssieres has reported a method for the fabrication of ZnO rods and nanowires in aqueous phase [16]. This route allows the formation of well-crystallized rod-shaped structures of better uniformity with respect to the samples produced via sol-gel methods [20-21]. Vayssieres' original route was based on the thermal decomposition of zinc nitrate hexahidrate and methenamine solutions. This approach allowed the formation of well-aligned hexagonal ZnO rods, 100-200 nm wide and up to 10 μm long [16, 21]. Recently, a modification of Vayssieres' method has been successfully applied by the authors for the preparation of a biosensor for urea [22]. However, the study was limited to ZnO rods deposited onto a base film of ITO, without providing further details about the synthesis and characterization of the produced materials. Accordingly, the present work is focused on the systematic study of the growth of ZnO-NRs and its dependence on the type of substrate and the sputtering conditions to deposit the ZnO base layer. The proposed approach is relatively simple and easy-to-scale up and considers the use of a reflux system at 95°C. Two types of substrate were evaluated: Si (100) and indium tin oxide (ITO), to determine whether their structural features affect the morphology of the rods obtained.

However, due to the lattice mismatches between the ZnO thin film deposited and the substrate which is larger for the case of ZnO/Si (40%) than for ZnO/ITO (3%), both material systems between wurtzite ZnO and cubic Si (100) a difference of 40% is estimated [23]. Wurtzite ZnO is expected that and ZnO on ITO substrate could exhibit a better crystal quality [23].

In addition, our work was also focused on the evaluation of alternatives conducive to a more precise control of the rod thickness by proper selection of the deposition conditions for base ZnO films. It was expected that the finer the grain size in the base ZnO films, the thinner the ZnO NRs that can be formed [16, 17, 20].

Research in this field has gained considerable attention in different areas such as chemistry, biology, materials sciences and in building blocks for miniaturization of electronics photonics devices and sensor for Surface Enhanced Raman Spectroscopy (SERS) [24, 25, 26]. Recent observations of SERS signals from thiol molecules suggest the formation of a strong and stable adsorption on ZnO semiconductor nanoparticles and detection of SERS enhanced signals for Rhodamine G on gold (Au) coated nanorod arrays [24].

The innovation in the nanocoatings on ZnO NRs substrates with metals helps to improve the sensitivity of the technique to achieve low-level detection for analytes on this surface, making possible accurate detection of nitroexplosives, biological molecules and chemical compounds by Enhanced Raman Scattering (ERS). However, novel nanocoatings of appropriate substrates improve the efficiency in the technique to low-level detection of analyte on the substrate. The Department of Homeland Security incorporated intelligent sensors technology to develop, manufacture and market products for national security, industry, and medicine. A portable trace explosives detection device for chemical agents detector was developed following these considerations [25]. Finally, the third reason is to respond to the challenges of new discoveries. The social and economic contributions of nanoscience have prompted U.S. Federal agencies participating in the Nanoscale Improvement, Engineering, and Technology Subcommittee and U.S. chemical-physics companies of all sizes to commit significant resources to nanotechnology research and development. The race to search for, improve, and commercialize nanomaterials is global. The U.S has accomplished nanotechnology development in important areas such as sensors, catalysts, separations, high-performance materials, coatings, energy conversion and storage, electronics and pharmaceuticals, just to name a few.

The ability to synthesize Au nanocoating on ZnO nanorods (ZnO NRs), is important for exploring their physical properties of not only individual single components but also their combinations in SERS applications. ZnO NRs composites, made by uv lamp deposition and ion beam sputter, have attracted wide interest because the structure, growth morphologies and electrical properties of ZnO NRs that distinguishes them from their monometallic counterparts.

The focus of this work will center on the optimization of conditions to control size of rods or nanorods both in the seed as well as during growth and orientation of the rods by thermal variations of the wet chemistry. The second goal is to coat the resulting nanorods with SERS-active gold layers. This metal is known to be such an excellent substrate for SERS studies while the effect is less pronounced on ZnO. Combining Au with ZnO semiconductor may result in new stable substrates for SERS studies in the detection of could successfully detect analytes such as: adenine, 4-nitrobenzenethiol and 2, 4-aminobenznethiol (ABT) and 1, 3, 5-trinitroperhydro-1, 3, 5-triazine (RDX) at low detection levels.

1.2 Objectives

1.2.1 Main Objective

- The aim of this study is to optimize the size of ZnO rods to obtain ZnO nanorods taking into account the dependence of coating of metal such as the gold on ZnO arrays; with the purpose of conducting studies in surface enhanced Raman scattering (SERS) for the detection of analytes such as: 4-aminobenznethiol (4-ABT), 4-nitrobenzenethiol, adenine, and 1, 3, 5-trinitroperhydro-1, 3, 5-triazine (RDX) at low levels.

1.2.2 Specific Objectives

1. To determine the influence of the type of substrates (p-type Si (100), and ITO) on the quality of the ZnO films deposited by RF magnetron sputtering.
2. To determine optimum conditions to control the growth and orientation of ZnO rods onto previously synthesized ZnO films.
3. To determine the optimum Au-coating on ZnO rods by Ion beam and Uv lamp methods.
4. To evaluate the detection capability by SERS of produced Au-coated ZnO rods for 4-aminobenznethiol, 4-nitrobenzenethiol, adenine and 1, 3, 5-trinitroperhydro-1, 3, 5-triazine.

1.3 Dissertation Contents

This dissertation is structured in the following way:

Chapter 1 Introduction includes the justification of the research work as well as the objectives. The theoretical background, including the relationship between ZnO properties and crystal size, in addition to fundamental concepts on SERS and experimental design, are discussed in Chapter 2. The literature review about ZnO and Au coated ZnO and their applications are summarized in Chapter 3. Chapter 4 describes the deposition protocols of ZnO base film on Si (100) and ITO films. That chapter also deals with the optimization of the synthesis parameters for shape and diameter reduction of ZnO rods by wet chemistry methods and the corresponding characterization of ZnO NRs. The results obtained from the optimization of Au-coated on ZnO NRS/ ZnO base film/ Si (100) and ZnO NRs/ ZnO base film/ ITO are discussed in Chapter 5. Chapter 6 presents the future works related to this project.

CHAPTER 2: BACKGROUND

2.1 Physical Properties of Zinc Oxide

Zinc oxide is an important electronic and photonic material because of its wide direct band gap (3.37 eV) and a relatively large exciton binding energy of 60 meV [27-30]. It exhibits many interesting properties including near-UV emission, [29-30] transparent conductivity, [31] and piezo- electricity.

Zinc oxide is a unique material that exhibits semiconducting and piezoelectric dual properties. Using a solid–vapour phase thermal sublimation technique, nanocombs, nanorings, nanohelices/nanosprings, nanobelts, nanowires, nanocages and oriented helical ZnO nanorod arrays of ZnO have been synthesized under specific growth conditions [31-38]. However, despite great progress in this field, the shape-controlled synthesis of ZnO nanocrystals, especially regarding control over the complex structure, still remains a remarkable challenge. A summarized review on the structural and functional features of this material is presented in the next section.

2.1.1 Crystal Structure of Zinc Oxide

Zinc oxide, a II-VI compound semiconductor crystallizes in either cubic zinc blende or hexagonal wurtzite structure; where each anion is surrounded by four cations at the corners of a tetrahedron, and vice versa, as shown in Figure 1. These materials exhibit a substantial ionic character, despite a tetrahedral coordination that is typical of sp^3 covalent bonding. Typical structures in ZnO are wurtzite, zinc-blende, and rocksalt as schematically shown in Figure 1. At ambient conditions, the thermodynamically stable phase is wurtzite, while the zinc blende ZnO structure can be stabilized only by growth on cubic substrates. The rocksalt structure may be obtained at relatively high pressures [39, 40].

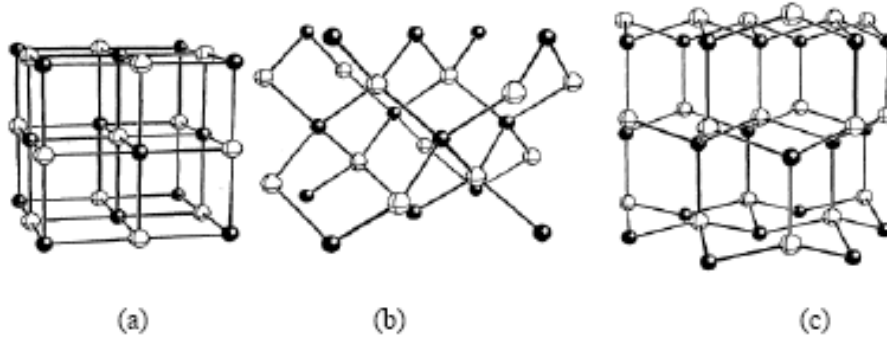


Figure 1. ZnO crystal structures: (a) rocksalt , (b) zinc blende and (c) wurtzite [41].

Wurtzite zinc oxide has a hexagonal structure (space group $C6mc$) with lattice parameters $a = 0.3296$ and $c = 0.52065$ nm [38]. The structure of ZnO can be described as a number of alternating planes composed of tetrahedrally coordinated O^{2-} and Zn^{2+} ions, stacked alternately along the c -axis as shown in Figure 2.

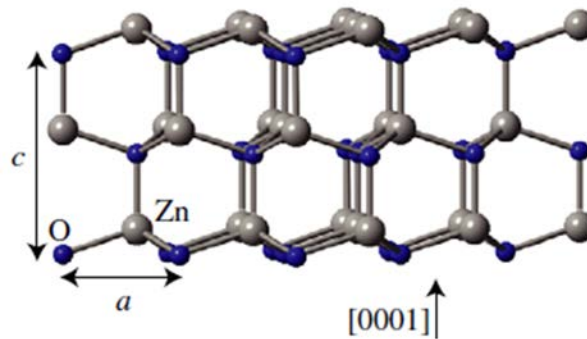


Figure 2. The wurtzite crystal structure of ZnO with the lattice parameters a and c

Furthermore an important characteristic of ZnO is its polar surfaces. The most common polar surface is the basal plane. The oppositely charged ions produce positively charged Zn-(0001) and negatively charged O-(000 $\bar{1}$) surfaces, resulting in a normal dipole moment and spontaneous polarization along the c -axis as well as a divergence in surface energy [39]. To maintain a stable structure, the polar surfaces generally have facets or exhibit massive surface reconstructions, but ZnO- $\pm(0001)$ are exceptions: they are atomically flat, stable and without reconstruction [40-41]. Efforts to understand the superior

stability of the ZnO $\pm(0001)$ polar surfaces are at the forefront of research in today's surface physics [42–44]. The other two most commonly observed facets for ZnO are $(2\bar{1}\bar{1}0)$ and $(01\bar{1}0)$, which are non-polar surfaces and have lower energy than the (0001) facets.

2.1.2 Typical growth structures of ZnO

Structurally, ZnO has three types of fast-growth directions: $(2\bar{1}\bar{1}0)$, $\pm(2\bar{1}\bar{1}0)$, $(\bar{1}2\bar{1}0)$, $\pm[(1\bar{1}20)$; $(01\bar{1}0)$, $\pm(01\bar{1}0)$, $\pm(10\bar{1}0)$, $\pm(1\bar{1}00)$, $\pm(0001)$ [45]. Together with the polar surfaces due to atomic terminations, ZnO exhibits a wide range of novel structures that can be grown by tuning the growth rates along these directions. One of the most profound factors determining morphology involves the relative surface activities of various growth facets under given conditions. Macroscopically, a crystal has different kinetic parameters for different crystal planes, which are emphasized under controlled growth conditions. Thus, after an initial period of nucleation and incubation, a crystallite will commonly develop into a three-dimensional object with well-defined, low-index crystallographic faces. Figures 3(a–c) show a few typical growth morphologies of 1D nanostructures for ZnO. These structures tend to maximize the areas of the $(2\bar{1}\bar{1}0)$, $(01\bar{1}0)$, facets because of their lower energy. The morphology shown in Fig. 3d is dominated by the polar surfaces, which can be grown by introducing planar defects parallel to the polar surfaces [45]. Planar defects and twins are observed occasionally parallel to the (0001) plane, but dislocations are rarely seen.

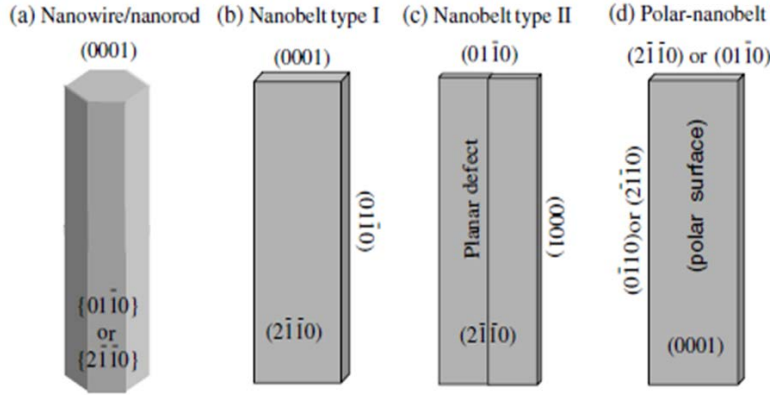


Figure 3. Typical growth morphologies of one-dimensional ZnO nanostructures and the corresponding facets.

2.1.3 Electronic band structure of ZnO

The energy of single free carrier is described by the band structure $E(\mathbf{k})$. This is a function of the quasi-momentum \mathbf{k} determined by the periodic boundary conditions. The properties of the band structure are determined by the symmetric properties of the semiconductor crystal and the chemical binding of the constituting elements. The crystal and electronic band structure of ZnO have been studied by various total-energy methods: Local Density Approximation (linear muffin-tin orbital), Linear Combination of Atomic Orbitals (LCAO), Hartree-Fock, pseudopotential and full-potential linearized augmented-plane-wave, self-interaction corrected pseudopotentials, and the GW approximation [46].

Figure 4a shows the band structure of bulk ZnO near the Γ line of the Brillouin zone. The most important thing to notice is that between the occupied bands and the empty bands (specified between Γ_1 and $\Gamma_{1.5}$) there is an optical band gap, E_g , of approximately 3.3 eV. This is the energy difference between the full and empty electron states. These filled states are called the valence band, and the energy at the top of the valence band is conventionally the zero of energy and is called the valence band edge. The empty states above the gap are called the conduction band. The lowest point in the conduction band is called the conduction band edge. For ZnO, the conduction band edge is at $\mathbf{k} = 0$, the Γ point, which is also the \mathbf{k} -value of the valence band edge. Since for ZnO the valence band and the conduction band edges occur at the same \mathbf{k} -values, the material is called a direct band gap semiconductor [47].

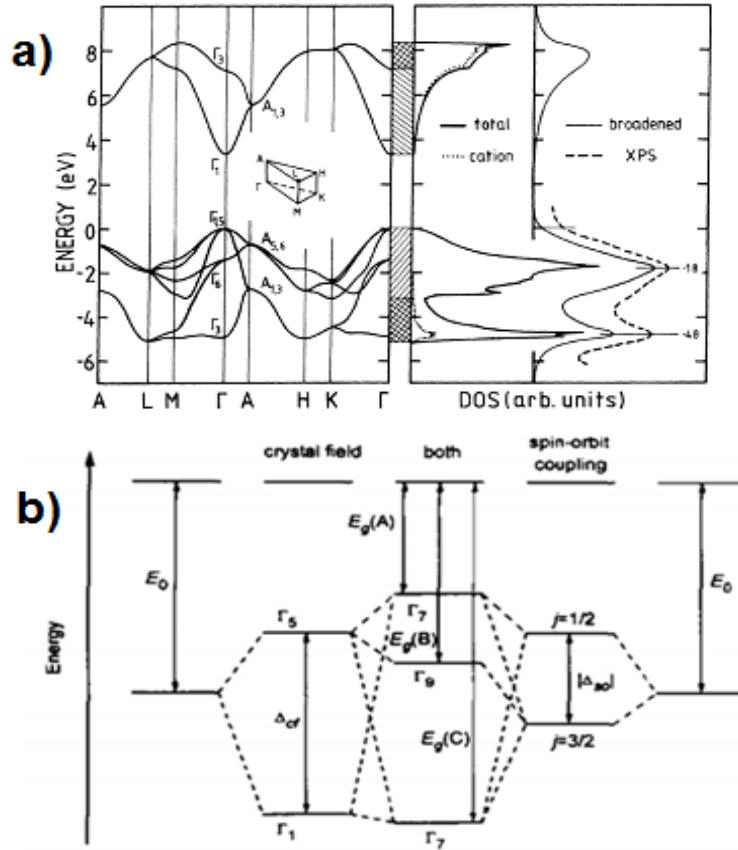


Figure 4. (a) Bulk band structure of ZnO for various high-symmetry lines in the irreducible part of the bulk Brillouin zone and density of states. The full line shows the total density of states and the dotted line gives the cation contribution to the DOS. [48]; (b) Splitting of the VB in hexagonal ZnO under the influence of crystal field and spin-orbit coupling. (The figure is not drawn to scale) [42]

ZnO has rather ionic binding. Consequently, the conduction band (CB) arises essentially from Zn^{2+} 4s orbitals, whereas the upper valence bands (VB) arise from the O^{2-} 2p states with an admixture of Zn^{2+} 3d levels. The valence band is p like, splitting into three doubly degenerate bands due to hexagonal crystal field (Δ_{cf}) and spin orbit (Δ_{so}) interactions labeled as A, B and C from higher to lower energies. Their ordering has been found to be $\Gamma_7(5)$, $\Gamma_9(5)$ and $\Gamma_7(1)$ respectively, in which the number in parentheses indicates the parent state without spin-orbit coupling as shown in Figure 4b. This particular ordering results from the negative spin-orbit splitting, which in turn is due to the participation of the Zn^{2+} 3d levels [48]. The possibility of a negative spin-orbit splitting was first suggested by Cardona [49]. However, the ordering of the valence bands, has been subject to extensive discussions [50].

2.1.4 Photoluminescence (PL)

The origin of the luminescence center and the luminescence mechanism are not really understood, being frequently attributed to oxygen vacancies or zinc interstitials [51]. The mechanism of the defect-related electron-hole recombination process in ZnO has been intensively investigated. The luminescence of ZnO exhibits a band edge ultraviolet UV emission peak and a broad visible emission band related to deep level defects. Among the different mechanisms proposed to explain the visible luminescence, oxygen vacancies V_O have been widely considered as the most probable candidate, although no consensus could be reached regarding the charge state of the oxygen vacancy, i.e., singly ionized [52] or doubly ionized oxygen vacancy [53] exploited as an oxygen source.

Several works report results about ZnO nanobelts produced by the catalyst are rather narrow, thin and uniform as shown in Figure 5a. TEM images show ZnO nanobelts in the range of 4-7 nm, indicating very good size uniformity. Photoluminescence measurements were performed at room temperature using a Xe lamp with an excitation wavelength of 330 nm to examine the size induced quantum effect in the ultra thin ZnO nanobelts. In addition, as one of the characteristics of nanoscale systems, quantum confinement was observed to cause a blue shift in the near UV emission peak in ZnO nanobelts [54], illustrated in Figure 5b. Quantum size confinement can significantly enhance the exciton binding energy [55]. PL spectra show that ZnO nanowire is a promising material for UV emission, while its UV lasing property is of more significance and interest. ZnO nanowire/nanorod is a natural candidate for optical waveguide.

Intrinsic optical properties of ZnO nanostructures are being intensively studied for implementing photonic devices. Photoluminescence (PL) spectra of ZnO nanostructures have been extensively reported [56-60]. Excitonic emissions have been observed from the photoluminescence spectra of ZnO nanorods [61]. Recently, a red luminescence band was reported which was attributed to doubly-ionized oxygen vacancies [62]. The strong emission peak at 380 nm was assigned to a band-to-band transition and the green-yellow emission band was related to oxygen vacancy as shown in the blue loop of Figure 5b. These results

are consistent with those of bulk ZnO. Furthermore, the green emission intensity increases with decreasing nanowire diameter. This observation is attributed to the larger surface-to-volume ratio of thinner nanowires favoring a higher level of defects and surface recombination [62].

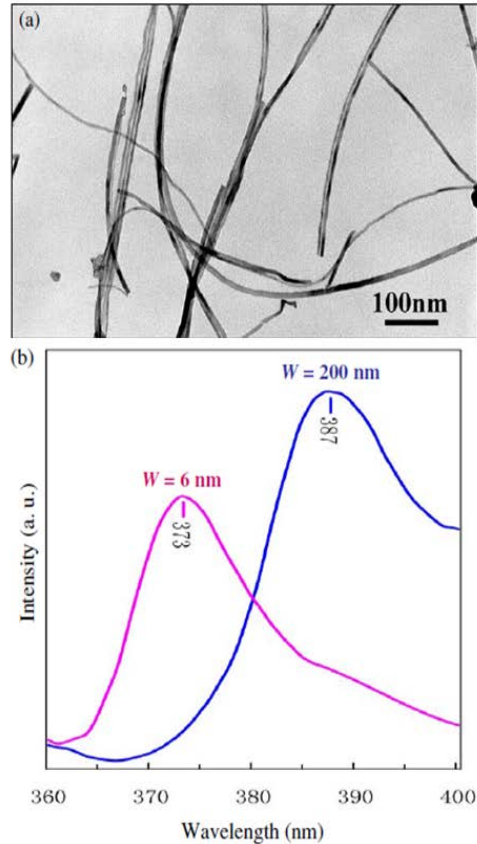


Figure 5. (a) Controlled synthesis of 6 nm wide ZnO nanobelts. (b) Photoluminescence spectra recorded from ZnO nanobelts with widths of 200 and 6 nm, respectively, showing a blue-shift with a reduction in nanobelt size [54].

ZnO nanowire lasers offer additional advantages: the excitonic recombination lowers the threshold of lasing, and quantum confinement yields a substantial density of states at the band edges and enhances radiative efficiency. Optical wave guiding using dielectric nanowire also achieved considerable progress. Recently, ZnO nanowires were reported as sub-wavelength optical waveguides [63]. Optically pumped light emission was guided by ZnO nanowire and coupled into a SnO₂ nanoribbon. These findings show that ZnO nanostructures can be potential building blocks for integrated optoelectronic circuits. Kind *et al* [64] reported that besides UV emitting and lasing, ZnO nanowires have been used for UV

photodetection and optical switching. Detection of defect state-related wavelengths in the visible region and polarized photodetection of ZnO nanowires have been achieved.

When the electric field component of the incident light is polarized parallel to the nanowire long axis, the photocurrent is maximized. The photoconductivity measurements of ZnO nanowires showed that the presence of O₂ has an important effect on the photoresponse, [65, 66]. It was found that the desorption-adsorption process of O₂ affects the photoresponse of ZnO nanowire. Upon illumination, photogenerated holes discharge surface-chemisorbed O₂ through surface electron-hole recombination, while the photogenerated electrons significantly increase the conductivity. When illumination is switched off, O₂ molecules re-adsorb onto the nanowire surface and reduce the conductivity.

2.2 Techniques of deposition of ZnO

ZnO-based films are prepared using a variety of deposition techniques such as metal Plasma-Enhanced Metal–Organic Chemical Vapor Deposition (PEMOCVD) and Pulsed Laser Deposition (PLD) among others. One of the deposition techniques mostly used due to its versatility is Magnetron Sputtering (MS). The fundamental difference between magnetron sputtering as a plasma process and thermally excited thin-film preparation methods (evaporation, chemical deposition methods) is the much higher energy input into the growing film provided by high deposition rates.

2.2.1 Magnetron Sputtering (MS)

Magnetron sputtering is now one of the most versatile techniques used for the deposition of transparent conductive oxides such as zinc oxide and indium tin oxide. It is a promising technique, which allows the deposition of films at optimized temperatures with good optical and electronic properties [67].

The fundamental difference between magnetron sputtering as a plasma process and thermally excited thin-film preparation methods (evaporation, chemical deposition methods) is the much higher energy input into the growing film that can be achieved by magnetron

sputtering. This technique is characterized by the following advantages [68]:

- good adhesion of films on substrates
- high deposition rates (up to $12 \mu\text{m min}^{-1}$)
- low substrate temperature
- good controllability and long-term stability of the process
- very good thickness uniformity and high density of the films
- by reactive sputtering in rare/reactive gas mixtures many compounds can be deposited from elemental (metallic) targets.
- relatively cheap deposition method.

The basic feature of a magnetron discharge is the confinement of the plasma in front of the target (cathode). This is achieved by the combination of electric and magnetic fields [69]. The magnetic field strength is adjusted in such a way (about 50 to 200 mT) that the electrons are significantly influenced by the magnetic field while the ions are not. The vacuum of sputtered atoms can be sustained at much lower pressures (10^{-4} torr) and/or higher current densities than the glow discharges without magnetic assistance. Tunable parameters for magnetron sputtering are: pressure, discharge power, design of the magnetic field (i.e. balanced or unbalanced magnetrons) and the excitation mode (dc or rf). Standard sputtering processes usually involve two modes of powering the magnetron sputtering system. The first method employs direct current. The second method involves the use of a radio frequency source with a typical frequency of 13.56 MHz. This method is preferred for both conductive as well as non-conductive targets (ceramic targets) [70]. This mode was mainly employed in the present study.

The ATC Orion 8-Linear E-Beam Magnetron Sputtering instrument was used for deposited ZnO base film on Si(100) and ITO substrates. The magnetron sputtering is a system with an on-axis configuration with two-magnetron sputter guns for two modes sputtering process: radio frequency (RF) and direct current (DC) magnetron. The process chamber is made of 304-grade stainless steel with cylindrical design 16” diameter x 16” high with full opening top plate for easy access to all internal parts – the guns for changing targets, substrate stage for loading and unloading samples. The two-magnetron guns of 2” diameter

with shutters are mounted on the plate at 65-degree angle [71]. The guns can be adjusted linearly to vary the distance between the substrate and the guns Figure 6a. For rf excitation the potential distributions using a ceramic target of ZnO is shown schematically in figure 6b. The rf plasma is mainly driven by ionization due to electrons which perform an oscillating motion in the plasma body. The electrons are able to follow the rf frequency (atypical) of 13.56 MHz, while the ions (Ar^+ , O^+ , Zn^+) are not, due to their inertia. These positives ions are accelerated in the cathode fall $V_p - V_{dc}$ towards the cathode, leading to the sputtering of the target. On the other hand, electrons and negative ions (O^-) move from the target to the substrate [72].

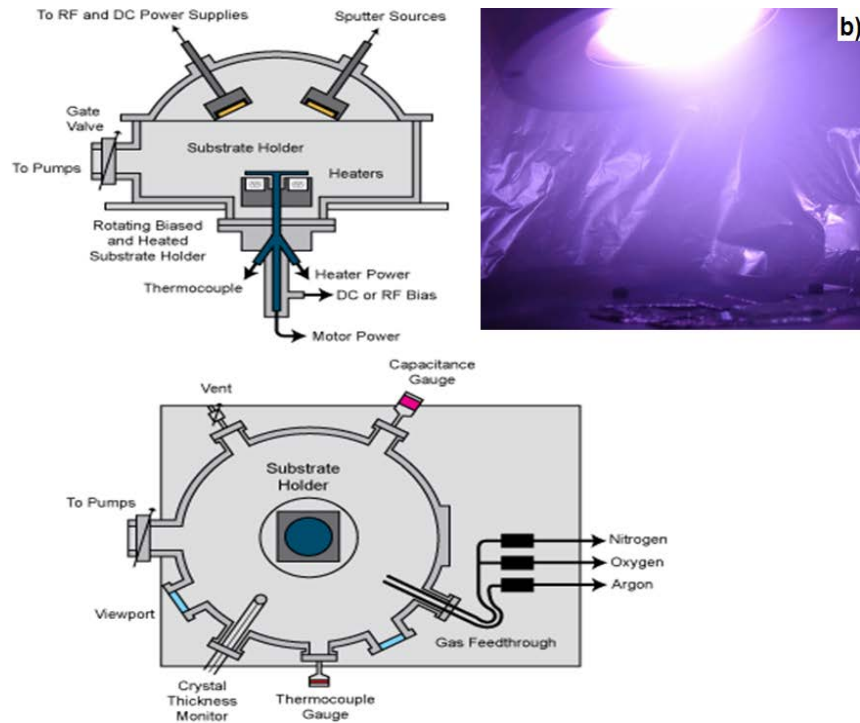


Figure 6. (a) Schematic diagram of a magnetron-sputtering configuration for simultaneous rf and dc excitation [72] (b) Plasma as is used in magnetron sputtering.

2.2.2. Plasma-enhanced Metal -Organic chemical vapor deposition (PEMOCVD)

This is one of the most attractive methods for synthesis of high perfection ZnO films at low temperatures. It consisted of two perforated aluminum electrodes, 33mm in diameter, separated by a gap 1.6mm wide (Atomflot- 250D from Surfex Technologies) connected to an

RF power supply at 13.56MHz, while the lower electrode could be grounded. A third aluminum plate can be installed beneath the lower electrode. It contained a network of channels and holes that mixed the metalorganic precursors with the plasma afterglow. Located 4 mm further downstream are usually rotating sample stage with integrated heating system. Figure 7 shows a schematic of the plasma reactor for this technique

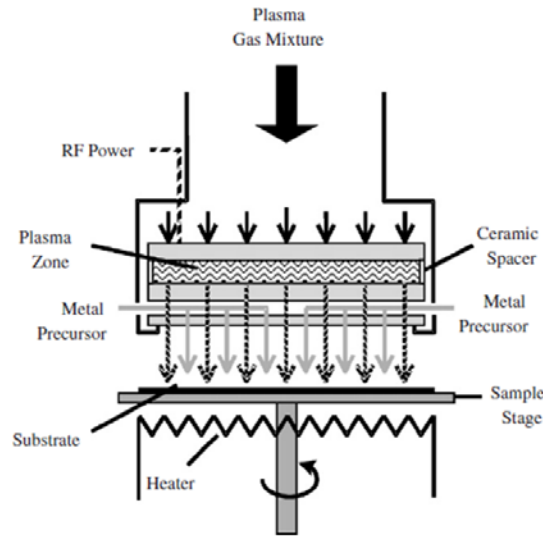


Figure 7. Schematic of the atmospheric plasma source and substrate holder

In the last 20 years since the chemical vapor deposition (CVD) of diamond was developed, it was followed by that of fullerenes and carbon nanotubes [73, 74]. Nanocrystalline diamond films have also attracted interest [75], because they have a low electron emission threshold voltage and a low coefficient of friction. The small grain size (approximately 5–100 nm) gives films valuable tribological and field-emission properties comparable to those of conventional polycrystalline diamond films. Amorphous and nanostructured carbon films have been studied for use as cold-cathode sources, electron emitters and hard low-friction coatings. From the fundamental perspective, on the other hand, the structure of these materials contains both threefold-coordinated (sp^2 -bonded) and fourfold-coordinated (sp^3 -bonded) carbon atoms. Furthermore, applications for micro-electro-mechanical systems (MEMS) devices, metal-semiconductor field effect transistors

(MESFETs), biochemical devices and electrochemical electrodes that take advantage of these excellent properties have been proposed [76, 77].

2.3 Synthesis of ZnO Nanostructures

The different surface structures of ZnO could induce anisotropic growth. Under thermodynamic equilibrium conditions, the facet with higher surface energy is usually small in area, while the lower energy facets are larger. Specifically, in the ZnO growth, the highest growth rate is along the *c*-axis and the large facets are usually (01 $\bar{1}0$) and (2 $\bar{1}$ $\bar{1}0$). Growth kinetics could be controlled by means of the controllable synthesis parameters, such as deposition temperatures and pressures as well as carrier gas flux.

2.3.1 Vapor Transport Synthesis

This method utilizes a vapor transport process. In such a process, zinc and oxygen or oxygen mixture vapor are transported and react with each other, forming ZnO nanostructures. This technique possesses several ways to generate zinc and oxygen vapor. In the direct method, Zn powder is heated under oxygen flow [78, 80]. This method facilitates relative low growth temperatures (500~700°C), but the ratio between the Zn vapor pressure and oxygen pressure needs to be carefully controlled in order to obtain the ZnO nanostructures. Another technique is the decomposition of ZnO but is limited due to the very high temperatures (~1400 °C) required [81]. Another widely used is the carbothermal method [81, 82-88] where ZnO powder is mixed with graphite powder as source material. At about 800-1100 °C, graphite reduces ZnO to form Zn and CO/CO₂ vapors. Zn and CO/CO₂ later react and result in ZnO nanocrystals. The advantages of this method lie in that the existence of graphite significantly lowers the decomposition temperature of ZnO.

The indirect methods to provide Zn vapor include metal-organic vapor phase epitaxy, in which an organometallic Zn compound, diethyl-zinc for example, is used under appropriate oxygen or N₂O flow [89, 90]. According to the difference on nanostructure formation mechanisms, the extensively used vapor transport process can be categorized into the catalyst free vapor-solid (VS) process and catalyst assisted vapor-liquid-solid (VLS)

process depicted in Figure 8. Synthesis utilizing VS process is usually capable of producing a rich variety of nanostructures, including nanowires, nanorods, nanobelts and other complex structures [91-94]

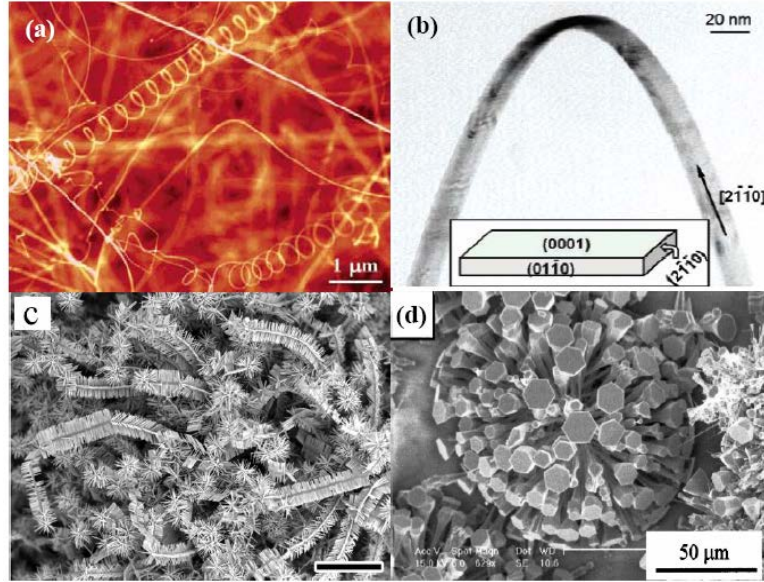


Figure 8. (a) A SEM micrograph of ZnO nanohelix structures grown via VS process. (b) A TEM image of ZnO nanobelt grown via VLS process. Inset: structure model of the nanobelt [81]. (c) Hierarchical ZnO nanostructures synthesized by vapor transport and condensation technique [89]. Scale bar: 10 μm . (d) Needle-like ZnO rods [95].

2.3.2 Metal catalyst

A focused metal catalyst is the liquid droplet which serves as a preferential site for absorption of gas phase reactant and, when supersaturated, it becomes the nucleation site for crystallization. Nanowire growth begins after the liquid becomes supersaturated in reactant materials and continues as long as the catalyst alloy remains in a liquid state and the reactant is available. During growth, the catalyst droplet directs the nanowire's growth direction and defines the diameter of the nanowires. Ultimately, the growth terminates when the temperature is below the eutectic temperature of the catalyst alloy or the reactant is no longer available. Growth of 1D nanostructure usually follows the vapour-liquid-solid (VLS) approach, in which a liquid alloy droplet composed of a metal catalyst component (such as Au, Fe) and a nanowire component (such as Si, III-V compound, II-V compound, oxide) is first formed under the reaction conditions. The VLS crystal growth mechanism was first

proposed by Wagner and Ellis [96] in 1964 for Si whisker growth, in which Si whiskers with diameters of up to the micrometre scale were grown by hydrogen reduction of SiCl_4 with the presence of Au, Pt, Ag, Pd, Cu and Ni as the catalysts. Westwater *et al* [97] and Lieber *et al* [98] then developed this mechanism and successfully prepared nanometre scale Si wires by pyrolysis of SiH_4 with Au as the catalyst and laser ablation of $\text{Si}_{0.95}\text{Fe}_{0.05}$ targets, respectively.

Figure 9 shows a SEM image of uniform ZnO nanorods/nanowires grown using Au catalyst on a polycrystalline alumina substrate. The nanorods show no alignment and are dispersively distributed, but their diameters and lengths are rather uniform, as defined by the size of the Au catalyst. ZnO nanorods were obtained by means of the controllable synthesis parameters. For the 1D ZnO nanowires grown via a VLS process, the commonly used catalyst for ZnO employed Au as a catalyst [84].

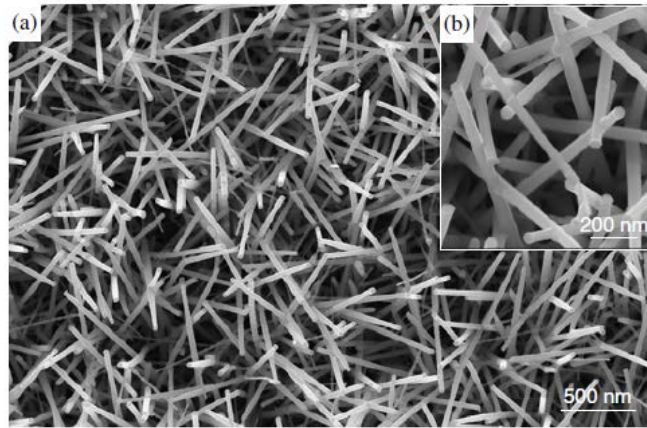


Figure 9. (a) ZnO nanorods grown using gold as a catalyst. (b) An enlarged image of the nanorods, showing gold particles at the tips [99].

The sample was deposited on a silicon substrate, as shown by an optical image displayed in Figure 10a. The most interesting phenomenon is that the as-grown products are distributed in two distinct temperature regions, with the metallic lustre in black indicating the Zn nanobelts and the white the ZnO nanobelts. Scanning electron microscopy (SEM) images show curly Zn nanobelts (Figure 10b) and straight ZnO nanobelts (Figure 10c). The Zn nanobelts were formed in a temperature range of 200–300 °C and they are distributed across

a region of >4 cm in length. The ZnO nanobelts were formed in a temperature range of 300–400 °C.

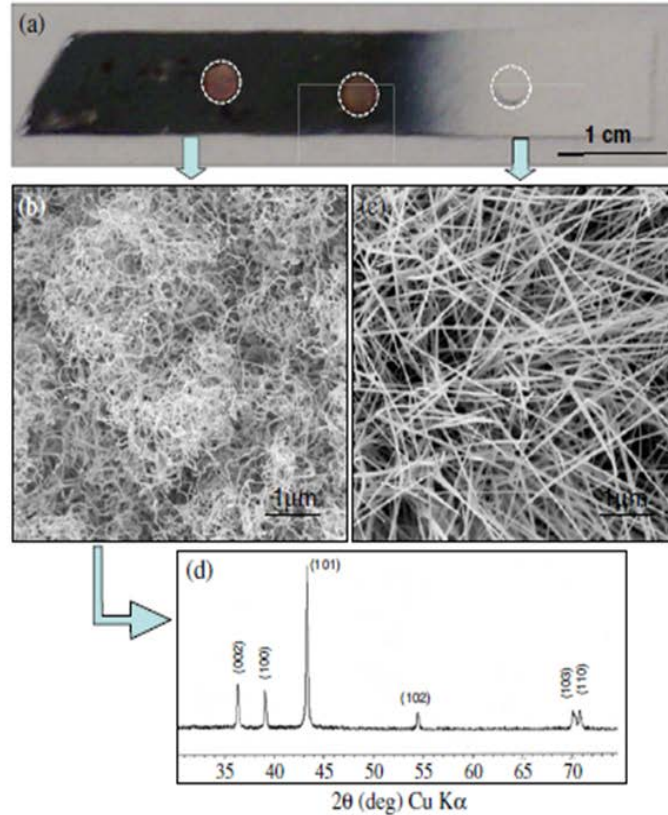


Figure 10. (a) An optical micrograph of the as-synthesized sample on a silicon substrate, showing two distinct products on the surface. The three circles indicate three TEM copper grids placed on the substrate for collecting samples (b), (c) SEM images recorded from the metallic lustre and white colour regions, presenting the formation of pure Zn nanobelts and ZnO nanobelts, respectively (d) XRD recorded from the metallic region, showing the formation of Zn nanobelts [100].

The transition distance between the two different products is <0.5 cm. This apparently shows the structural control by growth temperature and kinetics. The structure of the ZnO nanobelts has been investigated previously [100]. The X-ray diffraction spectrum recorded from the metallic region indicates that the as-received product is dominated by zinc (Figure 10d).

2.3.2 Electron-beam lithography

Electron beam of a scanning electron microscope (SEM) is used to expose small areas in a positive resist on top of the sample these exposed areas are subsequently removed in a chemical development process. If metal is evaporated onto such substrates, the metal is deposited on the substrates in the exposed areas and on the remaining resist on all other parts. By ‘lifting off’ the remaining resist one ends up with flat metal films at the exposed areas [101]. To control the locations of ZnO nanowires, both lithographic and non-lithographic patterning techniques have been utilized. With photolithography technique [102] square and hexagonal catalytic gold dot array was generated on sapphire substrate, then small diameter ZnO nanowires were grown from the patterned catalysts via a typical VLS process, as shown in Figure 11a. A simple way to create patterned catalysts array is to use shadow masks for catalyst deposition. For example, TEM grids were used to pattern square Au matrix [103]. Figure 11b shows the resulting ZnO nanowire arrays. Well-ordered and high density ZnO nanowires arrays can be obtained using advanced lithographic techniques such as electron beam lithography. In fact, this objective can be also realized by simply using non-lithographic shadow mask. Chik *et al.* have successfully fabricated hexagonal ZnO nanorod arrays by using anodic aluminum oxide membranes (AAM) as a mask to pattern Au catalyst on GaN substrate [104] In this work, a 500 nm thick AAM was carefully attached to a GaN substrate. After evaporation of Au, hexagonal catalyst dot array functioned as nanowire growth sites and resulted in the highly ordered ZnO nanowires array shown in Fig. 11c. Figure 11d shows an enlarged hexagonal ZnO nanorod array.

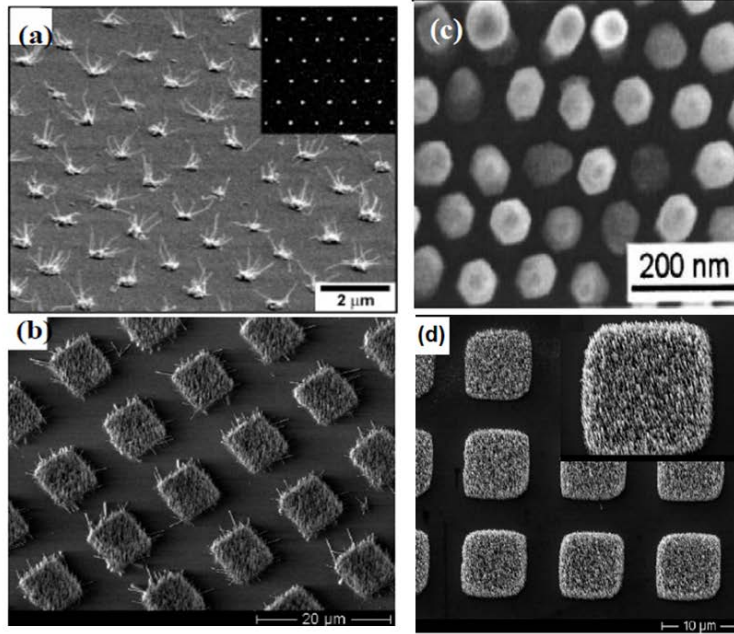


Figure 11. (a) Hexagonal ZnO nanowire array generated by lithographically patterned Au catalysts [102]. (b) Square ZnO nanowires array created using TEM grids [103]. (c) Hexagonal ZnO nanorod array with diameter ~ 60 nm and spacing ~ 110 nm (d) An enlarged hexagonal ZnO nanorod array [104].

Table 1 gives the crystal structures, lattice parameters and mismatch between ZnO (0001) plane and several epitaxy substrates. Though sapphire has been widely used as the epitaxy substrate for vertical growth of ZnO nanowires, it can be seen that GaN could be an even better candidate since it has the same crystal structure and similar lattice constants than ZnO. This has been confirmed by the work of Fan *et al.* [103] in which both the sapphire a -plane and GaN (0001) plane were used as epitaxy layer for ZnO nanowire growth. Electric field emission from vertically-aligned ZnO nanowire/nanorods also have been extensively investigated. Quasi-one-dimensional (Q1D) nanomaterial with sharp tip is a natural candidate for electron field emission [105,106-112].

Table 1 Lattice parameters of several epitaxy substrates.

Material	ZnO	GaN	Sapphire	SiC	Si
Crystal Structure	Wurzite	Wurzite	Hexagonal	Wurzite	Diamond
Lattice constant (nm)	a=0.325 c=0.521	a= 0.319 c=0.519	a= 0.475 c=1.299	a=0.325 c=0.521	a=b=c =0.543
Epitaxial plane	(0001)	(0001)	(11 $\bar{2}$ 0)	(0001)	(100)
Lattice Mismatch	0	1.9% [113]	0.08% [113]	5.5% [88]	18.6%[114]

Although the vertical alignment of ZnO nanostructures can be assisted by an electric field, [80] in most cases, the alignment is realized by lattice matching between ZnO and the substrate. Several types of epitaxy substrates have been utilized, including sapphire, [115, 116] GaN [103, 104, 117-119] ZnO film coated substrate [118] SiC [88] and Si substrate [120-123]. Yang *et al* have grown vertical aligned ZnO nanowires array on sapphire (1120) plane [115]. Apparently the quality of vertical alignment is mainly determined by the lattice mismatch between ZnO and the supporting substrate.

2.4 Optical properties of metallic gold nanostructures

The optical properties of metal nanoparticles are especially striking differing from those of their bulk states due to either the quantum or dielectric confinement effect [124]. The former becomes important at the subnanometer scale while the latter is responsible for the surface plasmon resonance (SPR), the nanometer scale feature which is the origin of the observed colors in metal colloids [125]. The SPR is regarded as the collective excitation of the conduction band electrons. Under the influence of the electric field of an incident light beam, the ionic cores tend to move in the direction of the applied field, while the electrons are displaced in the opposite direction. The displacement of the heavier ionic cores is negligible in relation to electron displacement, and a net polarization results. Consequently, a restoring force develops at the nanoparticle (NPs) surface with the resulting excitation of the free electrons oscillations. Moreover, for gold NPs the absorption peak is positioned close to 550 nm [126]. The surface plasmon is very sensitive to particle size, surrounding medium and shape [125, 127-128].

The SPR has been explained theoretically by the Mie theory by taking into account both absorption and scattering of light in the small metal particles [129, 130]. The optical absorption coefficient K (cm^{-1}) due to a collection of absorbing spheres is given in the electric dipole approximation of the Mie theory as:

$$K = \frac{18\pi N V n^3}{\lambda} \frac{\varepsilon_2(\omega)}{[\varepsilon_1(\omega) + 2n^2]^2 + \varepsilon_2(\omega)^2} \quad (2.1)$$

where n is the index of refraction of the medium, N is the number of spheres per unit volume, V is the volume of the individual spheres, $\varepsilon_1(\omega)$ and $\varepsilon_2(\omega)$ are the frequency dependent dielectric constants of the metal, and λ is the wavelength of the light in the medium. The plasmon resonance maximum is therefore obtained when the denominator becomes a minimum, i.e. for $\varepsilon_1(\omega) = -2n^2$. Then by using the relation for the dielectric function of the metal [129, 131].

$$\varepsilon_1(\omega) = 1 - \frac{\omega_p^2}{\omega^2} \quad (2.2)$$

Therefore, the dipole or quasi-static approximation of the Mie theory holds for mean particle radii $R < 10$ nm, where no significant shift in the SPR peak is expected. In this size regime, a $1/R$ size dependence of the full-width at half-maximum (FWHM) of the absorption band is observed [129]. Hence, assuming a narrow size distribution within this size region, mean particle radii may be approximated as:

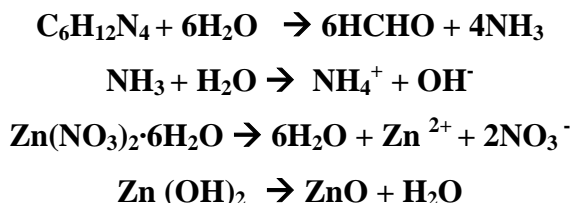
$$R = 1 - \frac{V_f}{\nabla\omega_{1/2}} \quad (2.3)$$

where R is the particle radius, V_f is the Fermi velocity of the metal and $\nabla\omega_{1/2}$ the FWHM for the absorption band in units of angular frequency [132]. The main assumption leading to Eq. 1.2 is that for the particle size range considered, R is less than the mean free path of electrons in the bulk metal [130] and therefore electron-surface scattering becomes an important relaxation process. Nevertheless, for larger particles the SPR band is significantly red shifted and subsequently becomes broadened making the $1/R$ approximation no longer suitable for particle size estimation. The Mie theory agrees well with experimental spectra of particles with $R > 10$ nm by considering the contribution of higher order resonance modes other than the electric dipole one (i.e. the SPR) [130]. Higher order modes such as the quadrupole one become evident with increasing particle size when the NPs are large in comparison to the incident radiation wavelength because the light can no longer polarize the particles homogeneously.

CHAPTER 3: LITERATURE REVIEW

Magnetron sputtering technique deposition is now one of the most versatile methods used for the deposition of transparent conducting oxides. This technique is characterized by the following advantages: low substrate temperature, good adhesion of the films on substrates, high deposition rates, and very good thickness uniformity [70]. This represents a relatively inexpensive deposition method. Magnetron sputtering is a convenient technique to make particle size in a uniform manner by sowing seed. In contrast to other methods which result in high polydispersity and a variety of shapes, this method offers narrow size distribution and near spherical particles [133-134].

Wet chemistry methods growth processes offer advantage of promoting only “seed growth”, this is controlled by changing the precursor concentration [135-136]. Shape-controlled synthesis of zinc oxide film is very important since almost all properties of ZnO nanorods or rods are dependent of shape and size. Thermal decomposition in a aqueous solution of zinc nitrate hexahydrate $Zn(NO_3)_2 \cdot 6H_2O$ and hexamethylenetetramine (HMT) ($C_6H_{12}N_4$) on a substrate is realized as follows.



The role of HMTA is still under debate. HMTA is a nonionic cyclic tertiary amine that can act as a Lewis base to metal ions and has been shown to be a bidentate ligand capable of bridging two zinc (II) ions in solution [137, 138]. HMTA is also known to hydrolyze, producing formaldehyde and ammonia in the pH and temperature range of the ZnO nanowires reaction [139-141]. In this case, HMTA acts as a pH buffer by slowly decomposing to provide a gradual and controlled supply of ammonia, which can form ammonium hydroxide as well as complex zinc(II) to form $Zn(NH_3)_4^{2+}$ [142, 143]. Because dehydration of the zinc hydroxide intermediates controls the growth of ZnO, the slow release

of hydroxide may have a profound effect on the kinetics of the reaction. Additionally, ligands such as HMTA and ammonia can kinetically control species in solution by coordinating to zinc (II) and keeping the free zinc ion concentration low. As reported by Sugunan et al. HMTA and ammonia can also coordinate to the ZnO crystal, hindering the growth of certain surfaces. It is believed that, in the chemical bath, hexamine being a non-polar chelating agent would preferentially attach to the non-polar facets of the nano-wires such as $(0\bar{1}0)$, (100) , $(\bar{1}10)$, thereby exposing only the (001) plane for a preferential growth as shown in Figure 12 [142].

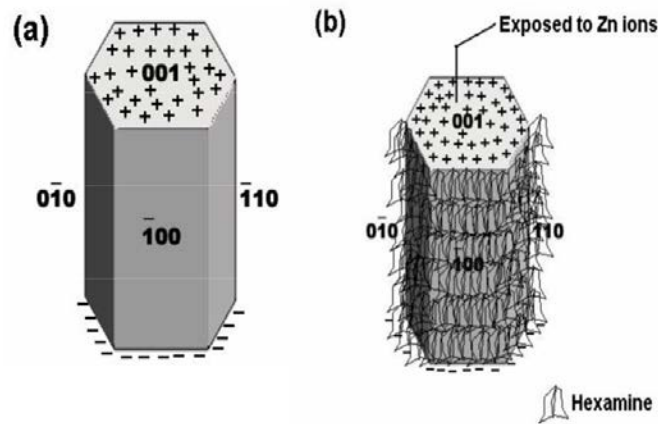


Figure 12. Schematic diagram of a) Role HMT and b) Exposed to Zn ions

Research efforts will focus on the manipulation of experimental variables such as mole ratios, reaction time and temperatures lower than 200 °C in aqueous deposition routes in order to optimize the corresponding plasmon resonance performance used by SERS. This phenomenon is based in collective oscillations of free electrons at metallic surfaces [144]. To describe the existence and properties of surface plasmons, one can choose from various models (quantum theory, Drude model). In addition, the work will deal with the optimization of the morphology and microstructures of selected nanorods and/or microrods. Nanorods should measure around 60 nm wide and 100 nm length. These dimensions are a function not only of chemical composition but also of crystal size variation.

ZnO NRs are excellent candidates in the development of biomolecular electronics, molecular switching devices, biosensors for medical diagnostics and gas sensors for environmental monitoring and chemical sensors by Surface Enhanced Raman Spectroscopy (SERS). [7,8-10]. Due to the physicochemical properties of these materials, size and shape are crucial for their activity or function [2]. On the other hand, ZnO nanotubes, nanorods and nanowires have gained much attention because they have a high surface area so the volume ratio makes them extremely sensitive to small surface changes [3-5]. Compatible with currently used microelectronics technology, the development of sensor devices is possible.

The electromagnetic (EM) and chemical mechanisms are based upon the optical properties of the noble metals Ag, Au, and Cu, and their ability to support the inelastic scattering increase. This enhanced scattering process is known as surface-enhanced Raman scattering (SERS). SERS is a powerful and non-destructive technique that has demonstrated to be sensitive and selective for molecular identification. Recently, SERS has been used extensively as a signal transduction mechanism in biological and chemical sensing [6]. Fundamental theory of the mechanisms responsible for the SERS enhancement remains an active research topic since the discovery of the phenomenon; two major factions have disagreed on the relative significance of the proposed mechanisms, chemical enhancement and electromagnetic enhancement [145]. In the chemical mechanism, which is now thought to contribute an average enhancement factor of 100, a charge-transfer state is created between the metal and adsorbate molecules. This mechanism is site-specific and analyte-dependent. Observations confirm that surface plasmon oscillations are involved in the intense Raman Scattering already reported for molecules adsorbed at roughened silver surfaces [9]. To understand the electromagnetic enhancement, one must consider the size, shape, and material of the nanoscale roughness features [9]. These characteristics determine the resonant frequency of the conduction electrons in a metallic nano-structure. When electromagnetic radiation with the same frequency is incident upon the nanostructure, the electric field of the radiation drives the conduction electrons into collective oscillation and there is an enhancement of the electromagnetic field at the surface at both the incident and Raman scattered wavelengths. This enhancement in turn induces a change in polarizability

of the molecule leading to intense Raman signals [145, 146].

The most frequently used SERS substrates are silver and gold colloids and silver/gold bimetallic colloids. These are mainly produced by reduction of silver nitrate or chloroauric acid with sodium citrate, the so-called Lee-Meisel method [147], or by reduction of silver nitrate or chloroauric acid with sodium borohydride following the Creighton procedure [148]. Aside from these, other reducing methods have also been reported for preparing SERS-active colloids.

In the absence of suitable stabilizing agents, colloidal particles would be attracted to each other by van der Waals forces, ultimately resulting in the coagulation and precipitation of the sol [149]. This is prevented by the use of a stabilizer/ capping agent, which sets up a repulsion barrier between the approaching particles. Stabilization is generally achieved by two methods: (a) electrostatic [150] and (b) steric [151]. The electrostatic stabilization involves the use of charged capping agents. Sodium citrate [152] is a commonly used capping agent. Citrate-capped nanoparticles are negatively charged and they attract positively charged counter-cations from the solution. This arrangement results in the formation of a diffuse electrical double layer and consequently a Coulombic repulsion between the particles. As long as the electric potential associated with the double layer is high, electrostatic repulsion between the particles will prevent agglomeration. However, the double layer is very sensitive to changes in temperature, and in particular the ionic strength of the solution. An increase in the ionic strength by the addition of a salt causes a compression of the double layer and shortens the range of repulsion. Reduction of the charge on the colloid by the addition of a neutral, strongly binding adsorbate, which displaces the adsorbed citrate anions, would also result in agglomeration [153].

The search for silver and gold substrates for SERS studies has led to very intense research in this field. Preparation and stabilization of these types of substrates have many problems associated with using SERS as an analytical technique [153]. The difficulty has been associated with producing reproducible SERS substrates. Variations in the morphology of SERS substrates can give rise to large differences in the signal intensity. The goals of this study are to prepare gold coatings over ZnO nanorods or rods. These nanorods should

exhibit chemical properties and thermodynamic stability associated to their size, which improve the present problem of steric stabilization that silver and gold colloids suffer.

Successful application of nanotechnology opens new opportunities for building of nanostructures of materials by different synthesis routes few studies have been carried out using ZnO nanocrystals for SERS detection of molecules. Studies on several molecules such as 4-mercaptopyridine and 4-mercaptobenzoic acid adsorbed on the surface of ZnO nanocrystals as a function of particle size in the range of 18 – 31 nm diameter, have shown an indication of a size-dependent charge-transfer resonance [3]. This effect was attributed to formation of a charge-transfer complex between a surface-bound exciton and the adsorbed molecule [154]. Many authors have discussed the development of the current nanotechnologies, improving its quality and efficiency through the different applications of ZnO nanomaterials [1].

CHAPTER 4: METHODOLOGY

4.1 Experimental Procedures

4.1.1 Materials

All reagents used were of analytical grade. The sputtering target used for the deposition of the base films consisted of zinc oxide listed as follows:

- ZnO target of 99.99% purity, 0.15” thick and 2” diameter produced by Superconductor Materials Inc. The p-type Si (100) and indium tin oxide (ITO) 15-25 Ω/SQ^2 substrates were purchased from Sigma Aldrich.
- In the deposition of ZnO rods in aqueous phase, zinc nitrate hexahydrate, $Zn(NO_3)_2 \cdot 6H_2O$ and hexamethylenetetramine (99.99%, Sigma-Aldrich Chemical Co) were used to synthesize and deposit ZnO rods onto the above-mentioned sputtered base films.

4.1.2 Preparation of Substrates

In this study, p type silicon (100) and ITO slides were used as substrate material. The substrates were cut into 1 cm x 1 cm pieces. The Si (100) and ITO glass microscope substrates were cleansed with 70% (v/v) high purity water and 30% (v/v) acetone and were sonicated for two hours. The substrates were dried and kept in oven until they were loaded into the deposition chamber of the magnetron-sputtering instrument.

4.1.3 Synthesis of ZnO base films

Radio frequency (RF) magnetron sputtering was used for RF excitation for the potential distributions using a ceramic target of ZnO as shown in Figure 6b. The optimization steps were achieved through the influence of deposition parameters such as substrate to target

distance (between 7 and 10 cm width) on the structural, optical and electrical properties of ZnO films. The rods-formation processes were divided into two stages: the nucleation and the growth stage. The nucleation on the substrate is very important to form good quality films. In addition, the temperature control and reaction time were crucial for satisfactory results. For instance, the ZnO base films were prepared by radiofrequency with power between 50 to 150 watt with time intervals between 10 and 30 minutes under argon atmosphere at 1×10^{-3} torr at 120 and 200 ± 2 °C. A summary of parameters for sputtering deposition are shown in Table 2. This temperature was measured with a thermocouple, which was in contact with the top plate of the substrate holder.

Table 2 Parameters of Sputtering Deposition of Zn

Target- substrate distance	6-10 cm
Sputtering pressure	1×10^{-3} torr
Gas flow	40 cc/min
Rf power	50 -150 W
Sputtering time	10 to 30 min
Substrate temperature	120 and 200 ± 2 °C

Subsequently, the films were washed with 70% (v/v) high purity water and 30% (v/v) acetone and sonicated for two hours to continue the thermal decomposition of zinc nitrate and hexamethylenetetramine.

4.1.4 Synthesis of ZnO NRs.

ZnO rods were synthesized from the thermal decomposition of zinc nitrate hexahydrate / hexamethylenetetramine (HMT) in aqueous phase [140, 155, 156]. The ZnO base /Si film deposited by RF magnetron sputtering was immersed in a glass beaker containing the $\text{Zn}(\text{NO}_3)_2 \cdot 6\text{H}_2\text{O}$ and HMT at concentrations of 0.001 to 0.1 M, ZnO base were placed vertically at the bottom of the glass bottle, showed in Figure 13.



Figure 13. System used for ZnO NRs synthesis by wet chemistry method.

The reacting solution in contact with the film was refluxed in 65-95 °C intervals for 1.5 to 24 hours. At the end of the contact time, treated films were removed from the Zn-HMT solution and thoroughly washed with high purity water (MilliQ 18.2 MΩ cm) to remove any residual amino complex during 15 minutes. The ZnO nanorods were placed in the oven at 200 °C for 10 minutes.

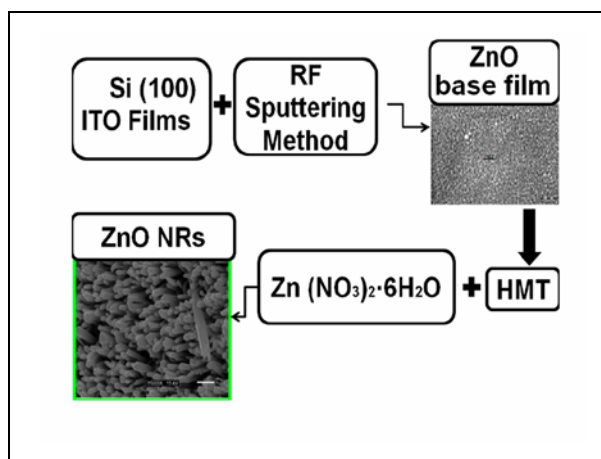


Figure 14. Flow diagram from growth-controlled synthesis of ZnO-NRs in aqueous phase has been investigated. ZnO-NRs were grown on ZnO films previously deposited onto Si (100) and indium tin oxide (ITO) substrates by RF magnetron sputtering and then characterized by several techniques.

4.2 Material characterizations

X-Ray diffraction (XRD) experiments were carried out in a Siemens D5000 (XRD) using the Cu-K α radiation (1.5405Å). SEM analyses were conducted on a JEOL-JSM 6500 instrument and a Philips/ FEI, XL30s, FEG SEM / Phoenix EDAX. Optical properties of ZnONR and ZnO rods were measured using a UV-vis DU 800 spectrophotometer and the photoluminescence spectra were acquired with a HORIBA Jobin Yvon FluoroLog-3 spectrofluorometer under excitation at 350 nm.

4.2.1 X-Ray Diffractometry (XRD)

XRD is one of the most powerful techniques for qualitative and quantitative analysis of crystalline compounds [157]. This experimental technique was used for determining the structure and orientation of ZnO NRs thin films. Experiments will be carried out in a Siemens D500 x-ray diffractometer (XRD) located at the Engineering Science and Materials Department using the Cu-K α radiation (1.5405Å). The x-ray scans were performed between 2θ values of 20° and 70°.

X-ray diffraction is a nondestructive technique, and is one of the widely used for determining lattice parameters, preferred orientation of the crystal, phase composition (qualitatively and quantitatively), grain sizes, lattice strain, residual stress. XRD can provide the information from a relative larger area of the specimen compared to TEM. Bragg's law describes the angle ($2\theta_{hkl}$) formed between the incident beam and the diffracted beams. This equation has the form: [157]:

$$2d\sin\theta = n\lambda \quad (4.1)$$

where n is integer that indicates the order of the reflection, θ is Bragg angle, and λ is the wavelength of the incident radiation, d_{hkl} is an interplanar spacing. In our case, the Cu-K α radiation ($\lambda=1.54056\text{Å}$) was used, and the crystalline phases and orientation were identified by matching the XRD peaks with those given in the data base of the program MATCH [158].

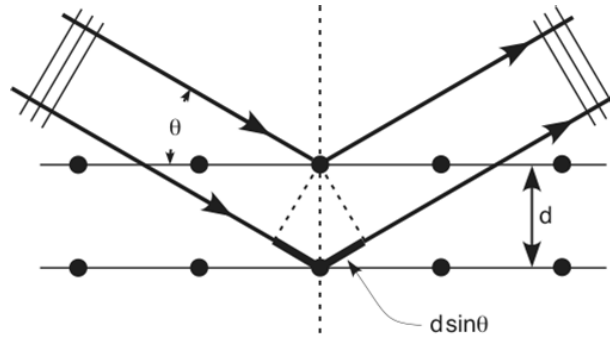


Figure 15. Schematic diagram of Bragg's diffraction from a set of parallel planes[159].

Furthermore, the lattice parameters are related with Miller indexes (hkl) of each reflection plane and interplanar distance (d_{hkl}). For example for ZnO NRs possess a hexagonal structure, so the lattice parameter can be determined from the following equation:

$$\frac{1}{d_{hkl}^2} = \frac{4}{3} \left(\frac{h^2 + hk + k^2}{a^2} \right) + \frac{l^2}{c^2} \quad (4.2)$$

On the other hand, the average crystallite size may also be determined by using Scherrer's equation.

$$D = \frac{K\lambda}{B \cos \theta} \quad (4.3)$$

Where D is the particle diameter, θ is the diffraction angle, and B is the full width at the half high maximum (FWHM). The factor K involves different instrumental aspects, such as geometry, penetration of X-ray in the sample. From the width of the diffraction peak using the Scherrer's equation, one can calculate the average particle size, h , k , and l are the Miller indexes, a and c are the lattice parameter [159].

4.2.2 Field Emission Scanning Electron Microscope (FE-SEM) and Energy Dispersive Spectroscopy (EDS)

The analyses were carried out at two different places. The first one corresponds to

the use of a Philips/ FEI, XL30s, FEG SEM / Phoenix EDAX located at the Lab of Hewlett Packard-PR – Aguadilla. The second microscope used a JEOL-JSM 6500 instrument and located at the Chemical Engineering Laboratory in UPR-Mayaguez.

FE-SEM examines the morphology and determines the grain and rod size. Therefore is important to determine the size of the seed for the optimization of ZnO NRs.



Figure 16. Image of a Philips/ FEI, XL30s, FEG SEM / Phoenix EDAX located at the Lab of Hewlett Packard-PR – Aguadilla.

Accelerated electrons in an SEM carry significant amounts of kinetic energy, and this energy is dissipated as a variety of signals produced by electron-sample interactions when the incident electrons are decelerated in the solid sample [160]. These signals include secondary electrons (that produce SEM images), backscattered electrons, diffracted electrons, photons, visible light, and heat. Secondary electrons and backscattered electrons are commonly used for imaging samples: secondary electrons are most valuable for showing morphology and topography on samples and backscattered electrons are most valuable for illustrating contrasts in composition in multiphase samples.

The interaction between the incident electrons and the atoms of the specimen leads to a variety of different signals. The information obtained (composition, structure, etc.) will depend on the kind of signal used to form the image. Important signals for our purposes are those that give rise to bright field images.

EDS is an analytical technique used for elemental analysis or chemical characterization of a sample. The sample is excited with the interaction of an X-ray source. Its characterization capabilities are due in large part to the fundamental principle that each element has a unique atomic structure allowing unique set of peaks on its X-ray spectrum. At rest, an atom within the sample contains ground state (or unexcited) electrons in discrete energy levels or electron shells bound to the nucleus. The incident beam may excite an electron in an inner shell, ejecting it from the shell while creating an electron hole where the electron was an electron from an outer, higher-energy shell then fills the hole, and the difference in energy between the higher-energy shell and the lower energy shell may be released in the form of an X-ray [159]. The number and energy of the X-rays emitted from a specimen can be measured by an energy-dispersive spectrometer. As the energy of the X-rays are characteristic of the difference in energy between the two shells and of the atomic structure of the element from which they were emitted, this allows the elemental composition of the specimen to be measured [157].

4.2.3 Absorption spectroscopy

One widely used method of optical characterization is the absorption from the infrared to the ultraviolet range. When an incident light beam interacts with a medium, part of the beam will be reflected on the medium surface, part of the beam will be transmitted through the medium, and the rest of the beam will be absorbed. Absorption of photons arises due to the transition of the electrons from lower energy levels to the higher energy levels.

The absorption ability of a matter is measured by its absorption coefficient. The absorption coefficient, α , for a uniform medium can be defined in terms of the intensity change of a monochromatic light beam in unit distance that the beam traveled in the medium. Therefore, the beam intensity as a function of the distance x can be written as:

$$I(\lambda) = I_0(\lambda)e^{-\alpha(\lambda)x} \quad (4.4)$$

On the other hand, absorption coefficient is a function of frequency (or wavelength). The variation of absorption coefficient with wavelength is called the absorption spectrum of the medium.

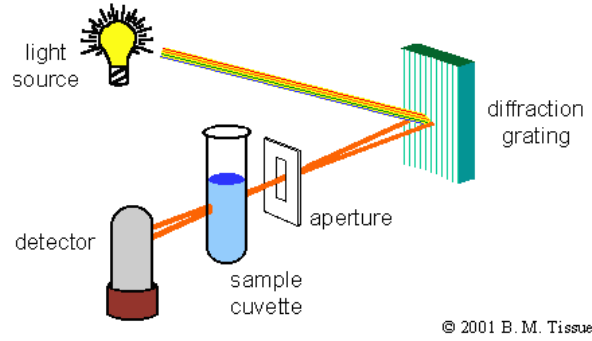


Figure 17. UV-vis spectrometer setup [158].

An absorption spectrometer (or transmission spectrometer) is generally composed of one or two monochromators, a continuous light source, and a photomultiplier. The spectrometer is equipped with two continuous light sources - a W lamp for measuring in the visible range (from 1000 nm to 320 nm) and a deuterium lamp for the measurement in ultraviolet range (from 320 nm to 200 nm). In our case, this technique was used to evaluate the optical properties of ZnO-base film and ZnO NRs based thin films, in the wavelength range between 200 nm and 800 nm.

The absorption characteristics of all the samples, at first the transmittance (T) at different wavelengths (λ) are measured and then absorbance (α) at the corresponding wavelengths λ are calculated using the Beer-Lambert's relation [161].

$$\alpha = \frac{1}{d} \ln\left(\frac{1}{T}\right) \quad (4.5)$$

where, d is the path length. The absorption edge for single crystal ZnO is very sharp and is determined by the nature of the electronic transition between the valence band and conduction band. The absorption edge for a suspension of nanoparticles is much broader and is determined by the distribution of particle size [162].

4.2.4 Photoluminescence

The photoluminescence spectra were acquired with a HORIBA Jobin Yvon FluoroLog-3 spectrofluorometer under excitation at 350 nm in the Nano-Materials Lab at New College of Florida, Sarasota, FL.

In photoluminescence spectroscopy, the sample is excited with a light with energy higher than the bandgap energy, and the emitted radiation is measured as a function of energy. The excitation creates electron-hole pairs which thermalize rapidly. The emitted light is produced by the radiative recombination of these pairs. The most important radiative recombination centers are donors and acceptors, where the electrons and holes can be localized by themselves or after forming a common bound state called an exciton. Hence in a photoluminescence spectrum four different types of optical transitions are observed: band-to-band (no localization), free-to-bound (either hole or electron is localized), donor-acceptor-pair (both the hole and the electron are localized) and exciton recombination (either free or bound). In conclusion, PL spectrum provides information about the structure of energy levels in the sample. The excitation spectrum is actually an absorption spectrum, which is obtained by monitoring the luminescence at a specific wavelength, i.e. at the peak of emission of interest. Therefore, the excitation spectrum is used to locate the energy levels of the excited states in the monochromator, white light from a xenon lamp is collected by an elliptical mirror and directed to the entrance slit. Then the light is dispersed through the grating and then is directed to the exit slit of the monochromator (for excitation). A specific wavelength is selected by the monochromator from the incoming light. The entrance and exit ports (or slits) of the spectrometer and the monochromator are adjustable in increments of 25 μ m. These are computer-controlled slits. To be able to detect the lamp profile of the output beam, a photodiode is used. The slits of the monochromator determine the amount of monochromatic light that is used to illuminate the sample. The spectrometer slits, on the other hand, control the intensity and resolution of the fluorescence signal that is detected by the photomultiplier (PMT). The PMT signals are amplified and processed.

4.2.5 SERS and Raman Spectrometry

A Renishaw Raman Microspectrometer RM2000 was employed for the vibrational spectroscopy measurements. The system is equipped with a Leica microscope. Sample detection was achieved at 785 nm wavelength. Experiments were performed at lab conditions (room temperature). The laser spot size on the focused samples was rectangular in shape, with dimensions: 50 μm x 90 μm . Laser power was kept on the sample head at 170 mW for 785 nm with the beam 100 % setting in the Wire Renishaw Software. The spectra were obtained in the range of 100-3500 wavenumbers (cm^{-1}) [9], 10 scans and 30 s of integration time.



Figure 18. Renishaw Raman Microspectrometer (RM2000) with Leica objectives with 10x magnification used.

5 RESULTS AND DISCUSSION

5.1 Optimization of synthesis parameters

Zinc oxide nanorods (ZnO NRs) have been investigated through this work with the purpose of optimizing growth parameters and size control. ZnO NRs were grown on Si (100) and indium tin oxide (ITO) glass substrates using zinc nitrate hexahydrate and hexamethylenetetramine as precursors. During the preparation of the ZnO base film, ZnO was first deposited using RF magnetron sputtering, and afterwards, a wet chemistry procedure was performed for ZnO NRs growth. The base film was able to aid in the uniform growth of well-aligned ZnO NRs. The ZnO NRs grown were characterized using X-ray diffraction, scanning electron microscopy (SEM), field emission SEM, optical absorption and photoluminescence spectroscopy. Diameter controls of the well-oriented and high-quality ZnO NRs are achievable during growth by adjusting parameters such as temperature, reagent concentration and reaction time. The ZnO NRs grown possess varying sizes in diameter (60 and 500 nm) and lengths well exceeding 3 μm . ZnO NRs/ZnO base film/ITO exhibit a strong UV absorption around 360 nm. Photoluminescence spectra presented narrow near-band-edge (NBE) dominant peak at 380 nm which indicate a relatively higher oxygen vacancy concentration in the ZnO NRs grown on ZnO/ITO in comparison with those on the ZnO/Si (100).

5.2 Deposition on substrate

Deposition of ZnO base film on the substrate is necessary to provide nucleation sites. This was achieved by fixing pre-synthesized ZnO base film by sputtering on the substrate (seeding). The results were both an improvement of the orientation along the c-axis and aspect ratio of the obtained rods [163].

The growth of ZnO NRs in the vertical orientation is usually substrate independent. Magnetron sputtering offers a fairly good control over the orientation and morphology of the obtained nanorods. Figure 19 shows ZnO NRs without ZnO base film deposited on Si(100) and demonstrate that the growth in the c-axis of the nanorods depends on nucleation sites

which can be introduced by depositing a layer of ZnO base film by sputtering.

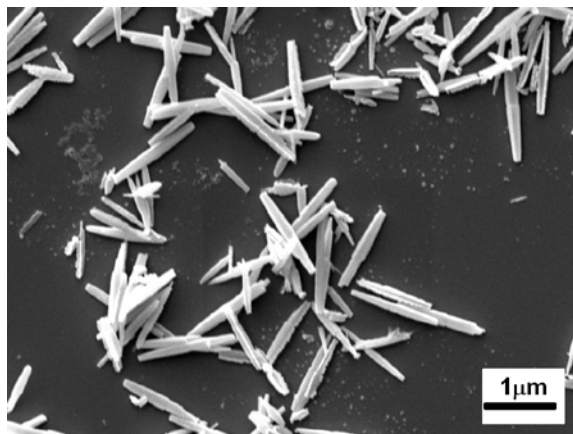


Figure 19. FE-SEM images of ZnO NRs on Si (100) without using pre-synthesized ZnO base film by sputtering.

5.3 ZnO NRs formation at temperatures below 200 °C

The heating at elevated temperatures and the consequent slow rise in pH, during the wet chemistry method, could be a factor that contributes to the degradation of hexamine and consequently precludes formation of ZnO NRs. A noticeable difference in morphology is observed for ZnO NRs grown on heated chemical baths at up to 200 °C by wet chemistry. In contrast, at 95 °C there is a significant variation of morphology for grown nanorods as seen from SEM images (Figure 20).

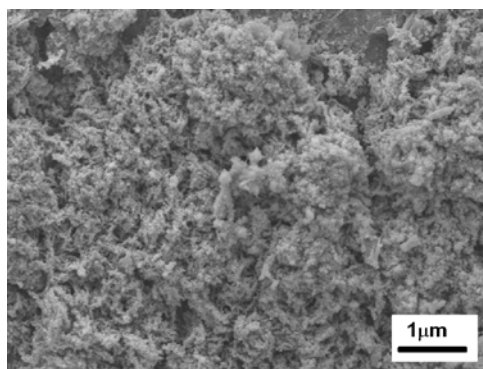


Figure 20. FE-SEM images of the solids synthesized by wet chemistry at 200 °C.

5.4 Sonication treatment for uniformity of films.

To remove both any residual amino complex and the ZnO rods which did not fix on the substrate; sonication was carried out during 15 minutes as shown in Figure 21. The ZnO nanorods were then placed in the oven at 200 °C for 10 minutes.

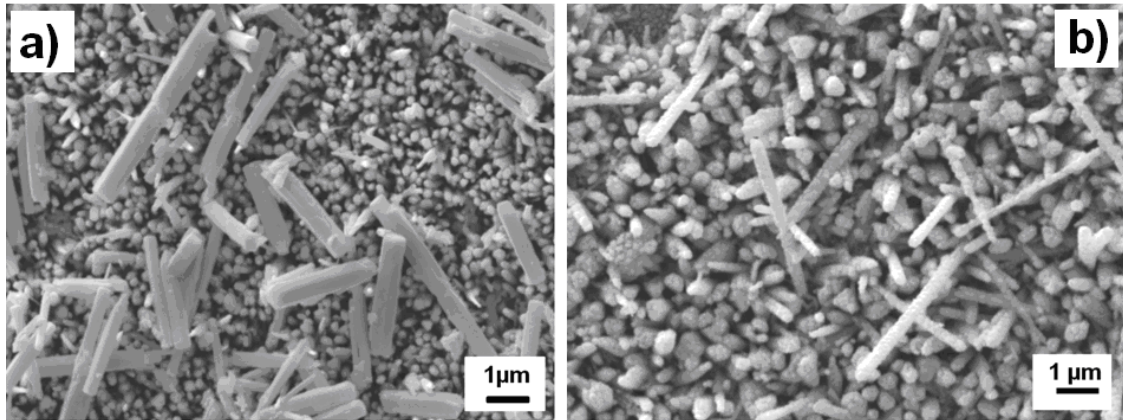


Figure 21. SEM image of ZnO rods deposited onto ZnO layer on Si (100) substrate. The rod synthesis temperature was 95 °C 7 hours: a) without sonication and b) sonicated.

5.5 ZnO base film/ITO

5.5.1 Effect of temperature on the deposition of ZnO base film/ ITO by sputtering

A. XRD Analyses

Figure 22a shows the XRD patterns of ZnO base film/ ITO deposited by RF magnetron sputtering. The (002) diffraction peaks were highly oriented, although the (101), (102) and the (110) reflections were also observed. The average crystallite size, calculated from the (002) peak employing the Debye-Scherrer formula, was 10 nm for a deposition temperature of 200 °C and 5 nm at 120 °C. ZnO base film/ITO at 120 °C showed preferential growth in the (002) plane as observed in Figure 22b. By use of a lower deposition temperature, it was proved that nucleation sites [164] could be achieved by depositing a layer of ZnO by sputtering or spin coating. This resulted in improvement of the aspect of the deposited material on the substrate (seeding). According to recent reports, this

should result in better uniformity [3] by introduction of improved aspect diameter of the ZnO NRs.

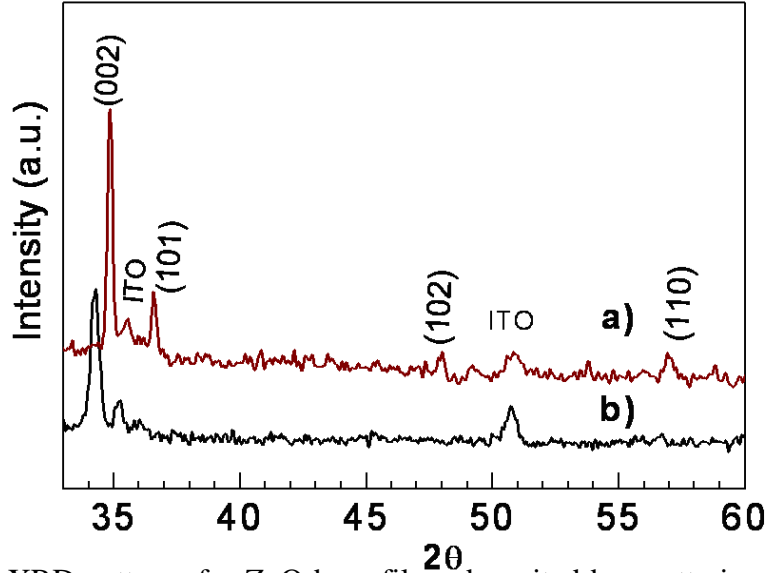


Figure 22. XRD patterns for ZnO base films deposited by sputtering on 15-25 $\Omega/\text{SQ2}$ ITO substrates at a) 200 °C, b) 120 °C and 10 min of deposition time.

Table 3 summarizes the data collected from the XRD analysis of ZnO base film on ITO deposited at different temperatures by magnetron sputtering. It should be noted that at the higher temperature (200 °C), four different planes [(002), (101), (102) and (110)], are clearly discernible. On the other hand, at the lowest temperature used (120 °C) only the (002) plane predominates. In addition, use of a lower temperature for deposition led to the formation of a structure with a smaller crystallite size when compared to every observed plane at the higher temperature used. The thickness of the ZnO base films was measured using a surface profilometer XP- 200 model high performance in the Speclab at University of Puerto Rico at Río Piedras, Puerto Rico. The thickness of the ZnO layer is presented in Table 3.

Table 3. Average crystallite size of ZnO base film/ITO deposited at different temperatures by magnetron sputtering.

Substrate deposition temperature	ZnO/ITO (200 °C)				ZnO/ITO (120 °C)
	Plane	(002)	(101)	(102)	(110)
Peak Position (2 θ)	34.78	36.49	47.05	57.12	34.33
FWHM ($^{\circ}$)	0.85	0.40	0.44	0.43	1.6
D Crystallite size (nm)	9.63 ± 0.04	20.5 ± 0.9	19.37 ± 0.03	20.7 ± 0.3	5.11 ± 0.03
Film Thickness (nm)	198				60
Average crystallite size (nm)	17.55 \pm 0.03				

B. Field Emission SEM Analyses

In order to attain additional insights on the morphological features of our samples, base films were prepared and ZnO deposits were analyzed by field-emission scanning electron microscopy. In general, during the deposition at 200 °C, the observed morphology of ZnO base film/ ITO is that of a flake and some nanoparticle. This was expected since there were different crystallographic planes formed as was mentioned previously in XRD analysis. The deposition of ZnO base film/ITO resulted in an average crystallite size of about 17.55 nm from XRD and FE-SEM image of about 220.85 nm as observed from Figure 23a. ZnO base film/ITO at 200 °C exhibited various grain sizes for the ZnO arrays compared to the observed morphology for the deposition at 120 °C (Figure 23b). ZnO base film/ITO at 120 °C showed that the ZnO thickness decreased to 64.77 nm. This suggests that deposition at a lower temperature resulted on a diminished grain size. However, for the highest temperature there are observed different sizes in the flake-like nanoparticles formed by

sputtering deposition with a grain size average of 220.85 nm and a standard deviation (SD) of 105.06 using the ImageJ program for scientific imaging processing and comparable with the film thickness of about 198 nm.

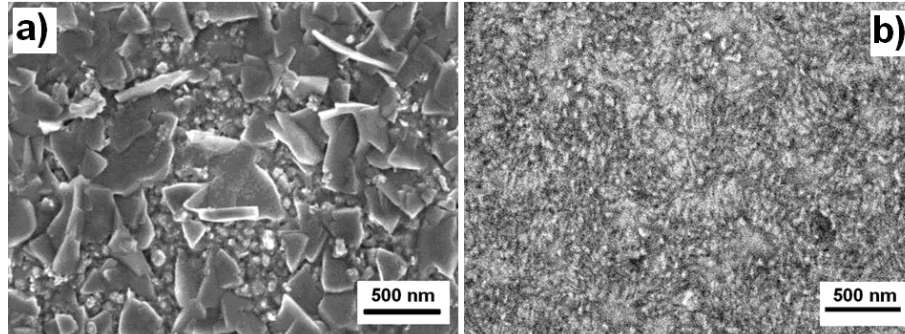


Figure 23. FE-SEM images of the ZnO base film/ITO film deposited by RF magnetron sputtering for 10 min at a) 200 °C; b) 120 °C. Grain Size for the the ZnO base films was 220 nm (SD 105) for 200 °C and 65 nm (SD 24) for 120 °C.

Considering the above-mentioned Section 5.5.1.A, at higher temperature for base film deposition, the nanocrystalline domains formed via sputtering growth on Si (100) substrate resulted in aggregation of apparently dispersed plates. Therefore, the advantages of sputtering in the nucleation of a coat of small seed crystals provide a more complete coverage of the substrate and a better coherent surface-textured film which resulted at 120 °C. On the other hand, at a higher temperature close to 200 °C, fewer columns that grow to larger diameter are favored. At a higher heating temperature of the substrate, grains of a larger size were obtained while maintaining uniform coverage.

5.6 Effect of deposition time on ZnO base film/ITO by sputtering

A. XRD Analyses

Fig. 24 shows the XRD patterns of ZnO base film/ITO for 10 and 30 minutes shown in Figures 24a and 24b, respectively. Use of a 10-minute deposition time during sputtering, resulted in a wurtzite structure obtained for ZnO base film/ ITO. The prevalence of the (002) plane shows the strongest characteristic orientation [19]. The characteristic planes for ZnO appear as weak peaks for the (101) and (102) planes in this film (Figure 24a).

When the deposition time was almost 30 minutes, an increase in the intensity of the (002) plane with respect to the (101), (102) and (110) crystallographic planes was obtained. Nonetheless, the (002) plane had a higher preferential orientation than the other planes as shown in Figure 24b. This is evidence of the c-axis texturing.

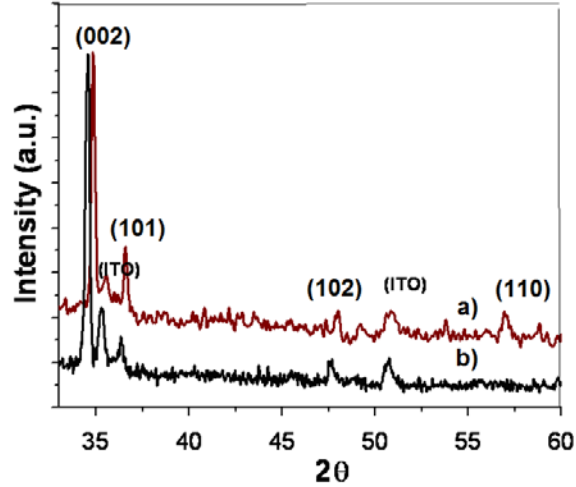


Figure 24. XRD patterns of the ZnO NRs/ZnO base film/ITO film deposited by RF magnetron sputtering for 120 °C for: a) 10 min and b) 30 min.

As seen in Figure 24, there is a shift of the peak's 2θ value for the (002) plane on increasing the deposition time from 10 a) to 30 minutes b). The reference value for the interplanar spacing for bulk ZnO is 2.60Å. Application of Bragg's law yields an interplanar distance of 2.5 Å for 30 minutes of deposition. These values reflect the effect of compression strain as shown in Figure 24. [159].

Table 4. Average crystallite size of ZnO base/ITO film deposited at different times by magnetron sputtering.

Substrate	(002) Peak Position		D
	(2θ)	FWHM ($^{\circ}$)	Crystallite size (nm)
ZnO/ITO (30 min)	34.81	0.43	19.0± 0.1
ZnO/ITO (10 min)	34.42	0.45	18.02± 0.05

B. Field Emission SEM Analyses

The FE-SEM images shown in Fig. 25 correspond to the ZnO/ITO base film. As with the Si (100) substrate, the films also seem uniform and compact again suggesting good sputtering deposition quality. When comparing Figs. 25a and 25b, the morphological features in both types of ZnO base films are evident. Deposition for 30 min led to a grain size of 324 nm (SD 0.080) with a thickness of about 305 nm. While for 10 min of deposition time afforded a grain size of 64.77 nm (SD 23.71). While ZnO grains were more or less equiaxial when ZnO was deposited at 120 °C for 30 min, the grains become densely packed in an irregular array. They exhibited elongated shape when ITO was deposited at 120 °C for 10 min.

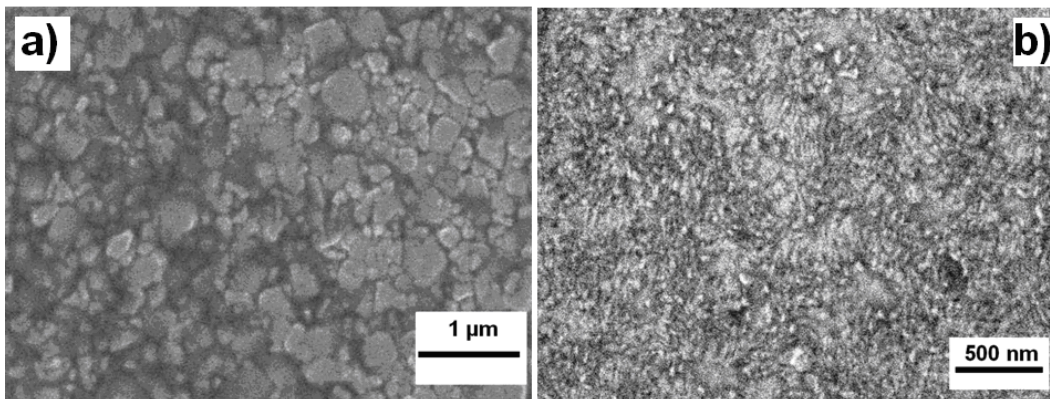


Figure 25. FE-SEM images of the ZnO base film/ITO film deposited by RF magnetron sputtering at 120 °C for (a) 30 min and (b) 10 min. Grain Size for the the ZnO base films were 324.02 nm (SD 0.08 for 200 °C and 64.77 nm (SD 23.71) for 120 °C.

On the other hand, we can observe in comparison of the Figure 25 that the deposition temperature has a direct relationship with the particle size. Figure 25b showed a lower average grain size estimated at $18.02 \text{ nm} \pm 0.05$ using the Scherrer's formula and thickness was about 20 nm.

5.7 ZnO base film/ Si (100)

5.7.1 Effect of temperature treatment on phase deposition of ZnO base film/ Si (100) by sputtering.

A. XRD Analyses

XRD patterns shown in Figure 26 show the effect of temperature obtained ZnO base films/ Si (100) deposited by sputtering under the conditions mentioned below. XRD analysis of both samples evidenced very strongly oriented structure in the (002) plane. The peaks observed correspond to a typical wurtzite hexagonal structure for ZnO with a preferred orientation on the c-axis perpendicular to the substrate. However, at a higher temperature deposition for ZnO base film/ Si (100) it was observed that the (101) plane is present but it is less intense than the corresponding (002) plane as shown in Figure 26a.

Figure 26b shows the (002) plane at a 2θ value of 34.37 (see also Table 3). His value was slightly shifted toward lower diffraction angles in the pattern with respect to the standard value at $2\theta = 34.422^\circ$. Apparently the quality of vertical alignment is mainly determined by the lattice mismatch between ZnO and the supporting substrate [20].

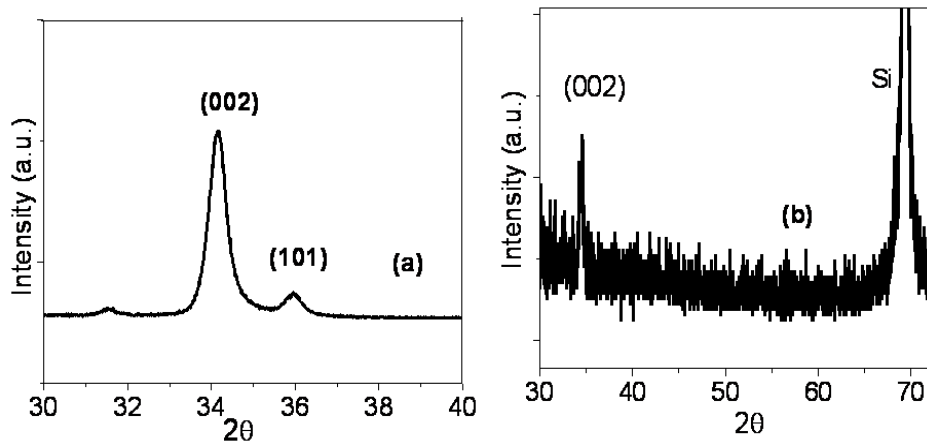


Figure 26. XRD patterns for ZnO base films deposited by sputtering on Si (100) substrates at: (a) 200 °C, (b) 120 °C and 10 min of deposition time in both samples.

Table 5. Average crystallite size of ZnO base/ Si (100) film deposited at different temperatures by magnetron sputtering.

Substrate Deposition temperature	(002)Peak	FWHM ($^{\circ}$)	D
	Position (2θ)		Crystallite size (nm)
ZnO/Si (100) (200 $^{\circ}$ C)	34.19	1.96	4.17 \pm 0.03
ZnO/ Si (100) (120 $^{\circ}$ C)	34.37	1.88	4.35 \pm 0.02

B. Field Emission SEM Analyses

FE-SEM images shown in Fig. 27 correspond to the ZnO/Si (100) base films grown by RF magnetron sputtering at different deposition temperatures. The films appear highly compact on deposition at the lower temperature (120 $^{\circ}$ C), which suggest a good quality deposition. The grain size is 148.09 nm as seen in Figure 27a. The grains become densely packed in a near regular array and are considered as seeds for the growth of the corresponding rods. At a lower deposition temperature, the grain size is thinner resulting in a more uniform and compact texture of the ZnO base film when compared with the higher temperature (200 $^{\circ}$ C) employed. The grain size average was approximately 19.65 nm and a comparable thickness of about 20 nm as observed in Figure 27b.

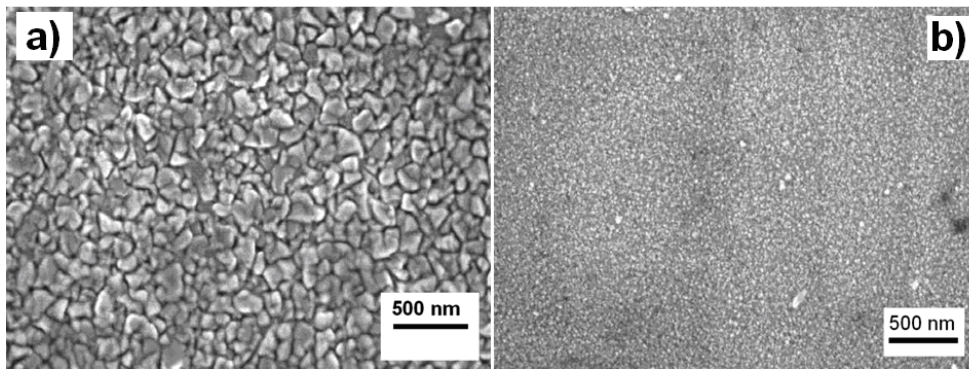


Figure 27. FE-SEM images of the ZnO base film/ Si (100) film deposited by RF magnetron sputtering for 10 min at a) 200 $^{\circ}$ C and b) 120 $^{\circ}$ C. Grain size for the ZnO base films were 148.09 nm (SD 33.91) for 200 $^{\circ}$ C and 19.65 nm (SD 19.65) for 120 $^{\circ}$ C.

5.8 Effect of deposition time on ZnO base film/Si (100) by sputtering

FE-SEM images shown in Fig. 28 correspond to the ZnO/Si (100) base films grown by RF magnetron sputtering at different deposition times. The morphological behavior corresponding to a good quality deposition is very similar to the results obtained by the effect of deposition temperature. The grain size was between 500 nm and 1.0 μm for the longer deposition time (30 min) compared to a grain size average of approximately 50 nm for the shorter (10 min).

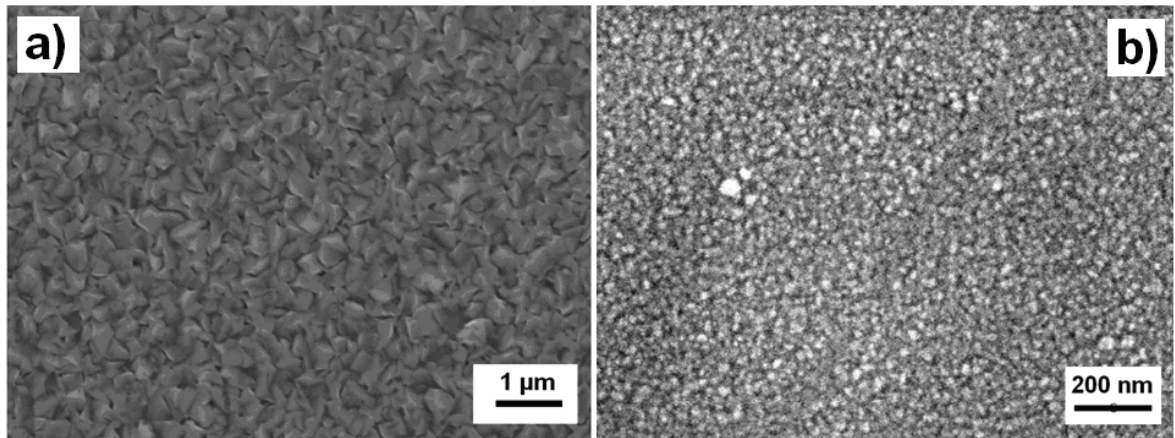


Figure 28. FE-SEM images of the ZnO base film/Si (100) film deposited by RF magnetron sputtering at 120 °C for: (a) 30 min; (b) 10 min. Grain Size for the the ZnO base films were 331 nm (SD 0.059) for 30 min and 20.91 nm (SD 4.73) for 120 °C for 10 min.

5.9 ZnO NRs/ ZnO base film/ITO

5.9.1 Effect of temperature treatment on growth of ZnO NRs deposited on ZnO base film/ ITO by magnetron sputtering.

A. XRD analyses

The X-ray diffraction patterns corresponding to the ZnO/ITO substrates and the ZnO deposited onto this base are shown on Figures 29a and 29b, respectively. In both samples, the diffraction patterns clearly show the preferential growth along the (002) plane in the wurtzite structure of ZnO. However, some ZnO NRs did not grow in the c vertical axis due to the weaker appearance of the (101) and (102) planes. This suggest the formation of a well organized columnar structure along the c-axis direction perpendicular to the substrate. The peak at a 35.4° corresponds to the ITO substrate.

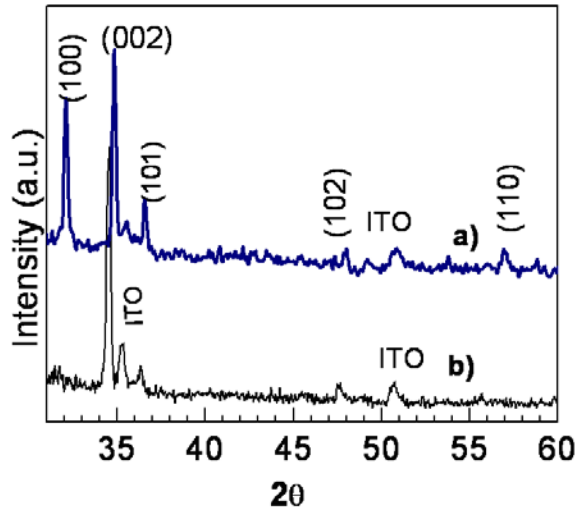


Figure 29. XRD patterns for ZnO NRs/ ZnO base films deposited by RF magnetron sputtering for 10 minutes at a) 200 °C b) 120 °C. Both samples of ZnO base film were used for the growth of ZnO NRs by wet chemistry, from starting equimolar (0.01M) aqueous solutions of Zn^{2+} and HMT at 95 °C and 1.5 hours of reaction time.

Table 6 Average crystallite size of ZnO NRs/ ZnO base film/ITO film deposited at different temperatures by magnetron sputtering.

Substrate	(002) Peak	FWHM ($^{\circ}$)	D
	Position		Average crystallite size (nm)
Deposition temperature	(2θ)		
ZnO NRs/ITO (200°C)	34.90	0.32	25.6 ± 0.2
ZnO NRs/ ITO (120°C)	34.54	0.34	24.06 ± 0.01

B. Field Emission SEM Analyses

Figure 30 shows that the highly oriented ZnO NRs with an average diameter of 78.49 nm (SD 21.39) and uniform lengths around 2.5 μ m in length were perpendicularly grown to the substrate. In addition, it was found that by controlling the experimental conditions, such as the deposition temperature, were obtained highly arrayed ZnO NRs. The effects of the deposition temperature on ZnO base film indicate a relatively high dependency on coverage over the entire substrate surface and closely packed seed layer provides an excellent

performance of highly oriented ZnO NRs. However, as the temperature is decreased the length of the rods decreases as seen Figure 30b. This compares with the seed crystal diameter of 95.46 nm (SD 30.02) as seen in Figure 30b.

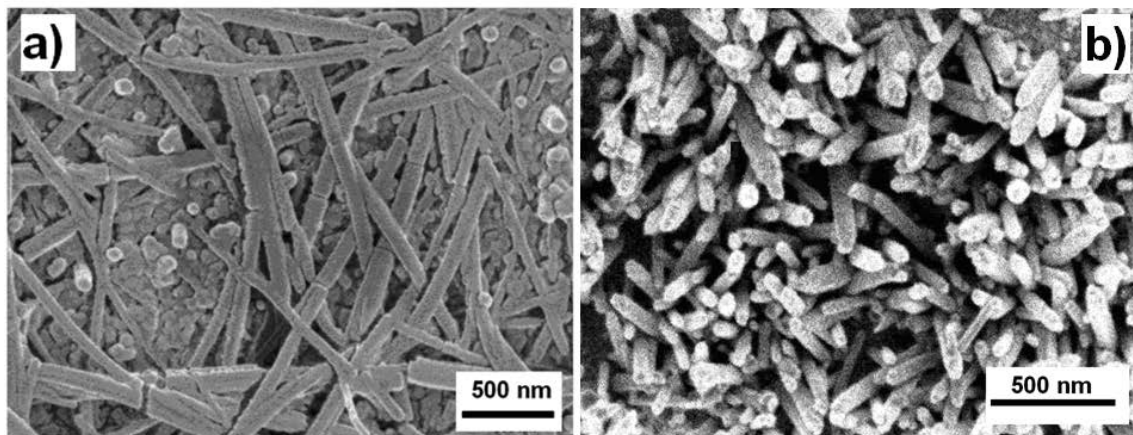


Figure 30. FE-SEM images of the ZnO NRs used on ZnO base film/ITO film deposited by RF magnetron sputtering for 10 minutes a) 200 °C (b) 120 °C. Both samples of ZnO base film were used for the growth of ZnO NRs by wet chemistry, from starting equimolar (0.01M) aqueous solutions of Zn^{2+} and HMT at 95 °C and 1.5 hours of reaction time. The estimated diameter for the the ZnO NR/ZnO base film/ITO were 95.46 nm (SD 30.02) and a length of 1.5 μm (396.87 nm) for 200 °C. Diameter size was 78.49 nm (SD 21.40 nm) with a length of (419.5) (SD 103.5 nm) for 120 °C.

5.10 Effect of deposition time on ZnO base film/ ITO by sputtering on the growth of ZnO NRs

ZnO nanorods grown on ZnO base film/ITO glass substrates show random distribution, with excellent substrate coverage as seen in Figure 31a. These nanorods have random orientation superior than that for film deposited by RF magnetron sputtering at 10 minutes. In addition, it is observed that it does not exhibit a preferential growth angle for the NRs obtained. Nanorods grown at 120 °C for 10 min had a grain size of 203 nm (SD 0058). Interestingly, ITO-coated glass has a comparatively rougher surface than the other substrate. It is hypothesized that this roughness may be a contributing factor in the disordered orientation of the nanorods.

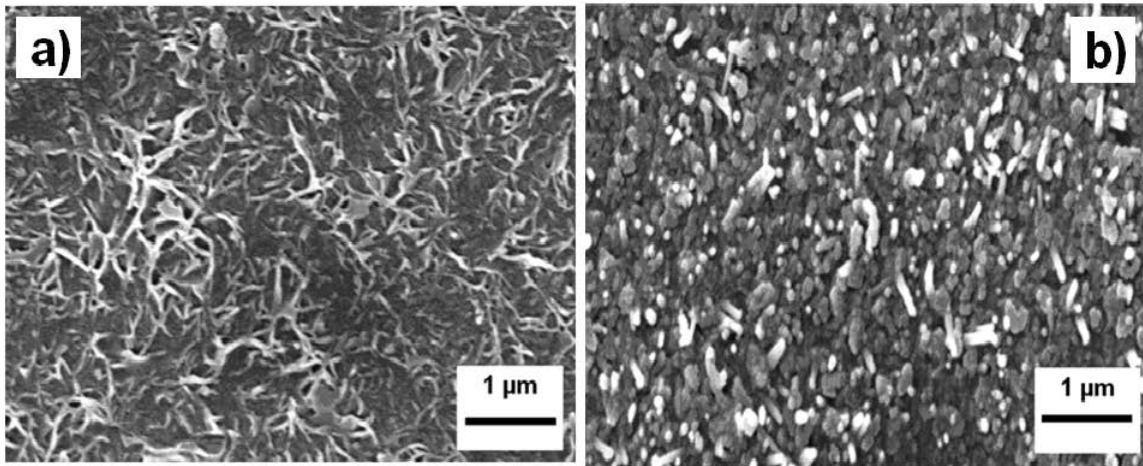


Figure 31. FE-SEM arrays of ZnO NRs deposited onto ZnO base film/ITO film deposited by RF magnetron sputtering at 120 °C for a) 30 min and b) 10 min. Both samples of ZnO base film were used for the growth of ZnO NRs by wet chemistry, from starting equimolar (0.01M) aqueous solutions of Zn^{2+} and HMT at 95 °C and 1.5 hours of reaction time. Diameter size for the the ZnONR/ ZnO base film/ITO were 19.65 nm (SD 0.058) and a length of 529 nm (SD 153 nm) for 10 min.

5.11. ZnO rods deposited onto ZnO base film/Si (100)

5.11.1 Effect of temperature treatment of ZnO base film/Si(100) on the growth of ZnO NRs.

A. XRD Analyses

Figure 32 shows the XRD for ZnO NRs/ ZnO base film/Si (100) and it is evident the effect of temperature on the material obtained. The (002) preferential plane shows a small shift of approximately $2\theta = 34.24$ nm with an average crystallite size of 14 nm for a deposition temperature of 200 °C as shown in Figure 32a. While at the lower deposition temperature by magnetron sputtering, the (002) plane was slightly increase in shift ($2\theta = 34.58$ nm) as seen in Figure 32b. Furthermore, the preferential growth of the (002) plane and the absence of other planes such as the (101) plane in the ZnO deposit, confirmed the strong out-of-plane orientation for ZnO NRs/ZnO/Si (100). This could be an indicative of the development of columnar crystals. ZnO NRs/ Si (100) obtained at a lower temperature were found to have an average crystallite size of about 2.5 nm as shown in Table 5. This suggests that the reaction time had a more profound effect on the average crystallite size of ZnO NRs obtained.

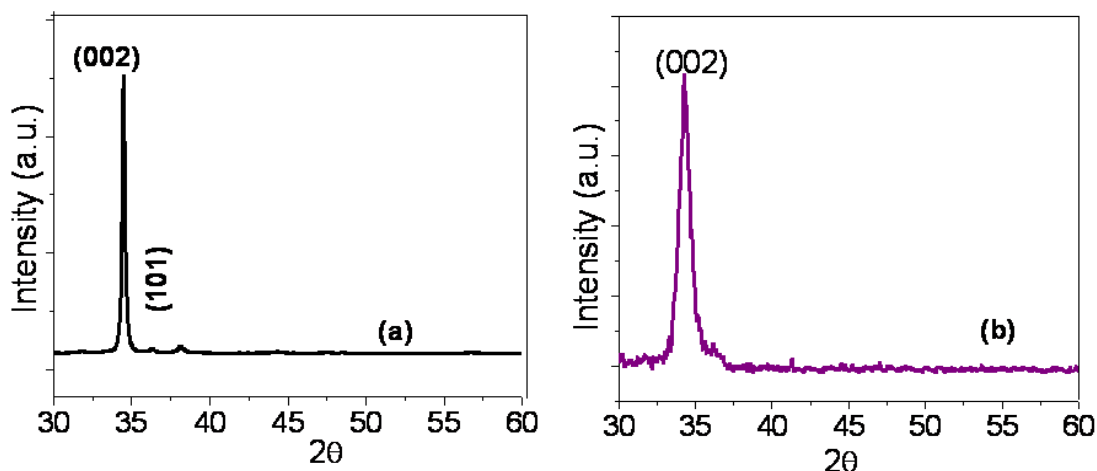


Figure 32. XRD patterns for ZnO NRs/ ZnO base films used on ZnO base film/Si (100) substrate deposited by RF magnetron sputtering for 10 minutes at (a) 200 °C (b) 120 °C. Both samples of ZnO base film were used for the growth of ZnO NRs by wet chemistry, from starting equimolar (0.01M) aqueous solutions of Zn²⁺ and HMT at 95 °C and 1.5 hours of reaction time.

Table 7. Average crystallite size of ZnO NRs/ ZnO base/ Si (100) film deposited at different temperatures by magnetron sputtering

Substrate Deposition temperature	(002)Peak	FWHM (°)	D crystallite size (nm)
	Position (2θ)		
ZnO NRs/Si (200°C)	34.24	0.6	13.63± 0.09
ZnO NRs/ Si (120°C)	34.58	3.3	2.45± 0.00

B. Field Emission SEM Analyses

The FE-SEM image shown in Fig. 33a corresponds to ZnO nanorods grown on ZnO base film/Si (100) at 200 °C. Substrates were deposited by RF magnetron sputtering for 10 minutes. These showed a superior proximal distribution, with excellent substrate coverage. These ZnO NRs have thickness of around 150 nm and diameters of 124.73 nm (SD 31.78).and a length of 263.6 nm (SD 7305 nm) Therefore, ZnO NRS made with ZnO base film deposited by RF magnetron sputtering for 10 minutes at 120 °C displayed a thicker diameter for ZnO NRs arranged in rodlike structures as seen in Figure 33b. Resulted in ZnO NRs with thickness of around 48 nm and diameter of 50.14 (SD 16.37) and a length of

319.36 nm (SD 9.052). It has been reported that ZnO nanowires in close proximity are inclined to have coalescence effects, and multiple ZnO nanowires forming one single growth site may merge together to form a thicker nanorod under appropriate conditions [23]

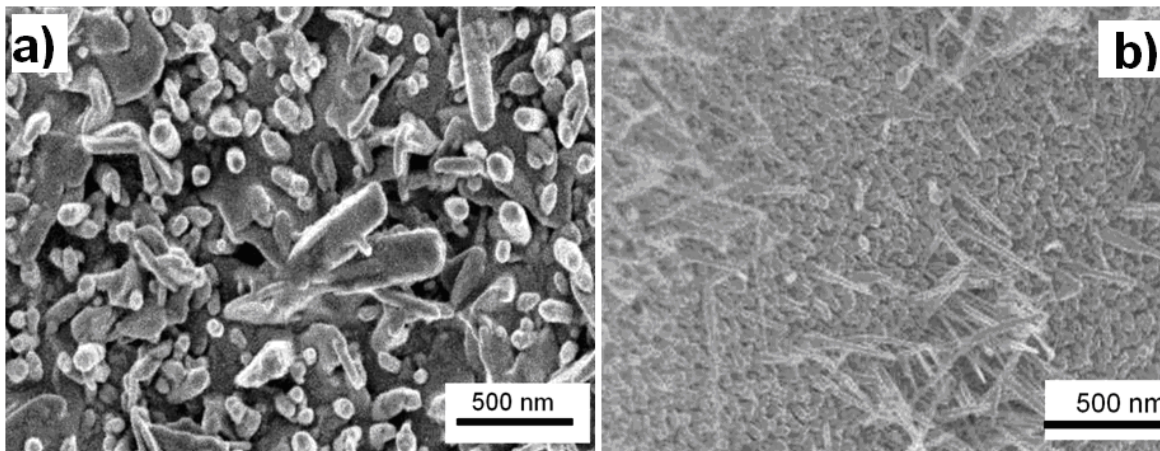


Figure 33. ZnO NRs/ ZnO base films used on ZnO base film/Si (100) substrate deposited by RF magnetron sputtering for 10 minutes at a) 200 °C b) 120 °C. Both samples of ZnO base film were used for the growth of ZnO NRs by wet chemistry, from starting equimolar (0.01M) aqueous solutions of Zn^{2+} and HMT at 95 °C and 1.5 hours of reaction time. ZnO NRs obtained at 200 °C had thickness of around 150 nm and diameters of 124.73 nm (SD 31/78). Use of a temperature of 120 °C resulted in ZnO NRs with thickness of around 48 nm and diameters of 50.14 nm, (SD 16.37), length of 319.36 nm (SD 90.52 nm).

5.12 Optimum conditions for growth of ZnO rods.

Based on the experiments conducted previously, it has been determined that the optimum conditions for deposition of ZnO base film by magnetron sputtering are: deposition temperature of 120 °C at 10 min with a constant power of 150 W and pressure of Ar for ZnO base film. For ZnO NRs synthesis, a constant 1:1 molar concentration of HMT to $Zn(NO_3)_2$ at 95 °C for 1.5 hr of reaction time via the wet chemistry procedure were deemed the optimal conditions.

5.13 Structural characterization of ZnO rods deposited onto ZnO base film /ITO substrates

5.13.1 XRD Analyses

The X-ray diffraction patterns corresponding to the ZnO/ITO substrates and the ZnO deposited onto this base are shown on Figures 34a and 34b, respectively. In both samples, the diffraction patterns clearly show the preferential growth along the (002) plane in the wurtzite structure of ZnO. However, some ZnO NRs did not grow in the c vertical axis due to the weaker appearance of the (101) and (102) planes. This suggest the formation of a well organized columnar structures along the c-axis direction perpendicular to the substrate. The peak at a 35.4° corresponds to the ITO substrate.

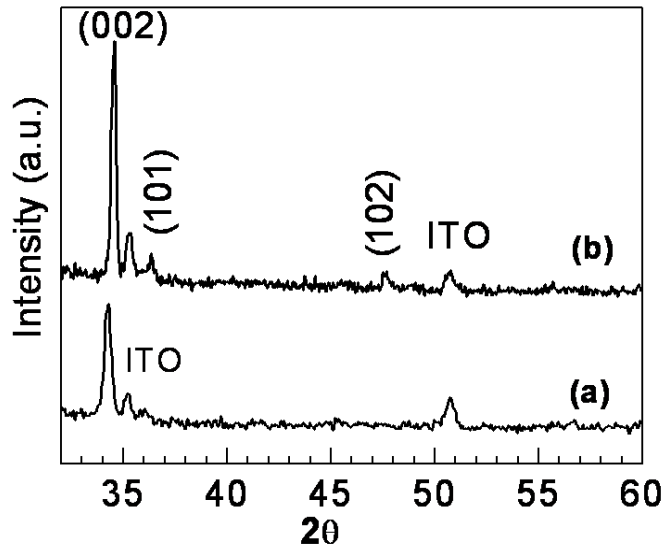


Figure 34. XRD patterns for: (a) ZnO base films deposited by sputtering on 15-25 $\Omega/\text{SQ}2$ ITO substrates at 120 °C, and 10 min of deposition time; (b) ZnO rod deposited from starting equimolar (0.01M) aqueous solutions of Zn^{2+} and HMT at 95 °C after 1.5 hours of reaction time.

The broadening of the XRD peaks evidenced the nanocrystalline nature of the ZnO NRs grown. The average crystallite size, estimated by the Scherrer's equation was about 26 nm. Although both XRD patterns evidenced the preferential growth in the c-axis direction by development of the (002) peak, it was shifted toward lower diffraction angles in the pattern with respect to the standard value at $2\theta = 34.422^\circ$ (ICDD Powder Diffraction File # 36-1451), as shown in Table 6 and in Fig. 34a corresponding to the ZnO base film. This shift can be attributed to compressive stress in the ZnO film deposited by sputtering onto the ITO substrate. The diffraction peaks can be indexed to a wurtzite hexagonal structure of the bulk

ZnO crystal with lattice constants $a = 0.32$ nm and $c = 0.51$ nm from the orientation plane (002) [165]. These values were obtained from Bragg's law and the corresponding plane spacing equation reported elsewhere for a hexagonal packing [154].

Table 8 Average crystallite size of ZnO thin films deposited on different substrates.

Substrate	(002)Peak	FWHM ($^{\circ}$)	D
	Position (2θ)		(crystallite diameter nm)
ZnO/ITO	34.23	0.43	19.0 ± 0.1
ZnO NRs/ ZnO/ITO	34.52	0.32	25.57 ± 0.02

Table 8 is a summary of XRD results and estimated crystallite size for ZnO thin films on the ITO glass and Si substrates, and ZnO NRs on ZnO/ITO, It is to be noted that the strain is compressive between ZnO and ITO.

5.13.2 UV-VIS absorption

Figure 35 shows the UV-VIS optical absorption spectrum for the ZnO rods grown on the ZnO/ITO substrate. The excitonic absorption peak is clearly observed at about 364 nm, which exhibits a blue shift compared to bulk ZnO materials (388 nm) [24]. This blue shift observed may be attributed to a confinement of the ZnO rods to nanoscale dimensions [25]. In contrast, optical absorption analysis was not possible for the Si substrate due to the lack of transparency for the ZnO NR deposited on ZnO/Si (100) substrate in the UV-VIS spectral range of interest.

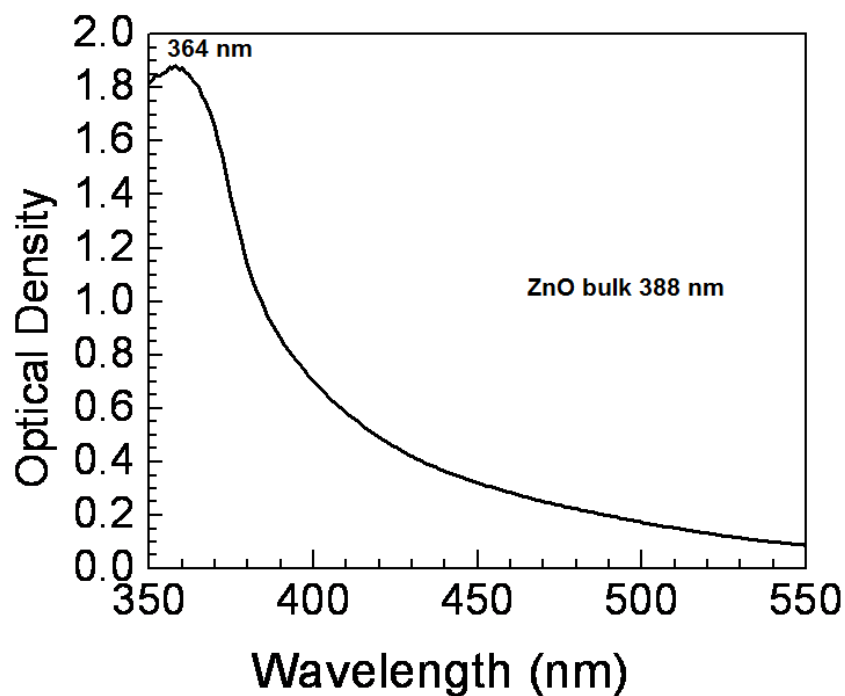


Figure 35. UV-VIS spectrum of ZnO rods deposited onto ZnO/ITO base film. The ZnO rods were grown using equimolar (0.01 M) aqueous solutions of Zn^{2+} and HMT at 95 °C and 1.5 hours.

5.13.3 PL measurements

ZnO rods deposited onto ZnO/ITO base film. ZnO rods were formed by the reaction of the following equimolar (0.01 M) aqueous solutions of Zn^{2+} and HMT at 95 °C and 1.5 hours. The photoluminescence spectra of ZnO NRs deposited onto ZnO/ITO base films substrates are shown in Figure 36. The spectrum was recorded at room temperature and under an excitation wavelength of 350 nm. The spectrum clearly displays the dominant (NBE) at 380 nm and also with weaker relative intensity a broad green luminescence (GL) at 550 nm emission bands previously reported in characteristic ZnO structure thin films [167]. Even though the origin of the GL band has been a matter of discussion [167-169] it is typically associated with deep-level defects such as oxygen vacancies and interstitial Zn ions, which is largely dependent on the synthetic route used for preparation of the ZnO NRs.

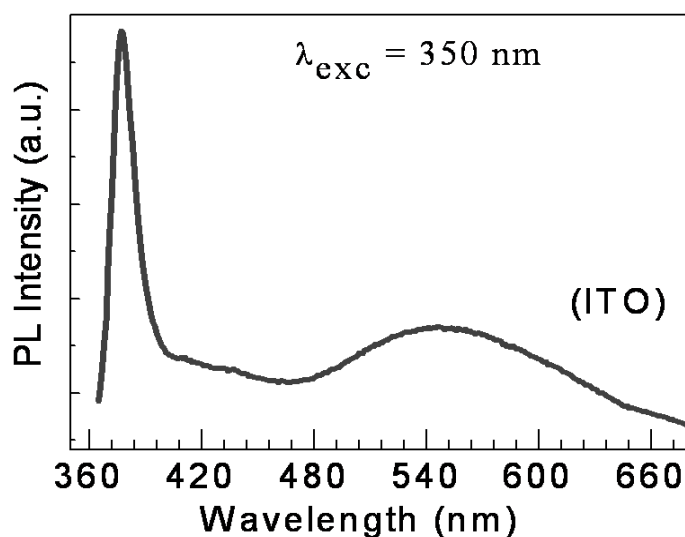


Figure 36. PL spectrum for ZnO rods obtained at an excitation wavelength of 350 nm.

5.14 Structure and Characterization of ZnO NRs deposited onto ZnO/Si (100) substrates under optimized conditions.

5.14.1 XRD Analyses

Fig. 37 shows the diffraction patterns of ZnO/Si (100) base film substrates (37a) and the corresponding ZnO rods deposit (37b). In this case, the base film was produced after a sputtering time of 10 min. The peak broadening observed in the XRD pattern of ZnO base film suggests an extremely and comparatively smaller crystallite size, with respect to those presented in Section 5.5.1. The estimated average crystallite size using Scherrer's formula was 9 nm, which is larger than the 4 nm estimated for the ZnO base film deposited onto ITO substrates. This is mainly due to different types of ZnO stress on those substrates such as compressive and tensile stress. Also in this case, the exclusive presence of the (002) diffraction peak evidences the preferential growth of the (002) planes in both the ZnO base film and the ZnO deposit. Furthermore, the preferential growth of the (002) plane and the absence of other planes different from those corresponding to (001) in the ZnO deposit, confirm the strong out-of-plane orientation for ZnO NRs/ZnO/Si. This could be an indicative of the development of columnar crystals oriented along the c axis.

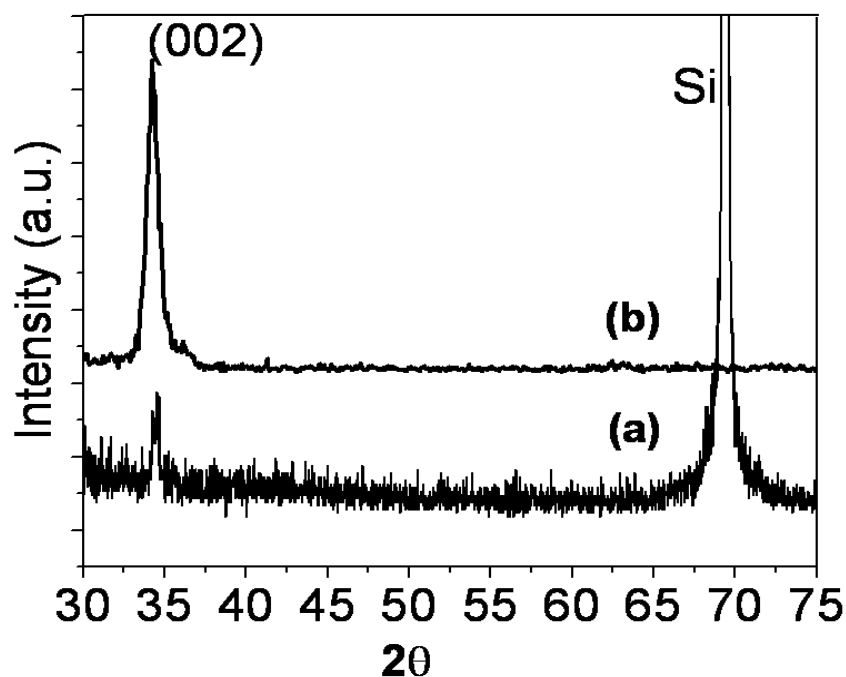


Figure 37. XRD patterns for: (a) ZnO/ Si (100) base film deposited by sputtering at 120 °C and 12 min of deposition time; (b) ZnO rods deposited onto the ZnO/Si base film. The ZnO rods were formed from equimolar (0.01 M) aqueous solutions of zinc nitrate and HMT at 95 °C and 1.5 hours of reaction time.

The above described ZnO/Si (100) film was placed in contact with an equimolar aqueous solution of 0.01 M zinc nitrate and HMT at 95 °C for 24 hours. At the end of the reaction period, the deposited material was annealed at 200 °C during 10 minutes in order to remove any traces of organic contaminants. The XRD pattern of the ZnO rods deposited onto ZnO/Si seed, Figure 37b, evidenced the preferential growth of the (002) plane over the (101) plane, which suggests the development of columnar crystals. It is believed that in the aqueous processing state, hexamine being a non-polar chelating agent would prefer being attached to the non-polar faces of the ZnO crystallites, thereby exposing only the (002) plane for epitaxial growth [157]. SEM analyses were used to confirm this interpretation.

Table 9 Average crystallite size of ZnO thin films deposited on different substrates.

Substrate	(002) Peak Position (2θ)	FWHM ($^{\circ}$)	D (crystallite diameter nm)
ZnO/Si (100)	34.42	0.45	18.18 \pm 0.05
ZnO NRs/ ZnO/Si (100)	34.24	0.89	9.19 \pm 0.06

Table 9 is a summary of XRD results and estimated crystallite size for ZnO thin films on the Si (100) substrates, and ZnO NRs on ZnO/Si(100).

5.14.2 UV-VIS absorption

UV analysis was not conducted because ZnO NRs/ ZnO base film /Si (100) substrates are transparent to UV radiation. Furthermore, PL spectra on ZnO base films / Si (100) and ITO film were not realized because of poor signal strength.

5.14.3 PL measurements

Shown in Fig. 38 are the PL results obtained for ZnO rods grown on the ZnO base film/Si (100) substrates. The spectra were recorded under an excitation wavelength of 350 nm, which lies within the absorption profile of the nanostructures. A weak shoulder near 381 nm was observed and was attributed to donor acceptor pair levels in ZnO base on p-type Si (100) substrate [169]. A small blue shift was observed on ZnO NRs/ZnO/Si with respect to ZnO NRs/ZnO/ITO. Both figures (38a and 38b) clearly display the dominant narrow NBE and also with lower relative intensity broad GL emission bands characteristic of ZnO rods [168, 170], at 380 nm and 550 nm, respectively. As observed, the qualitative features of the ZnO NRs spectra are similar for both surfaces, regardless of the nature of the substrate, mainly due to the use of ZnO base thin films on those substrates. Moreover, the relative PL area ratios of the UV NBE emission to the GL band (I_{UV}/I_{vis}) are 0.3 for the ZnO base film/ITO and 0.4 for ZnO base film/Si (100) substrates, respectively. Thus, the similar I_{UV}/I_{vis} ratios observed herein are indicative of the reliability of the preparation procedure for

yielding ZnO NRs in a consistent manner for both the ITO and Si (100) substrates. Regarding the ZnO/Si (100) and ITO base films, significant emission could not be recorded, due to the lack of nanostructure on base thin films.

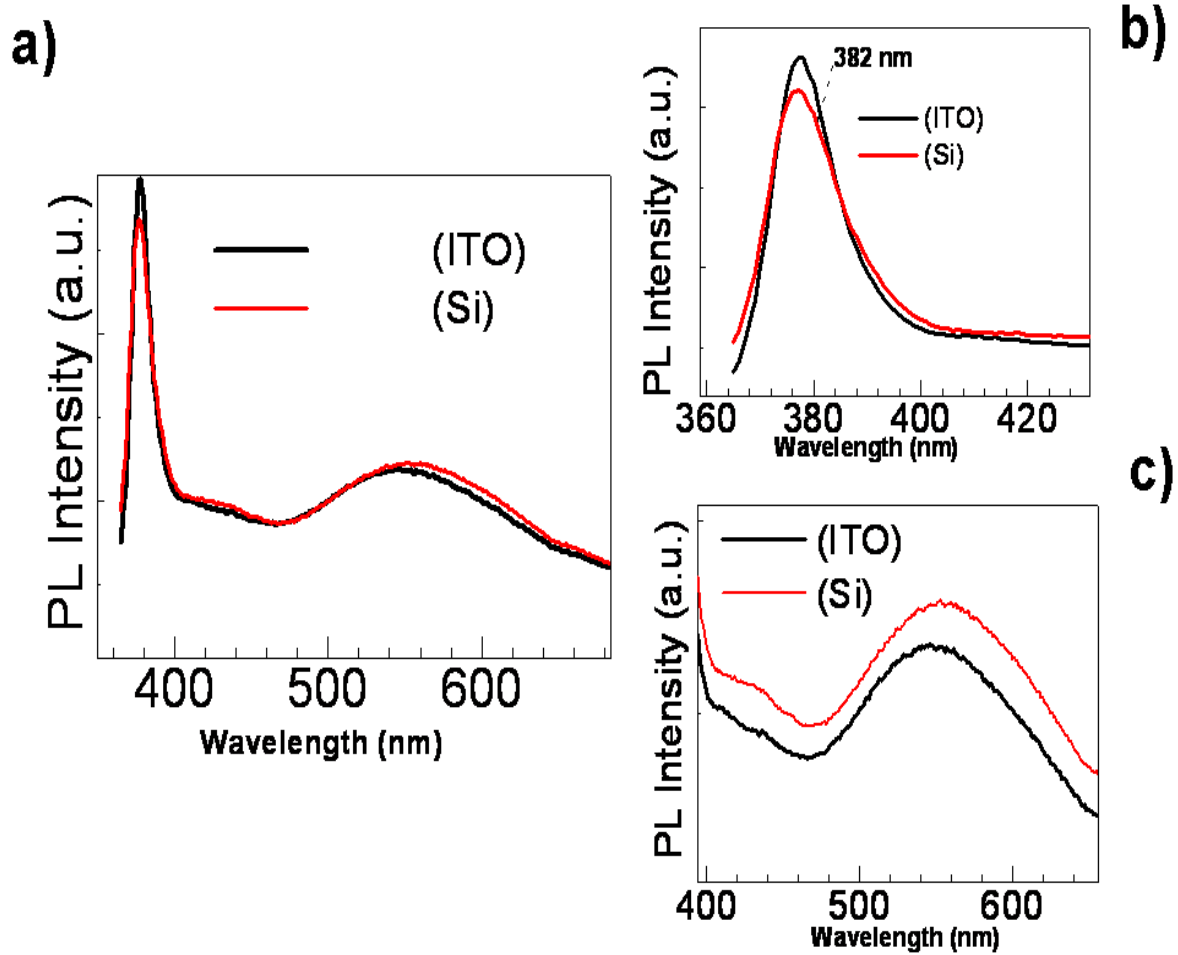


Figure 38. PL spectra for ZnO rods obtained at an excitation wavelength of 350 nm. a) ZnO rods deposited onto ZnO/Si and ZnO/ITO base film. In both cases ZnO rods were formed by the reaction of the following equimolar (0.01 M) aqueous solutions of Zn^{2+} and HMT at 95 °C and 1.5 hours. b) Comparison of UV NBE emission band for ZnO rods deposited onto ZnO/Si and ZnO/ITO base film. A weak shoulder is discernible at 382 nm. c) GL band for ZnO rods deposited onto ZnO/Si and ZnO/ITO base film.

5.15 Comparative morphological analyses for ZnO-NRs deposited on ZnO/Si (100) and ZnO/ITO

In order to attain additional insights on the morphological features of our samples, prepared base films and ZnO deposits were analyzed by field-emission scanning electron microscopy.

FE-SEM images shown in Fig. 39 correspond to the ZnO/Si (100) base films grown by RF magnetron sputtering. The films appear highly compact, which suggest a good quality deposition. The grains look equiaxial. These grains are considered as seeds for the growth of the corresponding rods.

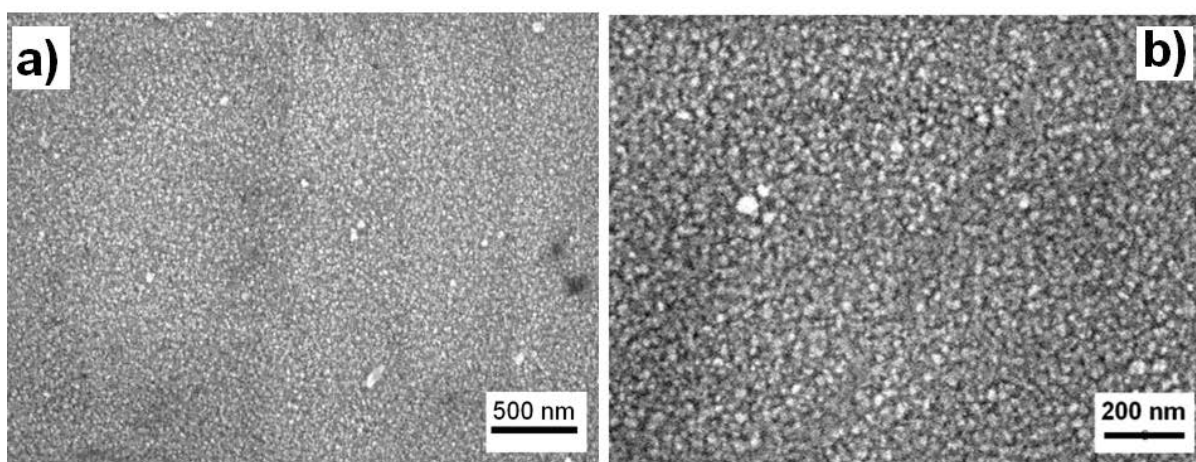


Figure 39. (a) FE-SEM images of the ZnO base film/Si (100) film deposited by RF magnetron sputtering for 10 min at 120°C. ZnO NRs obtained had thickness of around 20 nm and diameters of 19.85 nm (SD 4.85). (b) Magnification of (a).

The FE-SEM images shown in Fig. 40 correspond to the ZnO/ITO base film. As with the Si (100) substrate, the films also seem uniform and compact again suggesting good sputtering deposition quality. When comparing Figs. 39 and 40, the morphological features in both types of ZnO base films are evident. While ZnO grains were more or less equiaxial when ZnO was deposited on Si (100), they exhibited elongated shape when ITO was used as substrate. The crystal growth on the Si (100) substrate is a function of the particular orientation of the Si atoms on a specific plane. The size of the structures varies by orders of magnitude, from nonporous silicon to mesoporous Si, with crystallites in the nanometer scale. The diverse morphological features of porous Si can be affected by pore orientation, filling of macropores and depth variation of porous Si. [171]. However, ITO substrates do not have an orientation specific plane and they typically have low roughness upon manufacture. These structural differences affect the morphology of ZnO base film deposited by RF magnetron sputter on Si (100) and ITO substrates.

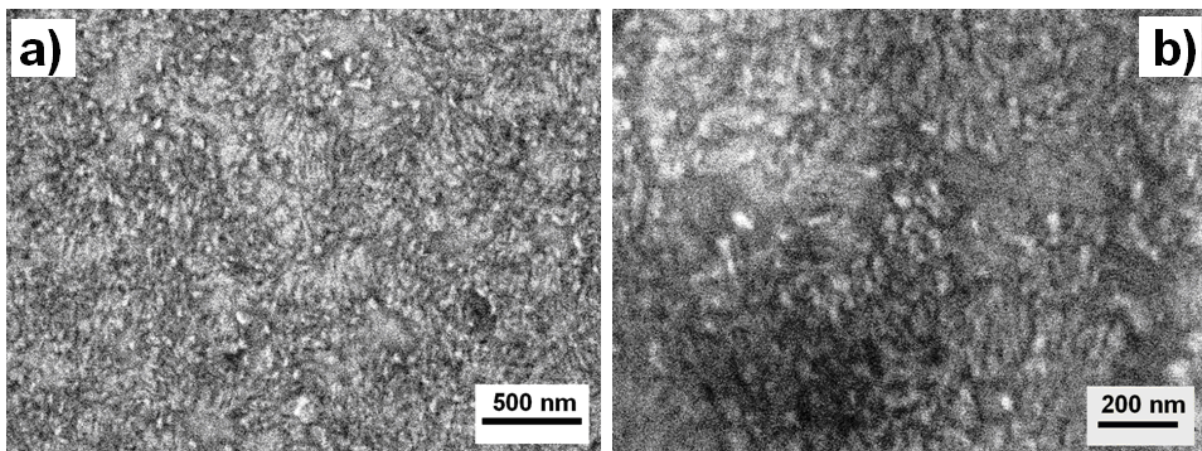


Figure 40. (a) FE-SEM images of the ZnO base film/ITO film deposited by RF magnetron sputtering for 10 min at 120°C. ZnO NRs obtained had diameter of around 64.77 nm (SD 23.71). (b) Magnification of (a).

Fig. 41 shows the FE-SEM images of the ZnO deposited on ZnO/Si, (a-b) and ZnO/ITO (c-d) base films deposited by RF magnetron sputtering for 10 min at 120°C from variation of the HMT and $\text{Zn}(\text{NO}_3)_2$ mol relation 1:1 at 0.01 M. The rod-shaped particles are clearly noted. Rods deposited onto ZnO/Si (100) base films averaged 50 nm in thickness with lengths above 1.2 μm . (SD179.4 nm). The ZnO rods grown onto ZnO/ITO base films were also nanometric in thickness (~ 78.49 nm) although shorter (up to 419.5 nm in length) compared to the rods grown on ZnO/Si (100) base films. The diameter for these rods was 64.77 nm (SD 8.52). These small differences in morphology of the ZnO NRs can be attributed to the observed differences on the morphology (grain size and shape) of the base films [152].

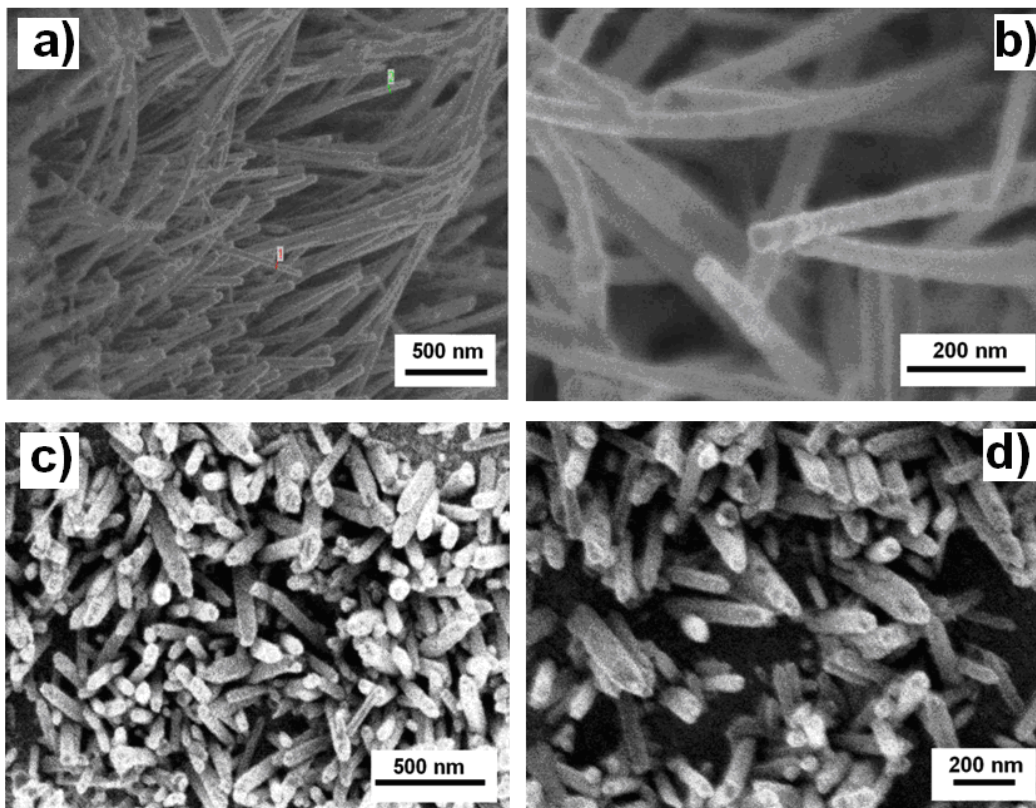


Figure 41. FE-SEM images of ZnO nanorods deposited onto a) ZnO/ Si (100) b) Magnification of a) c) ZnO/ ITO d) Magnification of c). Variation of the HMT and $\text{Zn}(\text{NO}_3)_2$ mol relation 1:1 at 0.01 M. ZnO NRs deposited onto ZnO base film/ Si (100) had obtained had diameter of around 64.77 nm (SD 23.71). ZnO NRs deposited onto ZnO base film/ITO had diameter size of around 78.49 nm (SD 21.40 nm) with a length of (419.5) (SD 103.5 nm) for 120 °C.

The appropriate manipulation of the synthesis conditions in the wet chemistry procedure allowed a certain degree of control on the resulting materials. Changes in parameters such as concentration of the reactants in the aqueous phase or reaction time had a significant effect on crystal growth rate and the final morphology of the obtained nanorods.

5.16 Variation of the molar concentration of HMT and $\text{Zn}(\text{NO}_3)_2$

The FE-SEM image in Figure 42a corresponds to ZnO NRs deposited on ZnO base film/Si (100) films grown by RF magnetron sputtering. The ZnO rods were formed by the reaction of the following equimolar aqueous solutions: 0.001 M of zinc nitrate and HMT at 95 °C for the same growth period of 4 hours at 95 °C. The diameter of as-synthesized ZnO nanorods averaged 70.69 nm (SD 12.38) and a length of 215.61 nm (SD40.75 nm). In

comparison, the rods grown on ZnO base film/ ITO exhibited a significant change in morphology and size: their average thickness was around 250 nm with ZnO NRs agglomeration. In contrast, at a concentration of 0.001 M of both hexamine and zinc nitrate, the resulting ZnO NRs were thicker (average thickness of 119.42 nm with SD 27.20) for the same growth period of 4 hours at 95 °C as seen in Figure 42 b.

Figures 42c show ZnO NRs/ ZnO base film/ Si (100) obtained when a concentration of 0.1 M of both HMT and $Zn(NO_3)_2$ was used with a reaction time of 4 h. This material exhibited a diameter around (104.11 nm with SD 15.27) and lengths of (235.05 nm with SD 58.37) were formed plate-like structures around 250 nm in length when compared to an equimolar aqueous solution: 0.001 M of zinc nitrate and HMT at 95 °C for the same growth period of 4 hours at 95°C. This result suggests that concentration of the precursors had a more profound effect on the growth rate of ZnO NRs as compared to the chemical bath temperature (95 °C).

Figure 42d shows ZnO NRs which were fabricated onto ZnO base films / ITO at a concentration of 0.01 M of both HMT and $Zn(NO_3)_2$. The material obtained showed enlargement as perpendicular arrays on the substrates. Nanorods grown on ZnO base film/ ITO glass had widths of approximate diameter of 95.46 nm (SD 30.02) and 250 nm in length, with minimal variation between nanorods. ZnO NRs grew about one to three times thinner, with respect to ZnO NRs prepared with concentrations of reactants at 0.1 M. We attribute some small differences in morphology for ZnO NRs to the specific characteristics of the substrate (Si and ITO) in aspects such as orientation of growth and nanorod thickness [31].

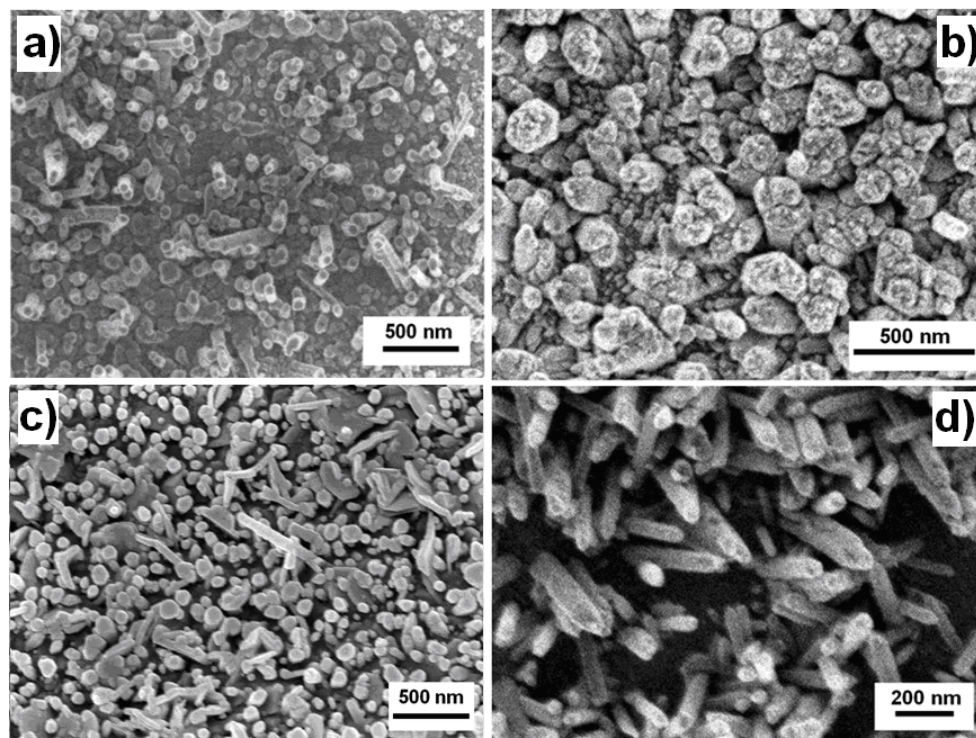


Figure 42. FE-SEM images for (a) ZnO NRs/ ZnO/Si, a reaction time of 4 hours and 0.001 M HMT and Zn^{2+} at 95 °C (b) ZnO rod/ ZnO/ITO, reaction time of 4 hours at 0.001 M HMT and Zn^{2+} at 95 °C. (c) ZnO NRs/ ZnO /Si films, at reaction time of 4 hours at 0.1 M HMT and Zn^{2+} at 95°C (diameter of 500 nm and 3 μ m lengths) (d) ZnO NRs/ ZnO /Si films, at reaction time of 1.5 hours at 0.01 M HMT (diameter of 75 nm and 500 nm lengths). The same reaction conditions were maintained for both substrates (Si and ITO) with a ratio 1:1 for Zn^{2+} and HMT, at a temperature of 95 °C.

Changes in the concentration of reagents employed resulted in changes in crystal size as well as a marked effect on the seed-layer thickness. This tendency is observed in Figures 42(a-b) and 42c. The diameter of the rods depended on the concentration of reagents and their length depended on the reaction time. However, when a two- or three-fold excess of Zn^{2+} was used, an increase in the specific surface area of NRs with respect to the substrate was observed as seen in Figures 42a and 42c.

5.17 Variation of reaction time on the growth of ZnO NRs.

The ZnO NRs were found to have thinner diameter (around 88 nm) lengths of at least 368 nm (SD 120.28) and formed plate-like structures. A concentration of 0.1 M solution of hexamine and zinc nitrate was used with a growth period of 4 hours at 95 °C (Figure 43a). In contrast, with a reaction time of 24 hours with the same concentration and temperature, the

ZnO NRs diameter was 113 nm with lengths of at least 2.51 μm (SD 0.99) as is shown in Figure 43b. This suggests that the reaction time had a more profound effect on the lengths of the grown ZnO NRs.

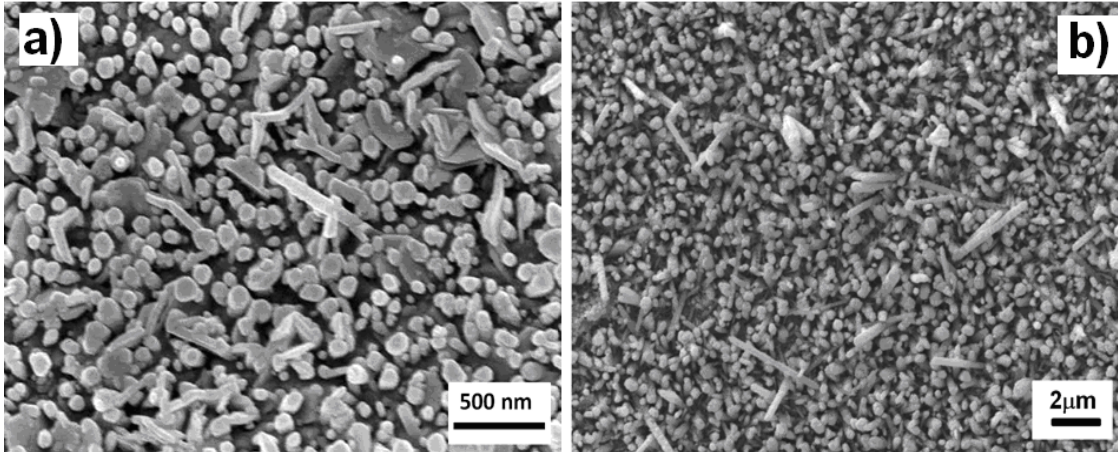


Figure 43 SEM image for ZnO rods collected from (a) a reaction time for 4 hours at 0.1 M HMT and Zn^{2+} at 95°C and (b) shows ZnO rods with a reaction time of 24 hours at 0.1 M HMT and Zn^{2+} at 95 °C.

FE-SEM images of Figure 44a correspond to ZnONRs deposited on ZnO base film/Si films grown by RF magnetron sputtering. The ZnO rods were formed by the reaction of the following equimolar aqueous solutions: 0.01 M of zinc nitrate and HMT at 95 °C and 1.5 hours. The diameter of as-synthesized ZnO nanorods averaged 560 nm and lengths above 3 μm as evidenced by the magnified section shown in Figure 44b. Uniform nanorods of ~60 nm were observed on ZnO base film/Si substrate with lengths depending on growth time consisting of 1.5 hours. In contrast, Figure 44c shows ZnO NRs which were fabricated onto ZnO base films / ITO showed enlargement as perpendicular arrays on the substrates. Nanorods grown on ZnO base film/ ITO glass have widths of approximately diameters of 75 nm and 500 nm lengths, with minimal variation between nanorods. For instance, it has been found that ITO has higher roughness than Si (100). We attribute some small differences in morphology for ZnO NRs to the specific characteristics of the substrate such as orientation and roughness.

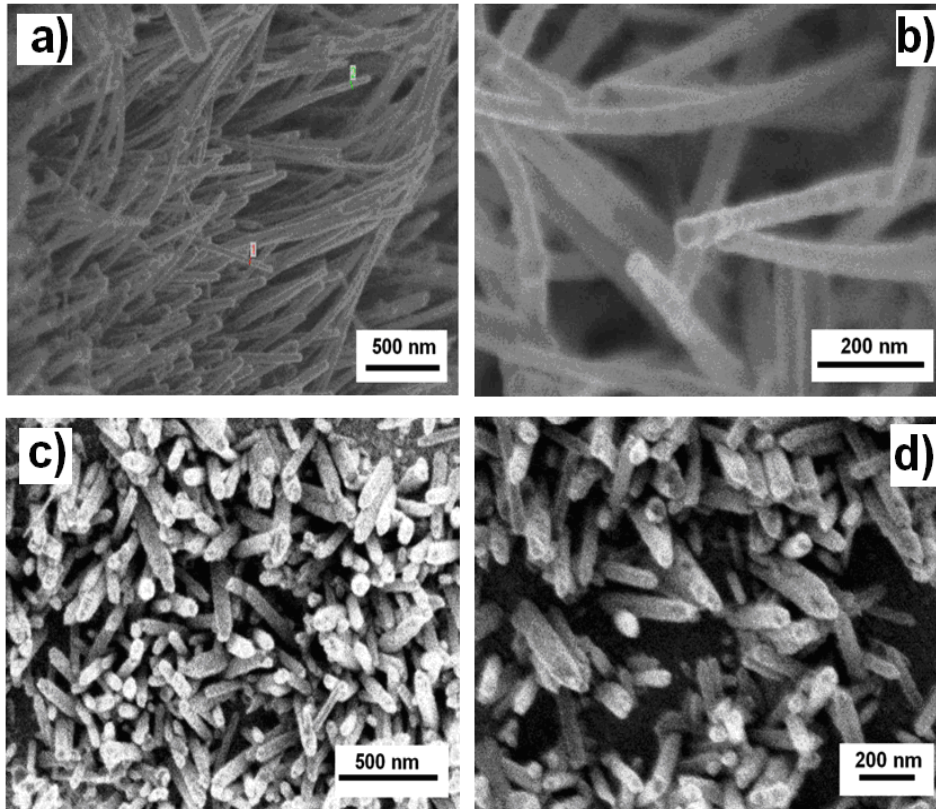


Figure 44 FE-SEM images of ZnO NRs on ZnO base film on Si (100) arrays with a diameter of: (a) 60 nm and lengths well exceeding 3 μm . (b) Approach Micrograph of ZnO NRs on ZnO base film/ Si(100). (c) ZnO rods/ ZnO base film/ Si (100) arrays. (d) ZnO NRs on ZnO base film on ITO film with a diameter of 75 nm and 500 nm lengths. The same reaction conditions were maintained for both substrates (Si and ITO) with a 1:1 ratio of 0.01M for Zn^{2+} and HMT, with a temperature of 95 $^{\circ}\text{C}$ and 1.5 hours of reaction time.

Variation of the experimental conditions, such as precursor concentration and reaction time during the wet chemistry method, allowed for a certain degree of control on the growth rate and the morphology of the obtained NRs. The role of hexamine in the growth of ZnO nanostructures consists of acting as a 7.2 pH buffer, by a slow release of OH^- ions by a hydrothermal process through thermal decomposition [172]. The best ratio for preparation of ZnO NRs was 1:1 for Zn^{2+} and HMT as observed in Figures 44a to 44d. It has been reported that, under hydrothermal conditions, HMT can promote the formation of well-aligned and highly crystallized ZnO nanorods [17]. Therefore, the concentration of precursor HMT had significant effects on the morphology of the materials obtained. During the heating process to 95 $^{\circ}\text{C}$, HMT will hydrolyze and release OH^- and the ionic product $\text{Zn}(\text{OH})_2$ with

subsequent dehydration to form the corresponding oxide. Regarding particle shape, the preferential adsorption of amine groups (from HMT) on specific crystallographic planes of ZnO has been reported. This promoted the preferential growth along the 'c' axis of the hexagonal wurtzite unit cell, which explains the rod-shaped morphology observed by FE-SEM analyses [165]. As discussed on Section 5.5.1 and 5.6.1, XRD patterns confirmed the preferential growth of ZnO NRs on the (002) plane (refer to Figures 34 and 37).

Compared to Vayssieres' method, our approach favors formation of NRs of thinner diameter (~60 nm) and shorter length (< 1.2 μm) [16]. It has been observed that NRs covered with a monolayer of gold of these dimensions could exhibit SERS performance with the possibility of molecule-level detection of different analytes [173].

5.18 Conclusions

ZnO NRs and rods were synthesized successfully by utilizing wet chemistry at a low temperature of 95 °C, based on modifications to Vayssieres method, namely the use of a reflux system at a constant temperature of 95 °C. The XRD characterization for ZnO rod showed a higher intensity for the (002) plane. The (002) plane usually corresponds to a maximum intensity of the ZnO zincite wurtzite structure, its seed size depended on many deposition parameters such as: temperature, radio frequency, deposition time and pressure. Both rod and nanorod size optimization depended on the ZnO base film size, and the parameters established by wet chemistry such as: molar concentration and reaction time. Temperature had a lesser effect in the growth of both ZnO nanorods and rods.

Analysis of the corresponding PL spectra evidenced the formation ZnO rods and ZnO NRs with the excitonic absorption peak clearly observed about 364 nm, which exhibits a blue shift compared to bulk ZnO materials (388 nm). Moreover, the relative PL intensity ratios of the UV NBE emission to the GL band (I_{UV}/I_{vis}) are 0.3 and 0.4 for the ZnO base film/ITO and ZnO base film/Si (100) substrates, respectively. This reflects a relatively higher oxygen vacancy concentration in the ZnO- NRs grown on ZnO/ITO in comparison with those on the ZnO/Si (100).

It was found that the morphology of ZnO NRs and rods depended from the type of substrate (Si or ITO) as well as concentration of reagents. Rods and nanorods were also confirmed by FE-SEM observations. The results indicated ZnO NRs were obtained with the following dimensions: between 60-500 nm diameter and lengths of 500 nm and 3 μm in ZnO NRs. It was possible to observe a greater change in the growth size of ZnO rods in comparison with the ZnO NRs, which had a smaller increase in diameter size. Longer reaction times allowed increase in the length of the rods. Interestingly, ZnO rods / nanorods on ZnO base film/ ITO have a comparatively surface than the other substrates. It is hypothesized that this may be a contributing factor in the disordered orientation of ZnO NR grown on ZnO base film/ITO glass substrates.

We found that annealing of the produced ZnO NRS at 200 °C allowed evaporation of organic residues. This results in the elimination of such impurities which would otherwise interfere with the detection of the analytes of interest. At 200 °C, the electrical conductivity of these semiconductors was not affected.

For future works, there exists the possibility of preparing scalable Au-nanocoated ZnO NRs arrays. These ZnO NRs offer distinct advantages over other techniques, since they can be applied to the fabrication of chemical sensors by Surface Enhanced Raman Spectroscopy (SERS). The nanorods are fully compatible with a wide variety of substrate types such as Silicon (100) and ITO.

5.19 ZnO Nanorods Coated with Au for Enhanced Raman Spectroscopy

5.19.1 Optimization of Synthesis of ZnO NRs coated with Au

Zinc oxide (ZnO) was first deposited using RF magnetron sputtering, and afterwards, a wet chemistry procedure was performed for ZnO NRs growth. Ion beam and UV process were used for coating the ZnO NRs with gold (Au). Au coating on ZnO NRs were used to evaluate the detection capability by SERS with different analytes. Au-coated ZnO NRs were characterized using X-ray diffraction, EDS and field emission scanning electron microscopy (FE-SEM). Ultraviolet photo-reduction showed a higher surface-enhanced Raman scattering than the ion beam method. This Au coating on ZnO NRs could successfully detect analytes such as: adenine, 4-nitrobenzenethiol and 2, 4-aminobenzethiol (ABT) and 1, 3, 5-trinitroperhydro-1, 3, 5-triazine (RDX) at low levels. Strong SERS spectrum of Raman was observed for 4-ABT. A limit of detection (LOD) of 1×10^{-8} M for ABT was achieved corresponding to a minimum of 5.4×10^5 molecules detected under the experimental conditions at excitation wavelength of 785 nm with a sensitivity of the ZnO NRs in the range of 1.1×10^{-16} g under laser spot.

5.19.2 Introduction

Zinc oxide studies conducted for several decades have shown the dependence of the physical properties of the materials obtained on the synthetic method for its preparation [3, 165, 174-176] Chemical-surface requirements of controlled size and shape and chemical roughening as a route to improving optical properties of the semiconductor nanostructures are also of high priority. The focal point of study in this research is the synthesis of ZnO NRs coated with gold metals, for the development of sensors using enhanced Raman spectroscopy phenomena.

Research in this field has gained considerable attention in different areas such as chemistry, biology, and material sciences and in building blocks for miniaturization of

electronics photonics devices and sensor for Surface Enhanced Raman Spectroscopy (SERS) [3, 177-178]. SERS technique offers a great enhancement of the intensity of the vibrational signals over 10 orders of magnitude, which has opened a new path for conventional Raman spectroscopy and made of SERS a powerful high-throughput spectroscopic technique for detecting very low concentrations of analytes from biomedical sciences [176-179] to environmental sciences [12-178]. It is widely accepted that chemical and electromagnetic enhancement are responsible for SERS enhancement [20, 180]. Recently, it has been demonstrated that using both three or two-dimensional (3D or 2D nanostructures) as SERS media can provide significant sensibility to bring SERS-based sensor to practical applications. It is desirable that the SERS substrates contain highly ordered structures with reproducible and controllable geometries, ranging from the conventional electron beam lithography [13, 140], photolithography [15], to the nanosphere lithography [16], block copolymer lithography [16, 17], [23].

Researchers have reported on utilizing luminescent semiconductor and samples of Au-coated ZnO NRs arrays with different average diameters. The diameter of the nanorods was controllable by the substrate position during the pulsed laser deposition. High SERS enhancement was observed from Au-coated ZnO nanorod arrays. The Raman spectra of rhodamine 6G (R6G) as low as 1 nM were measured with an average diameter of 400 nm [181].

Extensive studies have demonstrated that patterned binary monolayers can also be prepared on silver by inducing a surface-induced photoreaction for a self-assembled monolayer (SAM) of benzyl phenyl sulfide (BPS) on silver (Ag) [152]. On the other hand, it has been reported the use of strong or mild reducing agents to reduce different gold compounds aiming at better control of the size and size distribution in nanoparticles (NPs) [152-186] as also their physical and chemical properties.

The activation of ZnO NRs was usually carried out using either the ion beam method and the conventional optical methods using UV light lamp in short-wave based on photoreduction of gold (III) chloride hydrate (HAuCl_4) in solution.

In this research, a simple preparation method will be used to obtain Au-coated ZnO NRs in order to detect various analytes such as adenine, 4-nitrobenzenethiol and 2,4,6-trinitrotoluene, 4-aminobenzenethiol (ABT) and 1, 3, 5-trinitroperhydro-1, 3, 5-triazine (RDX) at low levels by SERS.

5.20 Experimental

5.20.1 Materials and Methods

All reagents used were of analytical grade. Zinc nitrate hexahydrate, $Zn(NO_3)_2 \cdot 6H_2O$ and hexamethylenetetramine (HMT), 4-nitrobenzenethiol, 99.99% , gold(III) chloride hydrate, (99.999% trace metals basis) were obtained from Sigma-Aldrich Chemical Co. The sputtering target used was zinc oxide, (all of 99.99% purity, 0.15” thick, 2” diameter) obtained from Superconductor Materials Inc. The p-type Si (100) and indium tin oxide (ITO) $15-25 \Omega/SQ^2$ substrates were purchased from Sigma Aldrich.

ZnO base films were grown using an ATC Orion 8-Linear E-Beam Magnetron Sputtering instrument was used with an on-axis configuration with two magnetron sputter guns for one mode sputtering process under radio frequency (RF) magnetron. ZnO NRs were prepared by wet chemistry method. Ion beam deposition was carried with Denton Vacuum, LLC, DSKV (DV-502B) a high-vacuum evaporator instrument with a high vacuum sample preparation system. A Renishaw Raman Microspectrometer RM2000 was employed for the vibrational spectroscopy measurements. The system is equipped with a Leica microscope. Sample detection was achieved at 785 nm wavelength. Experiments were performed at lab conditions (room temperature). The laser spot size on the focused samples was rectangular in shape, with dimensions: $50 \mu m \times 90 \mu m$. Laser power was kept on the sample head at 170 mW for 785 nm with the beam 100 % setting in the Wire Renishaw Software. The spectra were obtained in the range of 100-3500 wavenumbers (cm^{-1}) [5]. XRD experiments were carried out in a Siemens D5000 x-ray diffractometer (XRD) using the Cu-K α radiation (1.5405Å). The x-ray scans were performed between 2θ values of 20°

and 70°. SEM analyses were conducted on a JEOL-JSM 6500 instrument and a Philips/ FEI, XL30s, FEG SEM / Phoenix EDX.

5.20.2 Synthesis of Au coating on ZnO NRs.

The activation of ZnO NRs was usually carried out using the ion beam method and the conventional optical methods using UV light lamp. Deposited ZnO rods were activated by a precise coating with gold using ion beam sputtering technique. The coating conditions were 300 seconds of deposition, 17 mA and 50 mtorr of vacuum pressure for a sputter set point of 47%. According to the operation manual the gold coating thickness can be estimated at 32 nm, shown Figure 45.

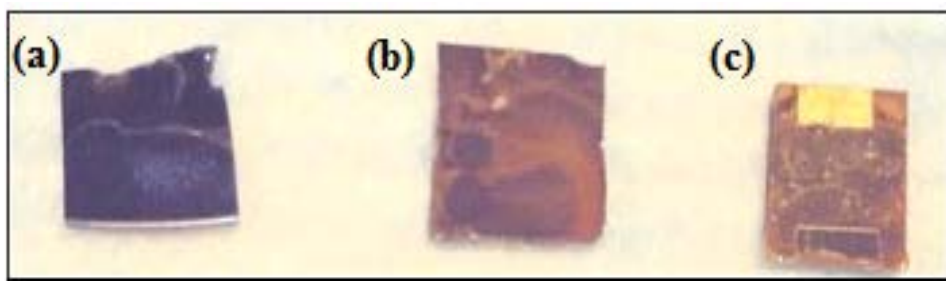


Figure 45. ZnO NR while light micrograph of: (a) ZnO NR/ZnO base film /Si (100), (b) Au-coated on ZnONR/ZnO base film/ Si(100) at 2 hours of UV–irradiation time. (c) Au-coated ZnO NRs/ZnO base film/Si by ion beam sputtering.

The second method used a UV light lamp. The experimental procedure was carried out using short-wave UV light based on the photoreduction of gold (III) chloride hydrate (HAuCl_4), from a 1×10^{-3} M solution with high purity water (MilliQ 18.2 M Ω cm). ZnO NRs films of 1 cm x 1 cm were swamped in a beaker with 4.0 mL of HAuCl_4 solution at pH 7.2, during 2 and 4 hours of reaction time under exposition of UV light. Afterwards, all films were rinsed with high purity water and dried at 120 °C for 2 hours to be used as substrates for SERS.

5.20.3 Normal Raman and SERS Experiments

Normal Raman and Surface Enhanced Raman Spectroscopy experiments were performed with a 785 nm excitation line in a Renishaw Raman Microspectrometer RM with spectroscopic grade CCD camera, 1200 l/mm (514/785) grating, Leica LX microscope and 10x objective, at 10 s integration time and 3 accumulations. For bulk analyte samples were prepared a solution of 0.1 M and poured in a capillary tube of 0.15 cm diameter. Spectra were recorded in the Raman Shift range of 100-3600 cm^{-1} at 3 accumulations, 10 s integration time each.

5.20.4 Sample Preparation for analysis by SERS

For SERS analysis, ZnO NRs were characterized using 4-ABT as SERS probe molecule. An aliquot of 2 μl of a solution 1×10^{-4} M to 1×10^{-8} M in ethanol were prepared and adjusted pH= 7.5 and mixed with 100 μL of 0.1 M sodium chloride (NaCl), sonicated for a period of 15 minutes followed by filtration through 0.5 μm mesh. The SERS spectra were recorded at the same conditions for: adenine, 4-nitrobenzenethiol and 2,4,6-trinitrotoluene, 4-aminobenzenethiol and 1, 3, 5-trinitroperhydro-1, 3, 5-triazine (RDX). The Raman signal for each mixture was recorded using 785 nm excitation wavelength in a Renishaw Raman Microspectrometer with a 10x magnification and 170 mW of power at head.

5.20.5 Results and discussion

Diffraction patterns for ZnO NRs/ZnO base film/ITO are shown in Figure 46. The three orientation planes (100) for ZnO and (111) and (200) for Au structures are observed. The plane (002) is absent suggesting deformation of columnar structures along the c-axis direction perpendicular to the substrate for ZnO NRs. Usually the (002) plane corresponds to a maximum intensity of ZnO zincite wurzite structure.

The broadening of the XRD peak evidenced the nanocrystalline nature of the ZnO deposit; the average crystallite size, estimated by the Scherrer's equation, was around 4.0 nm.

Au-coated on ZnO NRs/ZnO base film/ Si (100) shows a rise with respect to the (111) plane and signals also appear for the (200) and (220) planes characteristic to fcc Au phase [187, 188], as can be observed on Fig 47G. Reduction of the (002) planes with respect to (111), confirm the deposition of Au on ZnO NR. Wamng et al [189] have studied the electron transfer of the ZnO/Au system under UV light and concluded that the electrons transfer from Au to ZnO to form a uniform Fermi energy level during the formation of the Au-ZnO junction, as gold has a higher Fermi energy level than ZnO. Transferred electrons accumulate on the equilibrated Fermi level near the bottom of the conduction band of ZnO. More electrons can drop from the conducting band of ZnO to the valence band and recombine with holes, so more photons are radiated.

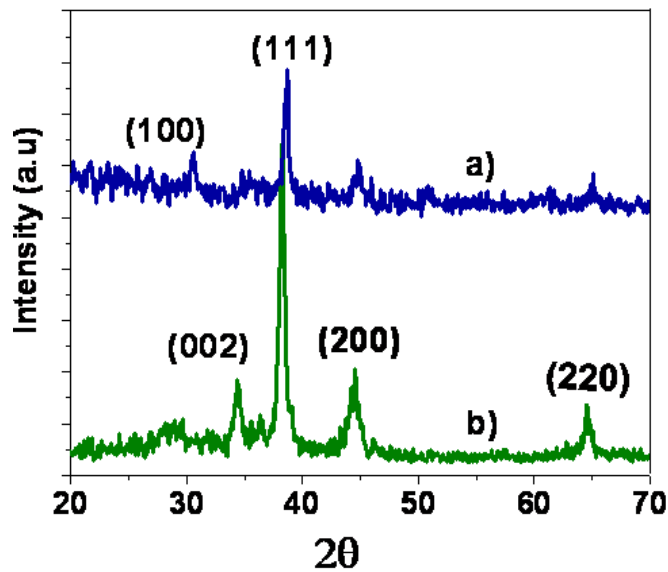


Figure 46. XRD a) Au-coated on ZnO NR/ZnO base film/ ITO and b) Au-coated on ZnO NR/ZnO base film/ Si(100). Au coating on ZnONR were formed by the reaction 1×10^{-3} M of HAuCl_4 aqueous solution kept at pH 7.2, with 2 hours of UV-irradiation reaction time at room temperature.

Based on the mechanism proposed by Yang et al. [190] for the photoreduction of Ag_2O , we can presume a similar path for Au^{+3} in HAuCl_4 as represented schematically in the diagram below [191].

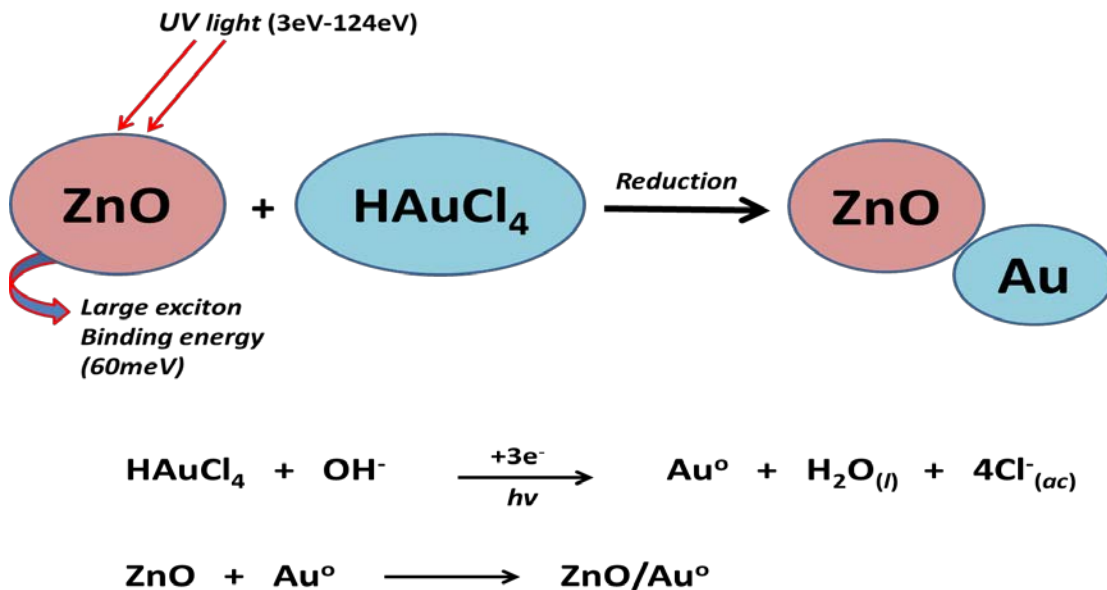


Figure 47a shows the energy-dispersive X-ray EDS spectra of the ZnONR/ZnO base film/Si. The absence of Au signal from this phases, suggests the high purity of ZnO deposits. and Fig 47b show Au coated/ZnO NRs/ ZnO base film/Si by ion beam sputtering method. The thickness of the film is approximately 32 nm. The energy-dispersive spectroscopy EDS images confirms the presence of zinc (Zn), oxygen (O) and gold (Au) atoms.

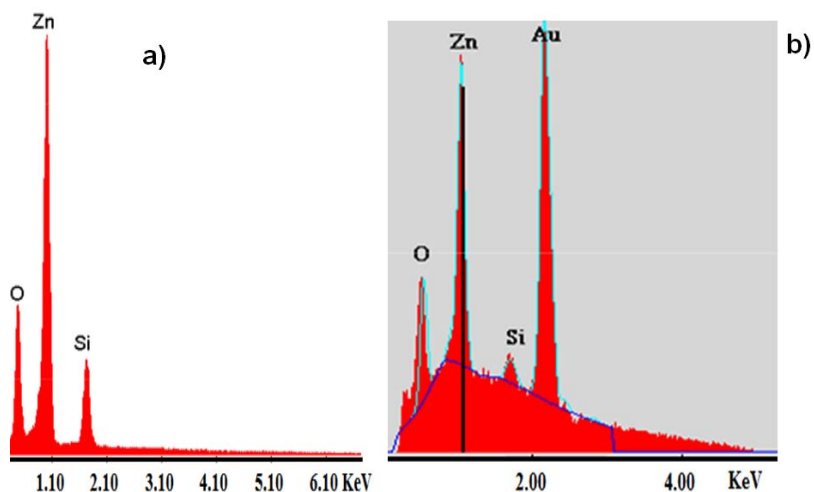


Figure 47. EDS Spectra from (a) ZnO NRs/ZnO basefilm/Si (100). (b) Au-coated ZnO NRs/ZnO base film/Si by ion beam sputtering.

Figure 48a show the SEM images for the Au coated on ZnO NRs/ ZnO/ Si (100), 1×10^{-3} M H_{AuCl₄} with 2 hours of UV-irradiation time. The deposition conditions for films and rods were the same as described in previous sections. As proposed, thicker rods were produced when the wet chemical synthesis took place onto the ZnO NRs/ZnO base/Si (100) film. In turn, thinner rods (average diameter of 48 nm with SD 10.21) and lengths of at least 421 nm (SD 86.81) were obtained when the deposition took place in the ZnO NRs resulting in reduction in diameter size. As discussed on Section 5.3 XRD patterns were of 4.0 nm from ZnO NRs/ ZnO/ Si (100). Figure 48b shows an approach micrograph of Au coated on ZnO NRs on ZnO base film/ Si (100).

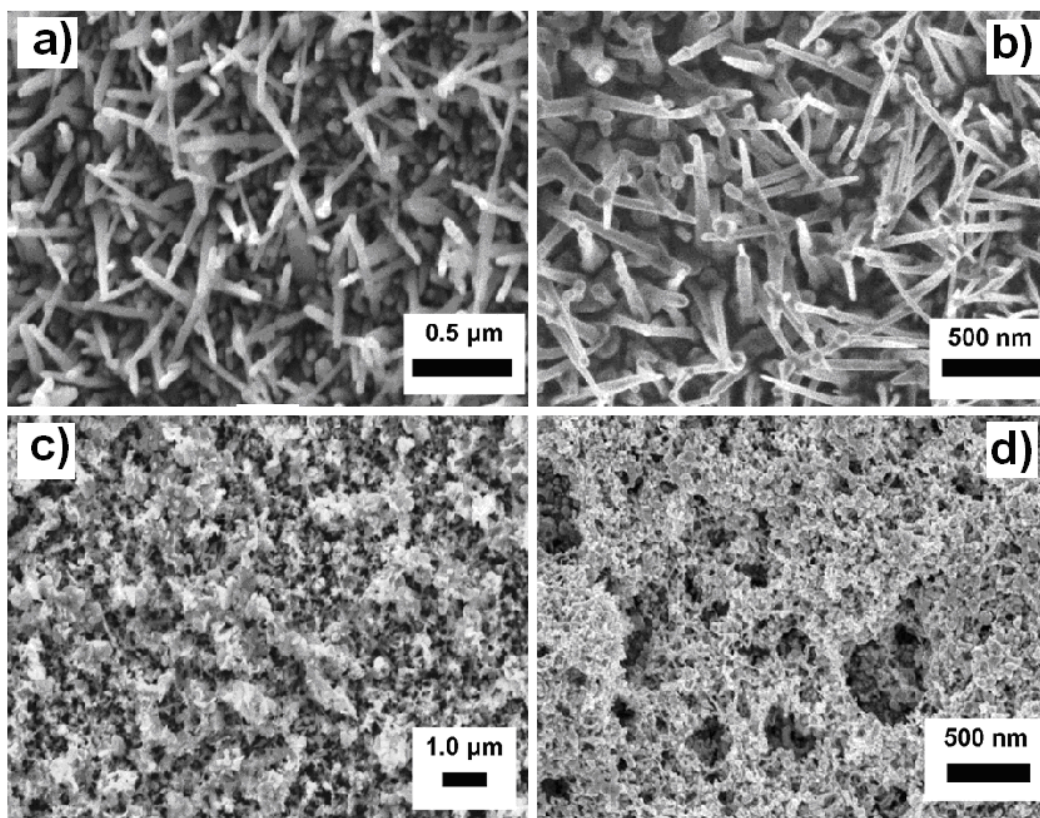


Figure 48. FE-SEM images of ZnO NRs/ZnO/Si morphology a) from Au coated on ZnO NRs/ ZnO/ Si (100), at 2 hours of UV-irradiation time. b) Zoom of a). c) Au coated on ZnO NRs/ ZnO/ Si (100), at 4 hours of UV-irradiation time and (d) Approach Micrograph of c). The experimental conditions were: 1×10^{-3} M of H_{AuCl₄} solution kept at pH 7.2.

The energy-dispersive X-ray (EDS) spectra reflect a notable reduction of the zinc and oxygen signals from this phase. This fact could suggest that the ZnO was degraded during

this period deposition of Au under UV lamp. Similarly the silicon (Si) peak showed an increase in intensity as well as the Au peak. It is clearly observed that there are changes on intensities of the Zn, Si, Au and the disappearance of the oxygen peak in ZnO NRs. These intensities can be observed from the EDS spectrum in Figure 47a. The FE-SEM image shows that the ZnO NRs were deformed (Figure 47b). The plane (002) disappeared and usually it corresponds to maximum intensity of ZnO zincite wurzite structure. As discussed on section 5.4 XRD patterns confirmed the preferential growth on the (111) plane (refer to Figure 46a). The preferential growth of the (100) plane over the loss of the (200) plane evidenced the loss of columnar crystals. The reaction time played an important role for the optimized deposition of Au on ZnO/ZnO base film/ITO arrays.

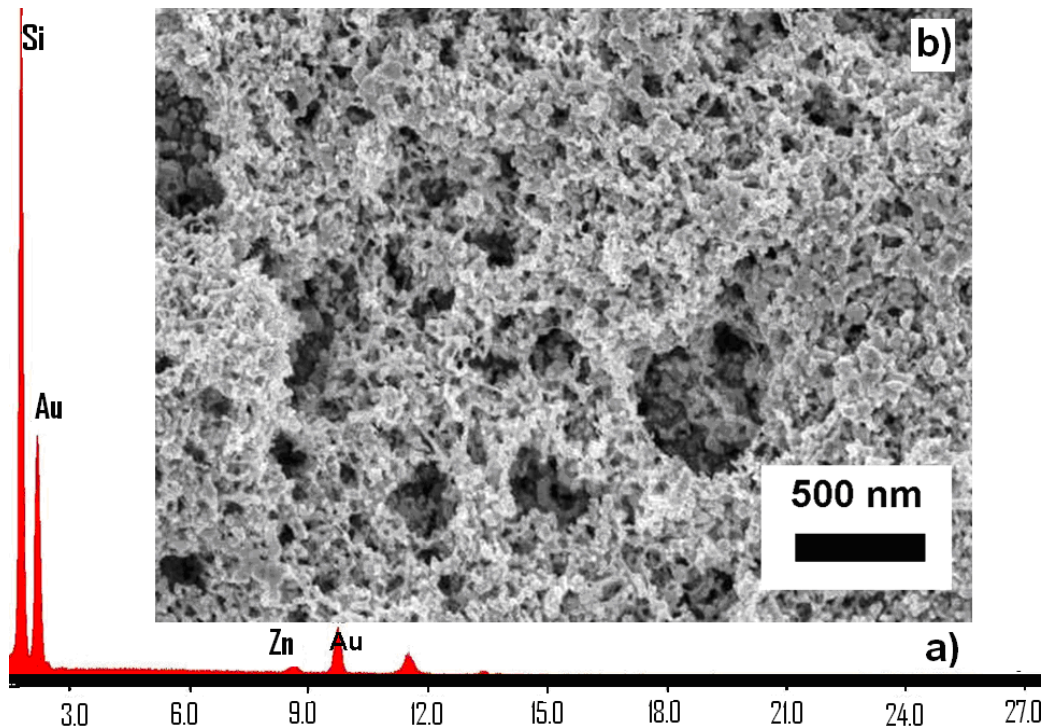


Figure 49. (a) EDS spectra for Au-coated ZnO NRs/ZnO base film/Si (100), 1×10^{-3} M HAuCl_4 with 4 hours of UV irradiation (b) FE-SEM images of ZnO NRs/ZnO/Si (100) morphology.

Figure 50a shows the FE-SEM image of ZnO NRs/ZnO base film/ITO at 0 hours of UV reaction time. After 2 hours under experimental condition with UV light, ZnO NRs/ZnO

base film/ITO were deformed. The reaction time for ZnO NRs/ZnO base film/ITO was shorter than for ZnO NRs/ZnO base film/Si. However the deformation of ZnO NRs is observed in the Fig 50b. This could be indicative of ITO acting as a catalyst, diminishing the reaction time and increasing the deformation in ZnO NRs/ZnO base film/ITO.

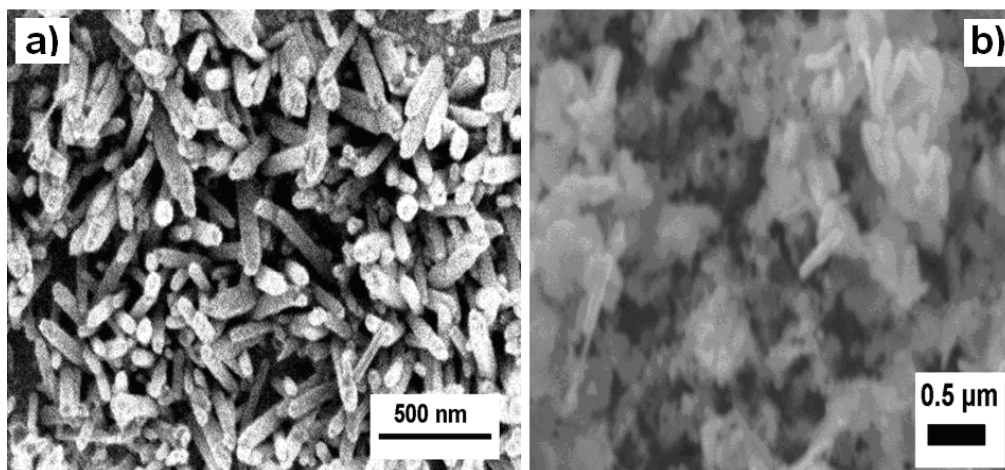


Figure 50. FE-SEM image of Au-coated ZnONR/ZnO base film/ITO, 1×10^{-3} M of HAuCl_4 solution kept at pH 7.2 with an UV-time reaction of: (a) 0 h (b) 2 h SEM image.

5.21 Surface Enhanced Raman Spectroscopy

Figure 51 shows the Raman spectrum for Au-coated ZnO NR/ZnO base film/Si(100) at 785 nm. The NRs were active for this excitation line. The band at 521 cm^{-1} is attributed to the silicon surface signal. A broad peak appears from 1500 up to 3000 cm^{-1} , from photoluminescence due to the gold coating.

4-ABT was selected as SERS probe molecule because it absorbs strongly on gold from a gold-sulfate bond [190] activity of the ZnONR. Figure 52 shows the normal Raman and SERS spectra for 4-ABT. Normal Raman was performed for 4-ABT using a concentrated analyte solution of 0.1 M in ethanol. Ethanol does not exhibit a pronounced SERS effect and for that reason can be used as an internal standard for determining the relative SEF values [191]. A small volume of 4-ABT sample was transferred to a glass capillary tube (1.5 x 90 mm) and placed in a homemade stainless steel holder for the SERS experiments under spot

laser experiments.

The intensities and peak areas could be calculated and compared to the normal bulk spectra (see Appendix A for more details). Relative Surface Enhancement Factors (SEF) were determined according to Equation 5.1. SEF, [192].

$$\text{SEF} = \frac{I_{\text{SERS}} * N_{\text{bulk}}}{I_{\text{bulk}} N_{\text{SERS}}} \quad (5.1)$$

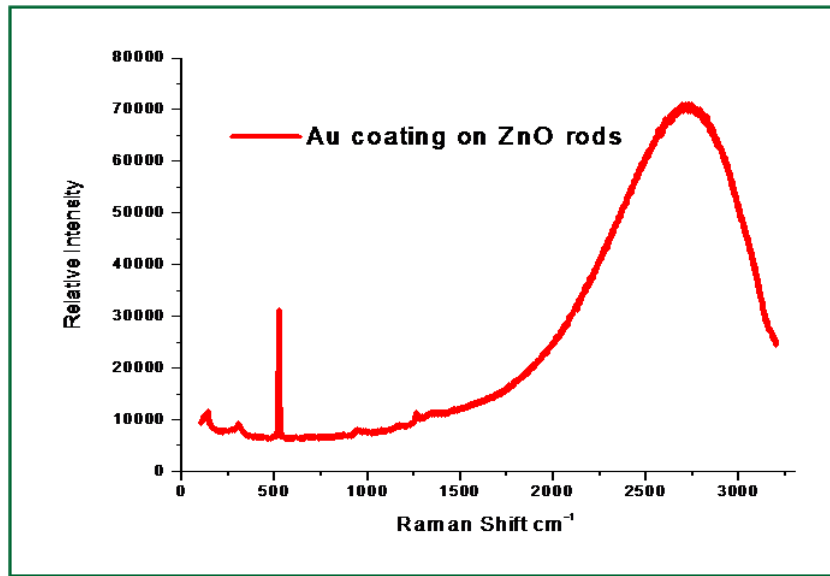


Figure 51. Raman spectrum of Au-coated on ZnO rods deposited onto base film on Si (100). Acquisitions were obtained at 3 accumulations, 10 s integration time using a laser power of 785.0 nm, 140 mW measured at head.

According to equation 5.1 shown, SERS intensity of a vibration mode I_{SERS} is given by the peak intensity. I_{bulk} is the peak intensity of a vibrational mode in the normal Raman spectrum (at high concentration). Therefore, the intensities were normalized to laser power and acquisition time with final units of $\text{counts} \cdot \text{mW}^{-1} \cdot \text{s}^{-1}$ at 1076 cm^{-1} . N_{bulk} and N_{SERS} are the average number of molecules sampled in the bulk and those adsorbed on the SERS active substrate illuminated by the laser, respectively. Furthermore, Le Ru et al have reported this formula is limited by some constraints and affected by major flaws, which can be severely amplified in the case of substrates characterized by a complex morphology, like nanorods,

nanowires and 3D architectures [193].

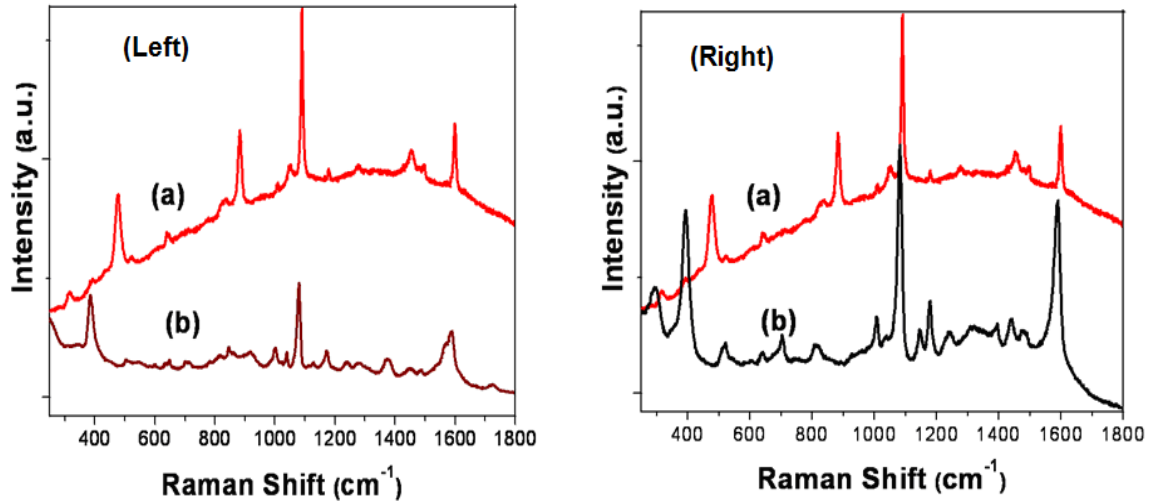


Figure 52. Comparison of 4-ABT Raman spectrum from (left) (a) 0.1 M 4-ABT on Au coating ZnO NRs/ZnO base film/Si from ion beam method. (b) 2 μL of a solution 1×10^{-4} M 4-ABT on Au coating ZnO NRs/ZnO base film/Si. (Right) 0.1 M 4-ABT on Au coating ZnO NRs/ZnO base film/Si from UV photo-reduction method. A similar procedure was used in both samples dissolved in ethanol prepared at an adjusted pH= 7.5 and mixed with 100 μL of 0.1 M sodium chloride (NaCl). Acquisitions were obtained at 3 accumulation, 10 s integration time using a laser power of 785.0 nm, 98 mW measured at head.

Figure 53 shows SERS of 4-ABT on Au coating ZnO NRs/ZnO base film/Si from both methods ion beam sputtering and UV light lamp. A peak at 390 cm^{-1} confirms that 4-ABT molecules are bound via a gold-sulfate bond. The Au-S mode increased in intensity with concentration from 1×10^{-8} M up to 1×10^{-4} M of 4-ABT. This last result indicates that 4-ABT was oriented perpendicular to the Au-coated ZnO NR surface [194]. On the other hand, 4-ABT detected from UV method for photo-reduction of Au Figure 19 (right) showed a noticeable increase of I_{SERS} with respect to ion beam sputtering method.

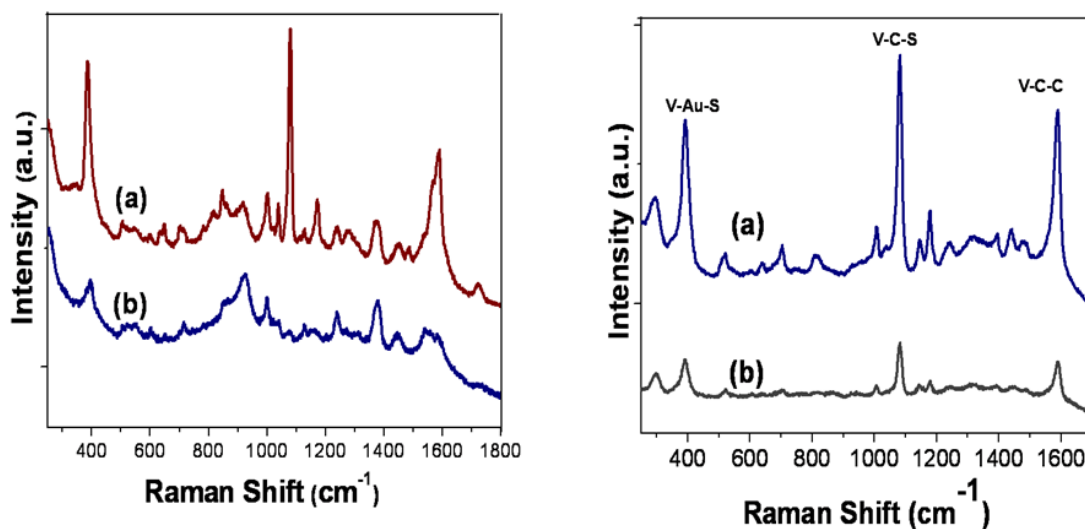


Figure 53. SERS of 4-ABT on (left) Au coating ZnO NRs/ZnO base film/Si by ion beam method (32nm) ;(a) 1×10^{-4} M 4-ABT, (b) 1×10^{-8} M 4-ABT. (Right) Au coating ZnO NRs/ZnO base film/Si UV light lamp (a) 1×10^{-4} M 4-ABT (b) 1×10^{-8} M 4-ABT on Au-ZnO NRs Spectra were acquired using a 785 nm laser with 98 mW (measured at head) at 3 accumulations, 10 s integration each time.

The enhancement of intensities of the peaks correspond to: C-S stretching (1075), C-H stretching (1171), C-H bend and C-C bending (1374) and the C-C stretching 1588 cm^{-1} [190]. These are mainly due to the field enhancement effect induced by surface plasmon polaritons of Au-coated ZnO NR [1].

Strong SERS of Raman spectra was observed for 4-ABT. However the experiments were realized with addition of Cl^- ions to increase the ionic strength effect. The results for all the concentrations are shown in Appendix A. A limit of detection (LOD) of 1×10^{-8} M for ABT was achieved corresponding to a minimum of 5.4×10^5 molecules detected under the experimental conditions at excitation wavelength of 785 nm with a sensitivity of the ZnO NRs in the range of 1.1×10^{-16} g under laser spot, with a SEF of 7.5×10^8 . The enhancement signal was induced by the chemical effect, due to an electronic resonance transfer between absorbed molecules and metal surface [36]. The contribution of chemical enhancement is in the order of 10^1 to 10^2 . Therefore the electromagnetic factor can be attributed to 10^6 up to

10^{14} . Both effects can contribute a high SERS enhancements factor for Au-coated ZnO NRs [191].

SERS experiments were performed taken a SERS mapping of thirty-two spots on an Au-coated ZnO NRs films to analyze the reproducibility under the lab conditions. The detection capabilities of Au-coated ZnO NRs substrates were evaluated with 4-ABT solutions over a wide range of concentrations from 1×10^{-4} up to 1×10^{-8} M. The results presented here show that good reproducibility expressed as relative standard deviation of 11.8% for ZnO NRs was found for these experiments as is showed in Figure 54.

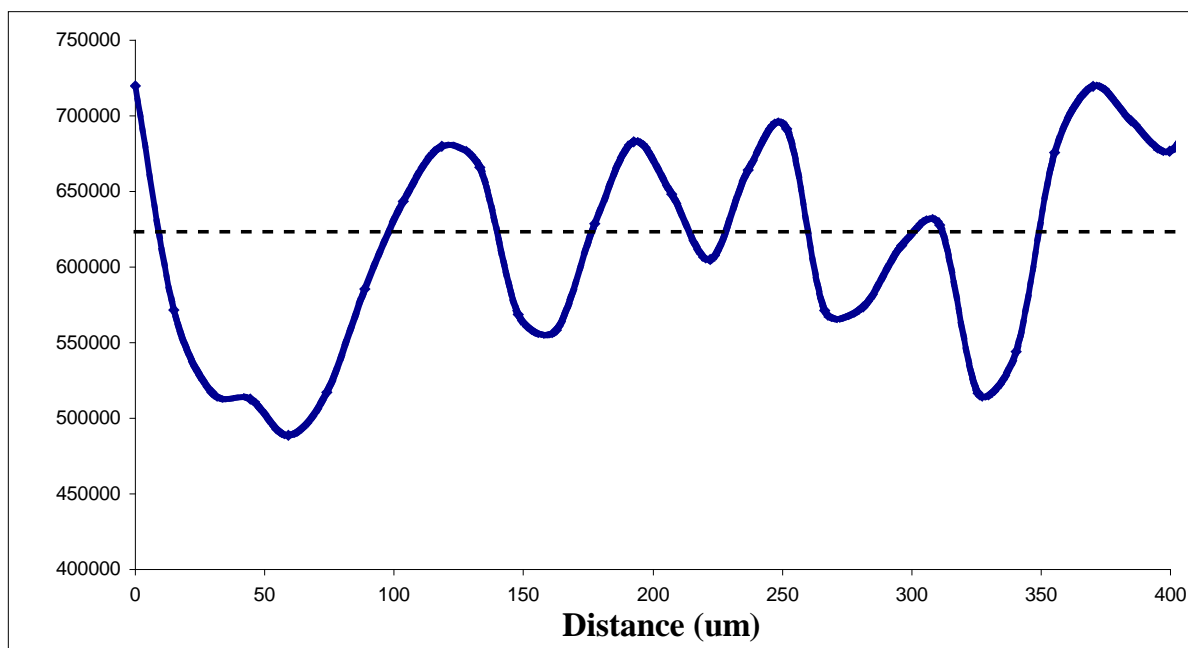


Figure 54. Mapping of 4- ABT on Au coating ZnO NRs/ZnO base film/si. to analyze the reproducibility in ZnO NRs coated with Au.

4-Nitrobenzenethiol was characterized at a wavelength of 785 nm for gold (Au) nanocoating on ZnO rod films. SERS spectra are shown on Figure 20 and measured using the Au-coated ZnO rods of 250 nm diameters. The mode at 1346 cm^{-1} is attributed to NO_2 stretching. Highly enhanced spectra were observed in the case of Au coated rod arrays at low concentration level of 7.7×10^{-10} g.

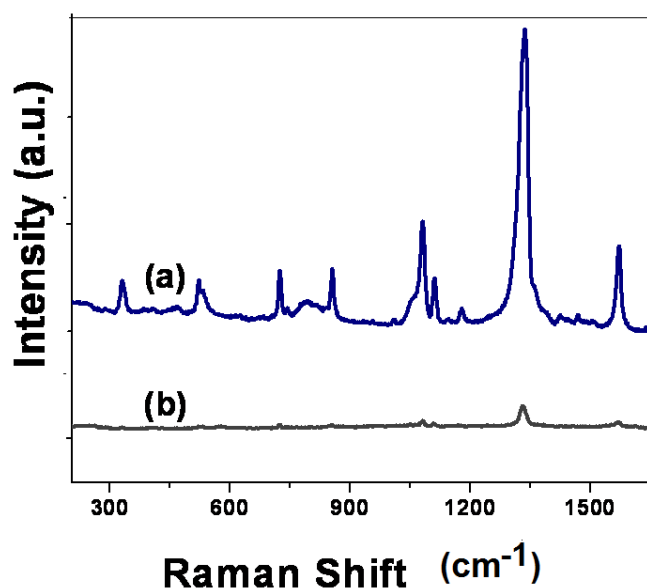


Figure 55. SERS of 4 Nitrobenzenethiol on Au coating ZnO rods/ZnO base film/Si by ion beam method (32nm) (a) 1×10^{-3} M 4-NBT, (b) 1×10^{-8} M 4-NBT were acquired at 3 accumulation, 10 s integration time using a laser power of 785.0 nm, 170 mW measured at head.

Particularly, the case of 4-NBT on ZnO NRs/ZnO base film/Si Raman spectral intensity was substantially enhanced because the concentration was lower than 7.7×10^{-10} g. The spectra originating from 4-NBT were obviously confirmed; exhibiting the high SERS enhancement factor as is shown in Figure 20a.

The results indicate that Au-coated ZnO NRs/ZnO base film/Si have a very high SERS activity due to the intense local electromagnetic field created by surface plasmon polaritons at the Au surface of each nanorod [3, 26]. 4-Nitrobenzenethiol was characterized at a wavelength of 785 nm for gold (Au) nanocoating on ZnO rods films as shown in Figure 20b. SERS spectra measured using the Au-ZnO NRs/ZnO base film/Si of 60 nm diameters. The mode of 1346 cm^{-1} is attributed to NO_2 stretching [195].

The relationship between area and concentration is shown in Figure 56. The information can be displayed in terms of intensity of a particular Raman signal or in terms of peak areas under a selected vibration band. 4-NBT was used as analyte. The NO_2 symmetric stretch at 1346 cm^{-1} in Figure 20 was integrated using Origin Pro 8.0 [196]. A monotonic

increase of peak areas was observed with increased concentration for 4-NBT. The results indicate that Au-coated grown ZnO NRs/ZnO base film/Si have higher SERS activity than Au-coated ZnO rod, was obviously confirmed, exhibiting the high SERS enhancement for a low level detection of 7.7 picograms with respect to 7.7×10^{-10} g for Au-coating on ZnO rod.

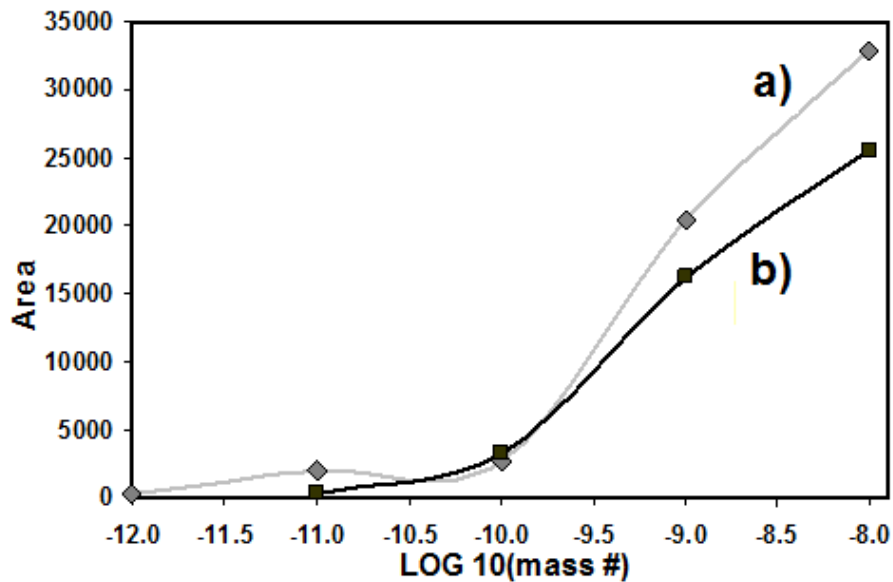


Figure 56. Peak area comparison from SERS spectra of 4-NBT of (a) Au-ZnO NRs and (b) Au-ZnO rods.

SERS spectra at 785 nm on ZnO NRs were activated with Au nano-coating. It is observed an enhancement of the C-C stretching mode at 1573-cm^{-1} or the in plane C-H bending mode at $1110\text{-}1082\text{ cm}^{-1}$ [192].

The vibration modes observed in the SERS spectrum of adenine molecules adsorbed on Au-coated coating ZnO NRs films were: 732.0, 953.3, 956.0, 1024.0, 1115.0, 1236.0, 1327.0 and 1396 cm^{-1} . These values were consistent with those found in Table 10.

Table 10. Raman spectral peak assignments of Adenine on Au coated coating ZnO NRs.

SERS	Normal Raman	Plane	Assignment
1397	1419	In	Str C ₄ -N ₉ , C ₄ -C ₅ , C ₆ -C ₁₀ , C ₇ -C ₈ bend C ₂ -H
1336	1333	In	Bend c ₂ -H, C ₈ H, N ₉ -H, str C ₆ -N ₁ , O ₈ -n ₉ , N ₃ -C ₄
1268	1248	In	Str C ₅ -N ₇ , N ₁ -C ₂ , bend C ₂ H, C ₂ N ₃
1244	1234	In	rock NH ₂ , str C ₅ -N ₇ , N ₁ -C ₂ , C ₂ -N ₃
1029	1025	In	rock NH ₂
961	942	In	Def R5 (sqz group N7-C8-N9)
790	797	Out	def-R6 (Wag C4-C58-C6), Wag C8-H
733	723	In	Ring breath whole molecule (distorted)

(Str: stretching bend: bending; rock: rocking; def: deforming; wag: wagging; breath: breathing; R5: five membered ring; R6: six-membered ring) [197].

SERS spectra for Au coating ZnO NRs/ZnO base film/Si of adenine assigned by McNaughton *et al.* [197]. A noticeable feature is the band at 732 nm characteristic of the Raman spectrum for adenine shown in Figure 57 (left).

Figure 57 (Right) shows SERS spectra at different concentrations of RDX on Au-coated ZnO NRs/ZnO base film/Si (100). The development of this method allowed for lowering of the detection limit of RDX in thin films. The 874 cm⁻¹ peak diminished in I_{SERS} to a concentration of 1x10⁻⁴ in comparison with in the concentration of 1x10⁻⁶ M of RDX. Raman bands assignments of RDX are as follow: the vibration mode at 930 cm⁻¹ is assigned to ring stretching and NO deformation signal intensity in SERS. The band at 874 cm⁻¹ is attributed to the symmetric ring-breathing mode; the band at 1258 cm⁻¹ is due to CH₂ scissoring and N-N stretch vibration; [198] the band at 1312 cm⁻¹ results from CH₂ wagging; the band at 1370 cm⁻¹ is ν NO₂ symmetric stretching vibration and β CH₂ scissoring; finally the band at 1560 cm⁻¹ is attributed to the ν NO₂ asymmetric stretch in nitroamines [198].

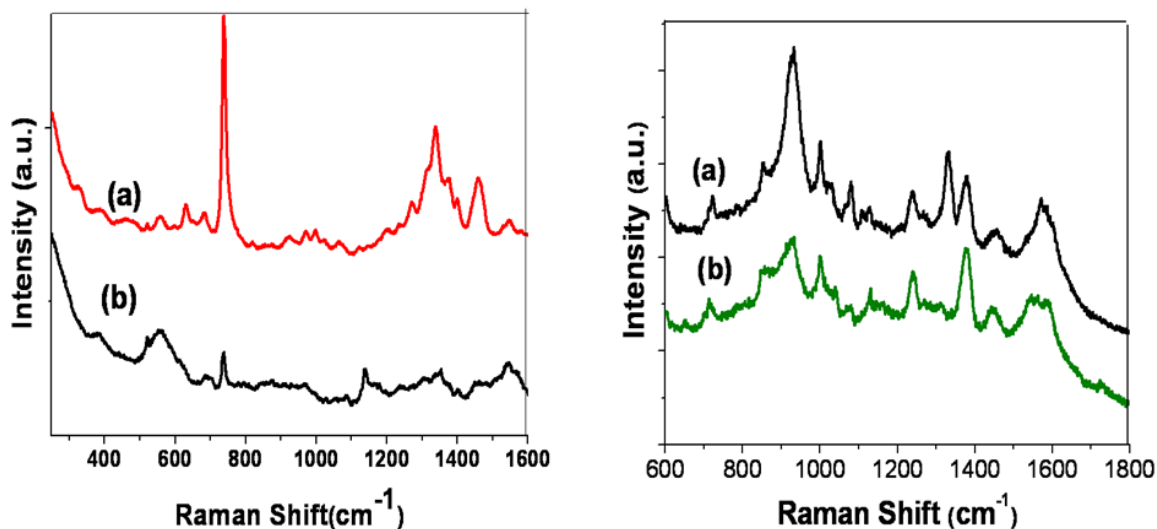


Figure 57. SERS of analytes on Au coating ZnO NRs/ZnO base film/Si. UV light lamp method. (Left) (a) 1×10^{-4} M adenine (b) 1×10^{-8} M. Right (a) RD 1×10^{-4} M (b) RDX 1×10^{-6} M, A similar procedure was used in both samples dissolved in ethanol prepared at an adjust adjusted pH= 7.5 and mixed with 100 μ L of 0.1 M sodium chloride (NaCl). Acquisitions were obtained at 3 accumulation, 10 s integration time using a laser power of 785.0 nm, 98 mW measured at head.

5.22 Conclusions

We have successfully synthesized Au-coated ZnO NRs/ ZnO base film/ Si (100) by UV method at room temperature. XRD characterization for ZnO NRs showed a higher intensity for the (111) plane and signals also appear for the (200) and (220) planes characteristic to the fcc Au-phase plane. UV light photoreduction of the gold (Au) coating on the ZnO NRs/ Zno base film/ Si (100) led to better enhancement of the SERS signals over gold deposited by the ion beam sputtering method. With this achievement, we were able to detect the explosive RDX at femtogram scale.

ZnO NRs/ ZnO base film/ ITO degraded within two hours after deposition of Au under UV lamp. Photooxidation of the Au coating was evidenced by an increase in intensity on both the silicon (Si) and gold (Au) peaks in the EDS spectrum (compare Figures 47 and 49). It is clearly observed that there are changes on intensities of the Zn, Si, Au and the

disappearance of the oxygen peak in ZnO NRs. This behavior has been previously reported and was attributed to the photocorrosive effect of ZnO under UV light [190].

The magnitude of the Raman scattered signal can be greatly enhanced when the scatterer is placed on or near a roughened noble-metal substrate. Strong electromagnetic fields are generated when the localized surface plasmon resonance (LSPR) of nanoscale roughness gold, are excited by visible light. The Au coated ZnO NRs/ ZnO base film /Si (100) present an associated stability in reference to their size with respect to Au-coated ZnO NRs/ ZnO base film /ITO under experimental condition with UV light irradiation for 2 hours. These ZnO NRs were reproducible and suitable for use as SERS sensors. 4-ABT was selected as SERS probe molecule because it absorbs strongly on gold. A limit of detection (LOD) of 1×10^{-8} M for ABT was achieved corresponding to a minimum of 5.4×10^5 molecules detected under the experimental conditions at excitation wavelength of 785 nm with a sensitivity of the ZnO NRs in the range of 19 femtogram under laser spot, with a SEF of 7.54×10^8 . The enhancement signal was induced by the chemical effect, due to an electronic resonance transfer between absorbed molecules and metal surface. The results presented here show that good reproducibility expressed as relative standard deviation of 11.8% for ZnO NRs was found for these experiments.

4-Nitrobenzenethiol was characterized at a wavelength of 785 nm on ZnO NRs/ ZnO base film /Si (100) grown nanorods and rods. The results indicate that Au coated ZnO NRs have a very high SERS activity due to the intense local electromagnetic field created by surface plasmon polaritons at the Au surface of each nanorod [1].

It has been demonstrated that Au coated ZnO NRs/ ZnO base film /Si (100) combined with SERS promises to be a good methodology for detection of adenine as well as RDX components. Low detection limits were found for these analytes: 19 femtograms under the laser spot. These limits of detection depend significantly on adjusting of pH and addition of Cl⁻ ions to increase the ionic strength effect, which induces electrostatic charge changes on the Au coated ZnO NRs surface.

CHAPTER 6: FUTURE WORKS

Prostate cancer is the second leading cause of cancer-related deaths in adult males in the United States. PSA, a 33-kDa glycoprotein, has been used as a prostate cancer marker since 1988[24].

The technique to be developed will achieve the rapid detection of cancer samples with high reliability and reproducibility. Ideally, multiple protein measurements in serum for cancer detection should feature low cost, high sensitivity accuracy, reproducibility and point of care application to avoid sample decomposition, facile rapid diagnosis and minimize patient stress. These requirements should be considered along with extensive number of proteins present in serum and low (pg mL^{-1}) normal level of biomarkers [199]. RAMAN provides a versatile platform for selective and sensitive detection of biomolecules of interest by SERS.

The future study could be addresses the current challenges in biosensor development, through the development of novel ZnO NRs materials for SERS biosensor, which should improve the sensitivity, reproducibility and stability. In addition, the proposed study provides the basis for the development of a biosensor that can be used for the detection of prostate, thyroid, and breast cancer.

CHAPTER 7: GENERAL REFERENCES

- [1] Tatsunori, J. Phys. D: App. phys. **41** (2008) 235304.
- [2] B. J. Bozleea, G. J. Exarhosb, Thin Solid Films 377–378 (2000) 1.
- [3] X. Wang, J. Phys. Chem. C. **111** (2007) 3836.
- [4] Z. Sun, Appl. Phys. Lett. **91** (2007) 221106.
- [5] Ch.L. Ching, Chem. Phys. Lett. **404** (2005) 30.
- [6] C. L. Haynes, A.D. McFarland, R.P. Van Duyne, Anal. Chem **77** (2005), 338A.
- [7] M. Fleischmann, P. J. Hendra, A. J. McQuillan, Chem. Phys. Lett. **26** (1974) 163.
- [8] A. Creighton, C.G. Blatchford, M.G Albrecht, J. Chem. Soc. Faraday Trans. II, **75** (1979) 790.
- [9] M. Balaguera, A. Burai, E. De La Cruz Montoya, J. Jerez, S. Hernández, Proc. SPIE, **6201** (2006) 62012C.
- [10] P. Lee, D. Meisel, J. Phys. Chem. **86** (1982) 3391.
- [11] Y. Xia, P. Yang, Y. Sun, Y. Wu, B. Mayers, B. Gates, Y. Yin, F. Kim, H. Yan, Adv. Mater. **15** (2003) 353.
- [12] M. Liao, L. Lu, J.C. Li, H. He, D.F. Wang, D.J. Fu, C. Liu, J. Phys. Chem. C **11** (2007) 1900.
- [13] K. Govender, D.S. Boyle, P.B. Kenway and P. O'Brien, J. Mater. Chem. **14** (2004) 2575.
- [14] Y. Wang, A. Brunsen, U. Jonas, J. Dostálek and W. Knoll, Anal. Chem. **81** (2009) 9625.
- [15] D. Byrne, E. McGlynn, K. Kumar, M. Biswas, M. O. Henry, and G. Hughes, Cryst. Growth Des. **10** (2010) 400.

- [16] L. Vayssieres, J. Phys. Chem. B **105** (2001) 3350.
- [17] J.S. Na, B. Gong, G. Scarel, G.N. Parsons, ACS Nano **10** (2009) 3191.
- [18] D. Wan, F. Huang, Y. Wang, ACS Appl. Mater. Interfaces **2** (2010) 2147.
- [19] X. Gao, X. Li and W. Yu, J. Phys. Chem. B **109** (2005) 1155.
- [20] Z. J. Wang, H.M. Zhang, L.G. Zhang, J.S. Yuan, J. Mater. Res **18** (2003), 151.
- [21] L. Vayssieres, N. Beermann. S. E. Lindquist, A. Hagfeldt, Chem. Mater. **13** (2001) 233.
- [22] N. Palomera, M. Balaguera, S. K. Arya, S. P. Hernández, M.S. Tomar, J. E. Ramírez, S. P. Singh, J. Nanosci. Nanotechnol. **11** (2011) 6683.
- [23] Z. J. Wang, H.M. Zhang, L.G. Zhang, J. S. Yuan, J. Mater. Res **18** (2003) 151.
- [24] F. Zhang, X. Wang, S. Ai, Z. Sun, Q. Wan, Z. Zhu, Y. Xian. L. Jin, K. Yamamoto, Analytica Chemical Acta. **519** (2004) 175.
- [25] J. M. James, A. J. James, J. D. Klein, K. M. Spencer. Analytical Chemical, **72** (23) (2000) 5834.
- [26] T. Y. Liu, T. K. Tong, W. H. Hsien, Y. Chen, Ch. Y. Hsuan, Langmuir. **22** (2006) 5804.
- [27] T. Nakada, Y. Hirabayashi, T. Tokado, D. Ohmori, and T. Mise, Sol. Energy **77** (2004) 739.
- [28] S. Y. Lee, E. S. Shim, H. S. Kang, S. S. Pang, and J. S. Kang, Thin Solid Films **437** (2005) 31.
- [29] R. Könenkamp, R. C. Word, and C. Schlegel, Appl. Phys. Lett. **85** (2004) 6004.
- [30] M. S. Wagh, L. A. Patil, T. Seth, and D. P. Amalnerkar, Mater. Chem. Phys. **84** (2004) 228.

- [31] H. Harima, J. Phys.: Condens. Matter **16** (2004) S5653.
- [32] Y. H. Leung, A. B. Djurisić, J. Gao, M. H. Xie, Z. F. Wei, S. J. Xu, W. K. Chan, Chem. Phys. Lett. **394** (2004) 452.
- [33] F. Liu, P. J. Cao, H. R. Zhang, J. Q. Li, and H. J. Gao, Nanotechnology **15** (2004) 949.
- [34] P.A. Hu, Y.Q. Liu, L. Fu, X.B. Wang, D.B. Zhu, Appl. Phys. A **78** (2004) 15.
- [35] S. Y. Bae, H. W. Seo, H. C. Choi, J. Park, J. Park, J. Phys. Chem. B **108** (2004) 12318.
- [36] H. Saeki, H. Tabata, T. Kawai, Solid State Commun. **120** (2001) 439.
- [37] S. Fujita, S.W. Kim, M. Ueda, S. Fujita, J. Cryst. Growth **272** (2004) 138.
- [38] H. Zhou, and Z. Li, Mater. Chem. Phys. **89** (2005) 326.
- [39] U. Özgür, I. Y. Alivov, C. Liu, A. Teke, M. A. Reshchikov, S. Dogan, V. Avrutin, S.J. Cho, H. Morkoc, J. Appl. Phys. **98** (2005) 041301.
- [40] J.E. Jafee, A.C. Hess, Phys. Rev. B **48** (11) (1993) 7903.
- [41] P. W. Tasker, J. Phys. C: Solid State Phys. **12** (1979) 4977.
- [42] O. Dulub, U. Diebold, G. Kresse, Phys. Rev. Lett. **90** (2003) 016102 .
- [43] A. Wander, F. Schedin, P. Steadman, A. Norris, R. McGrath, T.S. Turner, G. Thornton, N.M. Harrison, Phys. Rev. Lett. **86** (2001) 3811.
- [44] V. Staemmler, K. Fink, B. Meyer, D. Marx, M. Kunat, S.G. Gil, U. Burghaus, Ch. Woll Ch Phys. Rev. Lett. **90** (2003) 106102.
- [45] Y. Ding, X.Y. Kong, Z.L. Wang **57** (1998) 5674.
- [46] A.F. Kohan, G. Ceder and D. Morgan, Phys. Rev. B **61**(22) (2000-II) 15019.
- [47] A. Mang, S. Rübenacke, Solid State Commun. **94**(4) (1995) 251.
- [48] W.R.L. Lambrecht, Phys. Rev. B **65** (2002) 075207.
- [49] M. Cardona, Phys. Rev. **129** (1963) 69.

- [50] D. G. Thomas, *J. Phys. Chem. Solids* **15** (1960), 86.
- [51] S. Shionoya, W.H. Yen, *Phosphor Handbook* By Phosphor Research Society Press, Boca Raton, Florida, (1997) chap 7, Sect 7.
- [52] K. Vanheusden, W. L. Warren, C. H. Seager, D. R. Tallant, J. A. Voigt, B. E. Gnade, *J. Appl. Phys.* **79** (1996) 7983.
- [53] A. van Dijken, E. A. Meulenkamp, D. Vanmaekelberg, A. Meijerink, *J. Phys. Chem. B* **104** (2000) 1715.
- [54] X. Wang Y. Ding, C. J. Summers, Z. L. Wang, *J. Phys. Chem. B* **108** (2004) 8773.
- [55] J. Zhong, S. Muthukumar, Y. Chen, Y. Lu, H.M Ng, Jiang W, E.L Garfunkel, *Appl. Phys. Lett.* **83** (2003) 3401.
- [56] P.X. Gao P, Z. L.Wang, *Nano Lett.* **3**(2003) 1315.
- [57] P.X. Gao, Z.L Wang . *J. Phys. Chem. B* **106** (2002) 12653.
- [58] D. C. Look, J. W. Hemsky, J.R. Sizelove, *Phys. Rev. Lett.* **82**(1999) 2552.
- [59] A. Tsukazaki, A. Ohtomo, S.Yoshida, M. Kawasaki, C. H. Chia, T. Makino, Y. Segawa, T. Koida, S. F. Chichibu, H. Koinuma, *Appl. Phys. Lett.* **83** (2003) 2784.
- [60] C. Neumann, S. Lautenschlager, S. Graubner, J. Sann, N. Volbers, B.K Meyer, J. Blasing, A. Krost, F. Bertram, J. Christen, *Phys. Status Solidi b* **244** (2007) 1451.
- [61] R. Triboulet, J. Perriere, *Prog. Cryst. Growth Charact. Mater.* **47** (2003) 65.
- [62] S. J. Pearton, D.P. Norton, K. Ip, Y.W. Heo, *J. Vac. Sci. Technol. B* **22** (2004) 932.
- [63] V. Gupta, A. Mansingh, *J. Appl. Phys.* **80** (1996)1063.
- [64] H. Kind, H. Yan, B. Messer, M. Law, P. Yang, *Adv. Mater.* **14** (2002) 158.
- [65] Z. Fan, P. Chang, E. C. Walter, C. Lin, H. P. Lee, R. M. Penner, J. G. Lu, *Appl. Phys. Lett.* **85** (2004) 6128.

- [66] K. Keem, H. Kim, G. T. Kim, J. S. Lee, B. Min, K. Cho, M.Y. Sung, S. Kim, Appl. Phys. Lett. **84** (2004), 4376.
- [67] G.Y. Yeom and J. A. Thornton, J. Appl. Phys. **65** (10) (1989) 3816 .
- [68] K. Ellmer, J. Phys D: Appl. Phys, **33** (2000) R17.
- [69] K. Ho Kim, K. Cheol Park and D. Young Ma, J. Appl. Phys. **81**(12) (1997) 7764.
- [70] L. M. Angelats Silva, Msc. Thesis, University of Puerto Rico at Mayagüez, (2006) 18.
- [71] A. Belkind, A Freilich, J. Lopez, Z. Zhao, W. Zhu, K. Becker, New Journal of Physics **7** (2005) 90.
- [72] K. Ellmer, J. Phys. D: Appl. Phys. **34** (2001) 3097.
- [73] J. Robertson, Prog. Solid State Chem. **21** (1991) 199.
- [74] Th. Gruber, C. Kirchner, A. Waag, Phys. Stat. Sol. (b) **2** (2005) 841.
- [75] D.M. Gruen. Annu, Rev. Mater. Sci. **29** (1999) 211.
- [76] J. Philip, P. Hess, T. Feygelson, J.E. Butler, S. Chattopadhyay. K.H. Chen, L.C. Chen, J. Appl. Phys. **93** (2003) 2164.
- [77] G.M. Swain, A.B. Anderson, J.C. Angus, Mater.Res.Bull. **23** (1998) 56.
- [78] J.A. Mucha, D.L. Flamm, D.E. Ibbotson, J. Appl. Phys. **65** (1989) 3448.
- [79] K. Teii, H. Ito, M. Hori, T. Takeo, T. Goto, J. Appl. Phys. **87** (2000) 4572.
- [80] Y. Kouzuma, K. Teii, K. Uchino, K. Muraoka, Phys. Rev. B **68** (2003) 064104.
- [81] X. Y. Kong, Z. L. Wang, Nano. Lett. **3** (2003) 1625.
- [82] P. Chang, Z. Fan, W. Tseng, D. Wang, W. Chiou, J. Hong, J. G. Lu, Chem. Mater. **16** (2004) 5133.
- [83] H. Y. Dang, J. Wang, and S. S. Fan, Nanotechnology **14** (2003) 738.
- [84] M. H. Huang, Y. Wu, H. Feick, N. Tran, E. Weber, P. Yang, Adv. Mater. **13** (2001)

- [85] S. Y. Li, C. Y. Lee, T. Y. Tseng, *J. Cryst. Growth* **247** (2003) 357.
- [86] X. Kong, X. Sun, X. Li, Y. Li, *Mater. Chem. Phys.* **82** (2003) 997.
- [87] W. D. Yu, X. M. Li, and X. D. Gao, *Appl. Phys. Lett.* **84** (2004) 2658.
- [88] H. T. Ng, J. Han, T. Yamada, P. Nguyen, Y. P. Chen, M. Meyyappan, *Nano. Lett.* **4** (2004) 1247.
- [89] J. Y. Lao, J. G. Wen, Z. F. Ren, *Nano. Lett.* **2** (2002) 1287.
- [90] J. G. Wen, J. Y. Lao, D. Z. Wang, T. M. Kyaw, Y. L. Foo, Z. F. Ren, *Chem. Phys. Lett.* **372** (2003) 717.
- [91] D. Banerjee, S. H. Jo, and Z. F. Ren, *Adv. Mater.* **16** (2004) 2028.
- [92] J. Y. Lao, J. Y. Huang, D. Z. Wang, and Z. F. Ren, *J. Mater. Chem.* **14** (2004) 770.
- [93] S. Y. Bae, H. W. Seo, H. C. Choi, J. Park, J. Park, *J. Phys. Chem. B* **108** (2004) 12318.
- [94] Y. Dai, Y. Zhang, and Z. L. Wang, *Solid State Commun.* **126** (2003) 629.
- [95] B. D. Yao, Y. F. Chan, N. Wang, *Appl. Phys. Lett.* **81** (2002) 757.
- [96] R.S. Wagner, W.C. Ellis. *Appl. Phys. Lett.* **4** (1964) 89.
- [97] J. Westwater, D.P Gosain, S. Tomiya, S. Usui, H.J. Ruda, *Vac. Sci. Technol. B* **15** (1997) 554.
- [98] A.M. Morales, C.M Lieber, *Science* **279** (1998) 208.
- [99] X . Y. Kong, Y. Ding, R.S Yang, Z.L. Wang, *Science* **303** (2004) 1348 .
- [100] X . Y. Kong, Ding, Z.L Wang, *J. Phys. Chem. B* **108** (2004) 570.
- [101] I. Smolyaninov, D.L Mazzoni, C.C. Davis, *Phys. Rev. Lett.* **77** (1996) 3877.
- [102] E. C. Greyson, Y. Babayan, T. W. Odom, *Adv. Mater.* **16** (2004) 1348.
- [103] H. J. Fan, F. Fleischer, W. Lee, K. Nielsch, R. Scholz, M. Zacharias, U. Gösele, A.

- Dadgar, A. Krost, Supperlattice Microst. **36** (2004) 95.
- [104] H. Chik, J. Liang, S. G. Cloutier, N. Kouklin, J. M. Xu, Appl. Phys. Lett. **84** (2004) 3376.
- [105] D. Banerjee, S. H. Jo, and Z. F. Ren, Adv. Mater. **16** (2004) 2028.
- [106] Y. J. Xing, Z. H. Xi, Z. Q. Xue, X. D. Zhang, J. H. Song, R. M. Wang, J. Xu, Y. Song, S. L. Zhang, D. P. Yu, Appl. Phys. Lett. **83** (2003)1689.
- [107] Y.K. Tseng, C.J. Huang, H.M. Cheng, I.N. Lin, K.S. Liu, I.-C. Chen, Adv. Funct. Mater. **13** (2003) 811.
- [108] Y. W. Zhu, H. Z. Zhang, X. C. Sun, S. Q. Feng, J. Xu, Q. Zhao, B. Xiang, R. M. Wang, D. P. Yu, Appl. Phys. Lett. **83** (2003) 144.
- [109] H. Z. Zhang, R. M. Wang, Y. W. Zhu, J. Appl. Phys. **96** (2004) 624.
- [110] Y. B. Li, Y. Bando, and D. Golberg, Appl. Phys. Lett. **84** (2004) 3603.
- [111] C. X. Xu, X. W. Sun, Appl. Phys. Lett. **83** (2003) 3806.
- [112] S. H. Jo, D. Banerjee, and Z. F. Ren, Appl. Phys. Lett. **85** (2004)1407.
- [113] C. J. Lee, T. J. Lee, S. C. Lyu, Y. Zhang, H. Ruh, H. J. Lee, Appl. Phys. Lett. **81** (2002) 3648.
- [114] D. C. Look, D. C. Reynolds, C. W. Litton, R. L. Jones, D. B. Eason, G. Cantwell, Appl. Phys. Lett. **81** (2002) 1830.
- [115] P. Yang, H. Yan, S. Mao, R. Russo, J. Johnson, R. Saykally, N. Morris, J. Pham, R. He, H.J. Choi, Adv. Mater. **12** (2002) 323.
- [116] X. Wang, C.J. Summers, and Z.L. Wang, Nano Lett. **4** (2004) 423.
- [117] H. J. Fan, F. Bertram, A. Dadgar, J. Christen, A. Krost, and M. Zacharias, Nanotechnology **15** (2004) 1401.

- [118] S. Y. Li, P. Lin, C. Y. Lee, M. S. Ho, T. Y. Tseng, *J. Nanosci. Nanotech.* **4** (2004) 968.
- [119] Y.K. Tseng, C.T. Chia, C.Y. Tsay, L.J. Lin, H.M. Cheng, C.Y. Kwo, I.C. Chen,
J. Electrochem. Soc. **152** (2005) G95.
- [120] C. Geng, Y. Jiang, Y. Yao, X. Meng, J. A. Zapien, C. S. Lee, Y. Lifshitz, and S. T. Lee, *Adv. Funct. Mater.* **14** (2004) 589.
- [121] Y. Zhang, H. Jia, R. Wang, C. Chen, X. Luo, D. Yu, and C. Lee, *Appl. Phys. Lett.* **83** (2003) 4631.
- [122] J.J. Wu, S.C. Liu, *Adv. Mater.* **14** (2002) 215.
- [123] J. Park, H.H. Choi, K. Siebein, R. K. Singh, *J. Cryst. Growth* **258** (2003) 342.
- [124] N. A. Milne, M. Skyllas, V. Luca, *J. Phys. Chem. C*, **113** (30) (2009) 12983.
- [125] C. Burda, X. Chen, R. Narayanan, M.A. El-Sayed, *Chem. Rev.* **105** (2005) 1025.
- [126] Z. Wei, L. Yang, Z. Tie-Kai, X. Weiping, Z. Meng Zhang, Y. Shu-Hong, *J. Phys. Chem. C*, **112** (2008)19872.
- [127] V. Rotello, *Nanoparticles: Building Blocks for Nanotechnology* (Kluwer Academic/Plenum Publishers: New York, 2004).
- [128] S. Link and M.A. El-Sayed, *Annu. Rev. Phys. Chem.* **54** (2003) 331.
- [129] U. Kreibig and M. Vollmer, *Optical Properties of Metal Clusters*, **25** (1995) series in *Materials Science*, Springer, Berlin, XVII, 532 .
- [130] G.W. Arnold and J.A. Borders, *J. Appl. Phys.* **48** (1977) 1488.
- [131] P.B. Johnson and R.W. Christy, *Phys. Rev. B* **6** (1972) 4370.
- [132] T. Hayakawa, S.T. Selvan, M. Nogami, *J. Non-Cryst. Solids* **259** (1999) 16 .
- [133] J. Yoo, J. Lee, S. Kim, K. Yoon, I. J. Park, S.K. Dhungel, B. Karunagaran, D. Mangalaraj, J. Yi, *Thin Solid Films* **480-481**(2005) 213.

- [134] T. J. Coutts, X. Li, T.M. Barnes, B.M. Keyes, L.P Craig , S.E Asher, S.B. Zhang, S.H. Wei, Zinc Oxide Bulk, Thin Films, and Nanostructures, C. Jagadish and S. J. Pearton, editors, (2006) New York.
- [135] Z.R. Tian, J.A. Voigt, J. Liu, B. Mckenzie, M.J. Mcdermott, M.A. Rodriguez, H. Konishi, H. Xu, Nature materials **2** (2003) 821.
- [136] S.C. Liou, C.S. Hsiao, S.Y. Chen, J. Cryst. Growth **274** (2005) 438.
- [137] J. Zhang, L. Sun, J. Yin, H. Su, Ch. Liao, Ch. Yan, Chem. Mater. **14** (2002) 417.
- [138] Lori E. Greene, Benjamin D. Yuhas, Matt Law, David Zitoun, and Peidong Yang Inorg. Chem. **45** (2006) 7535.
- [139] K. Vanheusden, W. L. Warren, C. H. Seager, D. R. Tallant, J. A. Voigt, B. E. Gnade, J. Appl. Phys. **79** (1996) 7983.
- [140] R.C. Wang, L.H. Ying, C.H. Shu, L.Y. Feng and R.S. Huang, Appl. Phys A. **96** (2009) 775.
- [141] L. Vayssieres, N. Beermann. S. E. Lindquist, and A. Hagfeldt, Chem. Mater.**13** (2001) 233.
- [142] A. Sugunan, H.C. Warad, M. Boman, J. Dutta, Journal of Sol Gel Science & Technology **39** (2006) 49.
- [143] A. van Dijken, E. A. Meulenkaamp, D. Vanmaekelberg, A. Meijerink, J. Phys. Chem. B **104** (2000) 1715.
- [144] Y.C. Wang, I.C. Leu and M. H. Hon, J. Cryst. Growth **564** (2002) 237.
- [145] F. Zhang, Analytica Chemical Acta. (2004) 519.
- [146] B. Pettinger, Phys. Rev. Lett. **92** (2004) 151.
- [147] L. Yu-Chuan, J. Material Chemistry. **17** (2007) 2120 .

- [148] P. Lee, D. Meisel, *J. Phys. Chem.* **86** (1982), 339.
- [149] K.M. Spencer, J.M. Sylvia, S.L. Clauson, J.F. Bertone, S.D. Christesen, *Proc. SPIE.* **5268** (2004) 340.
- [150] T. M. Cotton, E. S. Brandt, In *Physical Methods of Chemistry Series: Investigations of Surfaces and Interfaces, Part B*, second edition, John Wiley & Sons, New York, IXB (1993) .
- [151] J. Callum, R. McHugh, G. Duncan, W.E. Smith, *Chemical communication.* (2002), 580.
- [152] H.C. Ming. *Journal Physics Chemical B.* **109** (2005) 18385.
- [153] Y. Cedeño, Doctor of Philosophy, Thesis, University of Puerto Rico at Mayagüez, (2010).
- [154] T.Y. Liu, H.C. Liao, Ch. Lin, SH. Hu and S.Yuan, *Langmuir* **22** (2006) 5804.
- [155] S.K. Panda. C. Jacob, *Physica E.* **41** (2009), 792.
- [156] R. Cebulla, R. Wendt, K. Ellmer, *J. App. Phys.* **83** (1998) 1087.
- [157] D. Byrne, E. McGlynn, K. Kumar, M. Biswas, M. O. Henry, and G. Hughes, *Cryst.Growth Des.* **10** (2010) 400.
- [158] D. Wan, F. Huang, and Y. Wang, *ACS Appl. Mater. Interfaces* **2** (2010), 2147
G.W. Arnold and J.A. Borders, *J. Appl. Phys.* 48 (1977)1488.
- [159] B.D. Cullity, S.R. Stock, *Elements of X-ray diffraction*, third edition, Prentice Hall, New Jersey (2001) .
- [160] <http://www.files.chem.vt.edu/chem-ed/spec/uv-vis/singlebeam.html>. Copyright © 2000 by Brian M. Tissue, all rights reserved.
- [161] K. Brandenburg and H. Putz, *Match Phase identification from powder diffraction*,

crystal Impact (2003-2006) Postfach 12 51, D-53002 Bonn Germany.

[162] J. Shackelford. Introduction to Materials Sciences for Engineers, fourth edition, Prentice Hall, New Jersey (1996).

[163] R.F Egerton, Physical principles of electron microscopy : an introduction to TEM, SEM, and AEM, Springer, Edmonton, Alberta (2005).

[164] S. Jáuregui, Msc. Thesis, University of Puerto Rico at Mayagüez, (2008).

[165] K.C.Barick, S. Singh, M.Asalam, D.Bahadur, MicroporousMesoporousMater.134 (2010) 195.

[166] C. Agashe, O. Kluth, J. Hupkes, U. Zastrow, B. Rech, J. Appl. Phys. **95** (2004) 1911.

[167] Z.R. Tian, J.A. Voigt, J. Liu, B. Mckenzie, M.J. Mcdermott, M.A. Rodriguez, H. Konishi, and H. Xu, Nature materials **2** (2003) 821.

[168] J. Liu, Z. Guo, F. Meng, Y. Jia, T. Luo, M. Li, J. Liu, Cryst. Growth Des. **9** (2009) 1716.

[169] N.S. Pesika, K. J. Stebe and P. C. Searson J. Phys. Chem. B **107** (2003) 1041.

[170] X. Liu, X. Wu, H. Cao, R. P. Chang, J. Appl. Phys. **95** (2004) 3141.

[171] D. Wang, H. W. Seo, C.C. Tin, M. J. Bozack, J. R. Williams, M. Park, N. Sathitsuksanoh, A. Cheng, Y. H. Tzeng, J. Appl. Phys. **99** (2006) 113509.

[172] J. A. Aparicio, F. E. Fernandez, J Mater Sci., **45** (2010) 6009.

[173] L. Yanhong, W. Dejun, Z. Qidong, Y. Min and Z. Qinglin, J. Phys. Chem. B **108** (2004) 3202.

[174] L. Clément. Semiconductor electrodes and photoelectrochemistry. In: Encyclopedia of Electrochemistry, WILEY-VCH, Weinheim (2002) 185.

- [175] Y.C. Wang, I.C. Leu, M. H. Hon, J. Cryst. Growth. **564** (2002) 237.
- [176] X. Gao, X. Li, W. Yu J. Phys. Chem. B **109** (2005) 1159.
- [177] X. Hu, Y. Masuda, T. Ohji and K. Kato, Thin Solid Films **518** (2009), 90.
- [178] D.C. Reynolds, D.C. Look, B. Jogai, C.W. Litton, T.C. Collins, W. Harsch, G. Cantwell. Phys. Rev. B. **58** (1998), 13276.
- [179] J. L. Chen, L. Luo, Z. Chen, M. Zhang, J. A. Zapien, C. S. Lee and S. T. Lee. J. Phys. Chem. C **114** (2010) 93.
- [180] A. Dev, S.A. Panda, S. Kar, S. Chakrabarti and S. Chaudhuri. J. Phys. Chem. B **110** (2006)14266.
- [181] D.J. Park, D.C. Kim, J.Y. Lee and H.K. Cho, Nanotechnology **17** (2006), 5238.
- [182] Y. Xia, P. Yang, Y. Sun, Y. Wu, B. Mayers, B. Gates, Y. Yin and F. Kim, H. Yan, Adv. Mater. **15** (2003) 353.
- [183] L.E. Greene, M. Law, D. H. Tan, M. Montano, J. Goldberger, G. Somorjai, P.D. Yang, Nano Lett. **5**, **1231** (2005) 1231.
- [184] X. Hu, Y. Masuda, T. Ohji and K. Kato, Thin Solid Films **518** (2009) 906.
- [185] I. Lee, S. W. Han, C.H. Kim, T. G. Kim, S. W. Joo, D.J. Jang, K. Kim, Langmuir **16** (2000) 9963.
- [186] M. Schulz-Dobrick, K. V. Sarathy, M. J. Jansen, J. Am. Chem. Soc. **127** (2005) 12816.
- [187] N. R. Jana, X. G. J. Peng, J. Am. Chem. Soc. **125** (2003) 14280.
- [188] M. P. Rowe, K. E. Plass, K. Kim, C. Kurdak, E. T. Zellers, A. Matzger, J. Chem. Mater. **16** (2004) 3513.
- [189] K. Yee, R. Jordan, A. Ulman, H. White, A. King, M. Rafailovich, J. Sokolov, Langmuir **15** (1999) 3486.

- [190] N. Nadagouda, G. Hoag, J. Collins, R. Varma, *Cryst. Growth Des.* **9** (2009) 4979.
- [191] Z. Quing, L. Yang, Z. Tié, X. Weiping, Z. Meng, Y. Shu, *J. Phys. Chem. C* **112** (2008) 19872.
- [192] Yamamoto, M. Nakamoto, *J. Mater. Chem.* **13** (2003) 2064.
- [193] K. Kim, J.K. Yoon, *J. Phys. Chem. B* **109** (44) (2005) 20731.
- [194] E. A. Mamdouh, *Cent. Eur. J. Chem.* **7** (3) (2009) 446.
- [195] R. Puebla, B. Cui, J. Bravo, T. Veres, H. Fenniri, *J. Phys. Chem. C* **111** (2007) 6720.
- [196] E. C. Le Ru, E. Blackie, M. Meyer, P.G. Etchegoin, *J. Phys. Chem. C* **111** (2007) 13794.
- [197] O. Primera-Pedrozo, Doctor of Philosophy, Thesis, University of Puerto Rico at Mayagüez, (2010).
- [198] S. Woo, I. Lee, K. Kim, *Langmuir* **18** (2002) 82.
- [199] M. Balaguera, Msc. Thesis, University of Puerto Rico at Mayagüez (2006).
- [200] Y. Watanabe, Y. Ishida, N. Hayazawa, Y. Inouye, S. Kawata, *Physical Review B* **69** (2004) 1
- [201] A. Nahla, Hatab, E. Gyula, P. Hatzinger, B. Gua, *J. Raman Spectrosc.* **41** (2010) 1131
- [202] T. J. Polascik, J. E. Oesterling, A.W. Partin, *J. Urol.* **162**, (1999) 29
- [203] J.H. Lin, F. Yan, X.Y. Hu, H.X. Ju, *J. Immunol Methods.* **291** (2004) 165

**APPENDIX A: SENSITIVITY CALCULATION FOR AU COATING
ZNO NRS/ZNO BASE FILM/SI.**

OBJECTIVE 10X			
<i>SPOT</i>	<i>90 μm x 50 μm</i>		
<i>μm, length</i>	<i>μm, width</i>	<i>Length, cm</i>	<i>Width, cm</i>
90	50	0.009	0.005
<i>Capillar diameter, mm</i>	<i>Capillary diameter, cm</i>	<i>Radius, cm</i>	
1.5	0.15	0.075	
	<i>Area laser x capillar diameter</i>		
<i>Illuminated volume(cm³)</i>	6.75E-06		
<i>Illuminated volume(μL)</i>	6.75E-03		
[4-ABT, M]	moles/μL	<i>Illuminated volume(μL)</i>	<i>Moles 4-ABT under laser spot</i>
1.00E-03	1.00E-09	6.75E-03	6.75E-12
1.00E-04	1.00E-10	6.75E-03	6.75E-13
1.00E-05	1.00E-11	6.75E-03	6.75E-14
1.00E-06	1.00E-12	6.75E-03	6.75E-15
1.00E-07	1.00E-13	6.75E-03	6.75E-16
1.00E-08	1.00E-14	6.75E-03	6.75E-17
1.00E-09	1.00E-15	6.75E-03	6.75E-18
1.00E-10	1.00E-16	6.75E-03	6.75E-19
	<i>Sensitivity, (Δlog Peak area)/ΔC</i>	<i>Average</i>	<i>STDEV</i>
	0.97	0.93	0.17
	1.18		
	0.87		
	0.90		
	0.71		

APPENDIX B: SEF VALUES FOR AU COATING ZNO NRS/ZNO BASE FILM/SI (100).

Concentration [M]	I_{SERS}	I normalized (SERS)	N_{Bulk}	I_{Bulk} (0.1 M)	I_{Bulk} (normalized)	N 4-ABT (molecules/cm²)	N_{SERS}	SEF
1*10 ⁻⁴	69255.44	4073.84	1.094*10 ¹⁶	73476.31	4322.13	8.13*10 ⁹	1.26*10 ⁶	1.27E+06
1*10 ⁻⁵	40580.58	2387.09	1.094*10 ¹⁶	73476.31	4322.13	8.13*10 ⁸	1.34*10 ⁷	7.43E+06
1*10 ⁻⁶	17122.94	1007.23	1.094*10 ¹⁶	73476.31	4322.13	8.13*10 ⁷	1.34*10 ⁸	3.14E+07
1*10 ⁻⁷	14434.79	849.10	1.094*10 ¹⁶	73476.31	4322.13	8.13*10 ⁶	1.34*10 ⁹	2.64E+08
1*10 ⁻⁸	4116.0	242.11	1.094*10 ¹⁶	73476.31	4322.13	8.13*10 ⁵	1.34*10 ¹⁰	7.54E+08

APPENDIX CHAPTER 8: Gold-coated Silica Nanowires for Immunoassay based on Surface Enhanced Raman Spectroscopy

Marcia Balaguera-Gelves^a Oscar Perales-Pérez^b, Surinder Singh^b, Sunil K. Arya^c, Shekhar Bhansali^c, Eduardo Murphy-Pérez^c and Samuel P. Hernández-Rivera^{a,*}

^aDepartment of Chemistry, University of Puerto Rico, P.O. Box 9000, Mayagüez, PR 00681, USA
Department of Engineering Science and Materials, University of Puerto Rico, P.O. Box 9000,
Mayagüez, PR 00681, USA.

^cDepartment of Electrical Engineering, University of South Florida, Tampa, FL 33620

8.1 Abstract

The detection of prostate specific antigen (PSA) at a very low concentration by Surface Enhanced Raman Spectroscopy (SERS) immunoassay using antigen-antibody binding has been demonstrated. Antibody specific to PSA antigens were immobilized covalently on gold coated Silica nanowires (SiO₂ NWs), which were functionalized onto dithiobis succinimidyl propionate (DTSP) The amine groups of DTSP covalently bonded to tracer antibodies by formation of an amide linkage The immobilized antibody was used to capture PSA antigen and SERS immunoassay was utilized for detection. SERS results are due to the field-enhancement effect induced by surface plasmon polaritons of Au-coated nanowires. Results reveal a superior selectivity and sensitivity for detection of PSA samples at about 1 pg/mL in concentration at an excitation wavelength of 632 nm laser.

8.2 Introduction

Progress in health care prevention associated with pathogen detection, immunoassays based on antigen-antibody binding have demonstrated advantages in their speed, selectivity and affinity for the desired biomarker [1-3]. Recent developments in nanotechnology, along with the demonstration of various quantum size effects in nanoparticles, nanocomposites,

allow a variety of nanostructures applications [4-10]. Studies have been reported for silica nanowires with a special concern for nanowires or nanorod structures. These are of interest due to their potential application in chemical sensors, rigid template; SERS based biosensor and other device applications [11-13].

Antibody immobilizations in immunoassays have become more prevalent, due in part to the development of immunosensors and other innovations. Coupling of these assays with readout technologies and appropriate materials to address performance characteristics such as detection limit is still a major priority [14-19]. A technique for immobilization of antibodies uses dithiobis succinimidyl propionate (DTSP) or dimercaptosuccinic acid on gold surfaces [20]. Thus, antibody immobilization using DTSP antibodies for one portion and physical adsorption for the other is a desirable goal in and of itself.

Various research articles have tested the importance of protein orientation, and their results support this hypothesis [20, 21]. Much of the research of orientation supports the claim that oriented antibodies yield better results, such as higher sensitivity of immunoassays, higher antigen-binding capacity, and more structured properties than randomly oriented antibodies.

In blood plasma, PSA exists in both complexed and free forms, with normal levels of total PSA between 4 and 10 ng/mL. The predominant form of serum PSA is a complex with R1- antichymotrypsin, with lesser amounts bound with R2-macroglobulin and R1-antitrypsin [22, 23]. Currently used assays distinguish between the different forms of PSA through unreacted epitopes in each complex. The distinction between complexed and free PSA is clinically relevant because the occurrence probability of cancer increases as the percentage of

free PSA decreases [22, 24]

Previous works [20] explain whether specific antibody orientation improves antigen binding activity in immunoassay and results show that experiment on the relative binding affinity of DTSP as compared with physical adsorption is required. The present study investigated Au coated SiO₂ Nanowires films. This surface has excellent optical properties for a sensitive detection of prostate-specific antigen (PSA). PSA is a glycoprotein consisting of one polypeptide chain, has been used as a serologic marker for detecting prostate cancer [22].

Recently, Surface Enhanced Raman Scattering (SERS) has received much attention in sensitive optical detection and spectroscopy due to its potential in high selective and sensitive detection of single molecules in solution [8-10]. SERS has been a promising technique for various applications in chemical-biochemical analysis, nanostructure characterization and biomedical applications [27]. Especially, SERS immunoassays based on proteins, antibody fragments, DNA fragments, and RNA fragments have been used as targets in cancer detection. This nonradioactive tagging technology is a safe and stable methodology capable to overcome problems in sample analysis such as interfering water absorption and overlapping signals from competing analytes [1-3, 8, 10, and 23]. However, not all molecules of interest have a chromophore that coincides with the commonly used visible lasers, and appropriate SERS signals are acquired from materials having a characteristic surface plasmon resonance that matches the excitation frequency [5, 25]. The intensity of the Raman-scattered light can be magnified by adsorbing the target molecule onto a roughened metal surface.

Platforms with Raman-enhancing properties that include the use of organic dyes in colloidal solutions, roughened metal surfaces and the use of metal nanoparticles encapsulated in polymers [25-27] have been used with different attachment methods to entrap the target molecule. Amongst these, the use of noble metal nanostructures surfaces has gained particular interest for their superior Raman signal enhancement and stability [28, 29]. One important characteristic in this particular matrix is that the biomarker gets positioned within a few nanometers of the metal surface, obtaining dramatic scattering cross-section enhancement [30, 31]. Amongst noble metals, gold is an enhancing surface at long-wavelength excitation due to their special optical properties, absorption and scattering bands, making them ideal candidates for the fabrication of bio-imaging sensors [32- 33]. Further, gold has proven to be biocompatible, less cytotoxic, and can be modified with thiols and disulfides [22], allowing covalent attachment of the biomolecule on the surface for a more robust and stable immunoassay.

Due to their specificity, speed, portability and low cost, biosensors offer exciting opportunities for numerous decentralized clinical applications. Current worldwide efforts are focused on the development of biosensors for clinical applications, such as for the early detection of cancers such as prostate cancer; consequently, the discovery of effective ways to immobilize antibodies is essential. However, for a biosensor to be used as a diagnostic device in a clinical setting some limitations have to be addressed, i.e. sensitivity, selectivity and stability as well as high overpotential at which the electron transfer process occurs [36]. Recent developments in nanomaterials and nanotechnologies are opening new alternatives for improving these parameters for the development of efficient clinical biosensors [37].

Taking the advantage of progress in nanotechnology for developing highly sensitive, selective and stable biosensors, enzyme-linked immunosorbent assays (ELISA) have served as the workhorse for clinical protein determinations, with detection limit (DL) as low as 3 pg mL⁻¹ for protein biomarkers [37-41] ELISA suffers limitations in analysis time, sample size, and impossibility of simultaneous measurement of collections of proteins.

Electrochemiluminiscense has been proven to have very good DL for proteins but require relatively expensive instruments for automated analyses [40-43].

The optimum SERS excitation wavelength is dependent on the chemical/physical properties of the enhancing substrate and not the photophysics of the scatterer, facilitating multilabel readout by requiring only one excitation wavelength. Raman responses are much less susceptible to photobleaching than fluorescence, enabling the use of extended signal averaging to lower detection limits.

The main goal of this work is to demonstrate a highly sensitivity, and accurate tool for detection of PSA cancer employing Au coated SiO₂ nanowires in a SERS-based immunoassay.

8.3 Materials and Methods

Mouse anti-human prostate specific antigen and PSA antigen were purchased from AbD serotec. Bovine serum albumin (BSA) was purchased from Sigma-Aldrich Chemical Co. dithiobis succinimidyl propionate (DTSP) was obtained from Fischer Scientific. Silica nanowires were prepared by ion-implanted seeding approach, method as described elsewhere [12, 13]. Deposition SiO₂ NWs were performed by a homogeneous stock solution of 0.2

mg/mL silica nanowires in water containing 10 mM nickel chloride (NiCl_2) was kept by overnight sonication. Fabrication SiO_2 NWs was carried onto the 0.5 x 0.5 cm gold surface using electrophoretic deposition. For SiO_2 NWs deposition 80 μL of the stock solution was added to 2 mL of acetonitrile were employed as the working, counter and reference electrode respectively, sonicated 1 min followed by apply a step potential of 100 V for 60 s.

The gold surface was modified using 2 mg/mL solution of DTSP via Self Assembled Monolayer (SAM) formation, which was then modified for Anti-PSA binding. The binding was achieved by applying 30 μL of a 5 $\mu\text{g}/\text{mL}$ solution of PSA antibody and incubating at 4 $^\circ\text{C}$ (overnight). The Anti PSA modified electrode was later blocked with 1% BSA to prevent nonspecific binding.

Surface Activation for SERS were carried with a deposition of 60 nm on thick gold film employed an e-beam to deposition. Surface morphology and the PSA detection was performed using scanning (Hitachi S4800 SEM) and Microraman (Renishaw) spectroscopy was done using 632 nm Ar laser with 3 accumulations of 10 s exposure.

8.4 Results and discussion

Transmission electron microscopy (TEM) images are shown Figure 58, with random growing direction of the silica nanowires with average diameter between 50 to up 90 nm.

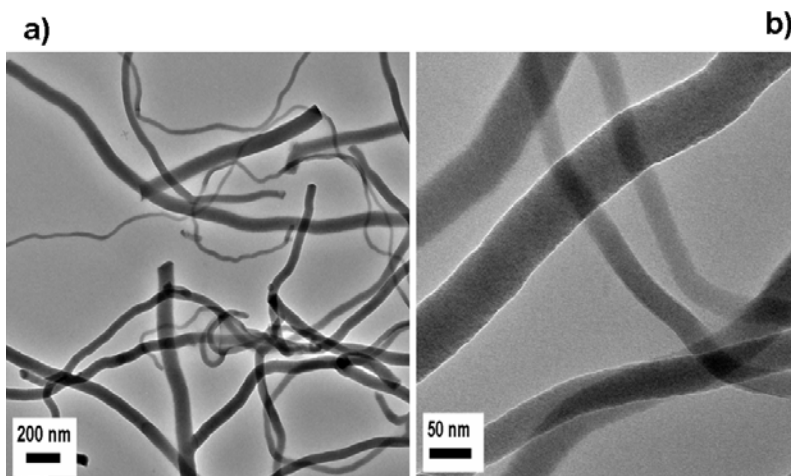


Figure 58. SEM micrographs of gold coated on silica nanowires (A) For SiO₂ NWs deposition 80 μL of the stock solution was added to 2 mL of acetonitrile, sonicated 1 min followed by apply a step potential of 100 V for 60 s. (B) Higher-magnification image clearly indicating the average diameter size for SiO₂ NWs is of 50 nm.

A broadening peak around 21 in the 2θ angle (44) evidenced the nature of the silica deposit; the average crystallite size, estimated by the Scherrer's equation, was around 4.0 nm.

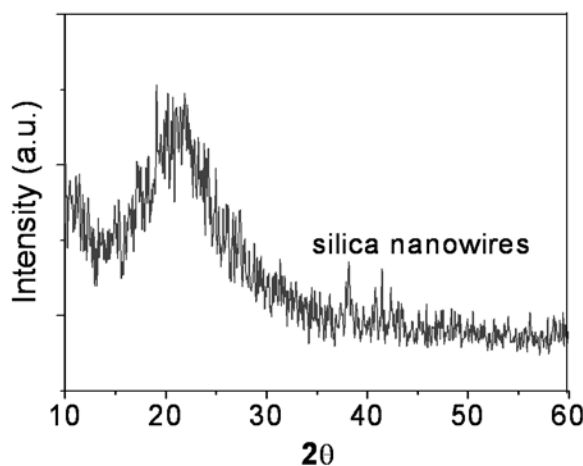


Figure 59. High ResolutionTEM micrographs of gold coated on silica nanowires (A) For SiO₂ NWs deposition 80 μL of the stock solution was added to 2 mL of acetonitrile, sonicated 1 min followed by application of a step potential of 100 V for 60 s. (B) Higher-magnification image clearly indicating the average diameter size for SiO₂ NWs is of 50 nm to 90 nm.

The capture antibody substrate consisted of anti-free PSA bound to gold-coated SiO₂ NWs surfaces via DSTP. PSA peak values at different concentrations of PSA were immobilized and its spectra recorded. On the next figure (Figure 60), the increasing concentration of PSA corresponds to a change in intensity for the peaks at 991, 1170, 1377, 1577 and 2143 cm⁻¹. For Raman bands these changes are significantly notable and consistent with those found in Table 3. [45]

Table 9 Band assignments for SER spectra for the epitope in the PSA molecule. Three residues of amino acids on Au-coated ZnO NRs are most important.

Asparagine Histidine 87 Cyst42			Proposed band assignment
Asn Cyst58			
Normal Raman			SERS
929	931	930	911
1140	1080	1140	1170
1356	1360	1344	1377
1615	1482	1411	1577
			C-COO str.
			NH ₃ ⁺ def.
			CH ₂ sciss, CH bend
			CO str.

Str: stretching; def: deforming; bend: bending, sciss, scissoring

Human prostate specific antigen (PSA or human kallikrein related peptidase KLK3) from seminal fluid is a sandwich complex with two monoclonal antibodies (mAbs). mAb 5D5A5 capture total PSA with exceptional high affinity [46]. The mAb 5D5A5 epitope consist of three stretches of PSA residues: Asn 61 to His87 and the main epitopic segment via disulfide between Cyst42 and Cyst 58 [47].

Although the SERS studies referenced above have identified a series of amino acids for PSA epitope, its side could maintain the bonding between mAbs and PSA. It is difficult to understand the SERS value of such cooperation between the antigen and the antibody, but it is suggested to conduct a study of computational vibration modes to predict more accurately the vibrational modes in the epitope.

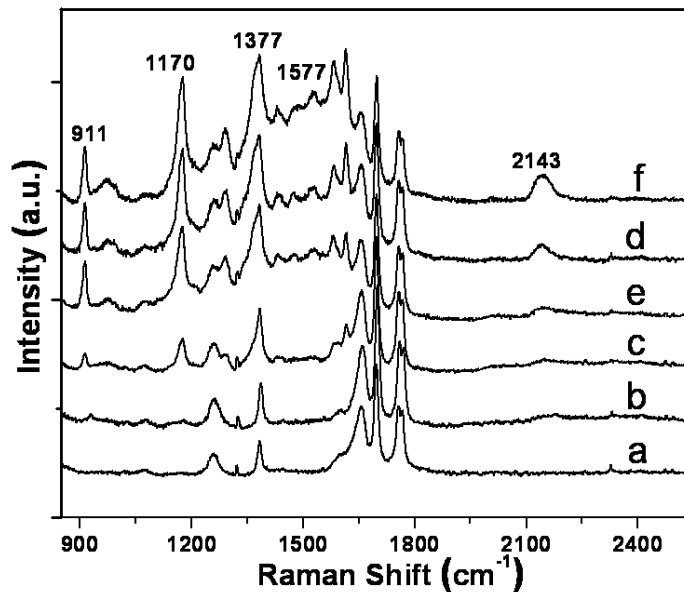


Figure 60. Gold-coated SiO₂ NWs demonstrating that the substrate is active for SERS implementation. a) antibody. b) blocked with 1% BSA. c) 1 pg/mL PSA. d) 1 ng/mL PSA. e) 50 ng/mL PSA. f) 50 ng/mL PSA. PSA spectra were acquired at 3 scans, 10 s integration time using a laser wavelength of 632 nm.

8.5 Conclusions

SERS experiment tested the relative binding affinity of gold-coated SiO₂ NW surfaces using DSTP. The SERS data showed the anti-PSA was detected at concentrations as low as 12 pg/mL.

8.6 REFERENCES

- [1] Y.E. Choi, J.W. Kwak, J. W. Park, Nanotechnology for Early Cancer Detection, *Sensors*, **10** (2010) 428
- [2] D. S. Grubisha, R. J. Lipert, H.Y. Park, J. Driskell, M. D. Porter, *Anal. Chem.* **75** (2003) 5936
- [3] H. K. Seo, W. J. Hong, D. H. Kang, S. R. Ryu, Y. M. Jung, *Bull. Korean. Chem. Soc.* **31** (5) (2010) 1215
- [4] K. G. Lee, R. W. Muhammad, T. J. Park, Jaebeom Lee, Sang Yup Lee, and Do Hyun Kim. *ACS Nano*, **4** (7) (2010) 3933.
- [5] L. Chen, L. Luo, Z. Chen, Zhang. M. Zapien, Ch. Lee, *J. Phys. Chem. C*, **114** (2010) 93
- [6] R. Ménez, M. Sandrine, B. Muller, M. Bossus, F. Ducancel, J. Colette, E. Stura. *J. Mol. Biol.* **376** (2008) 1021.
- [7] Z. Takai, Y. Doi, Y. Yamauchi, K. Kuroda. *J. Phys. Chem. C*, **114** (2010) 7586.
- [8] D. S. Grubisha, R. J. Lipert, H-Y. Park, J. Driskell and M. D. Porter, *Anal. Chem.* **75** (2003) 5936.
- [9] W. Lu, A. K. Singh, S. A. Khan, D. Senapati, H. Yu and P. C. Ray, *J. Am. Chem. Soc.* **132** (2010) 18103.
- [10] G. Wang, H-Y. Park and R. J. Lipert. *Anal. Chem*, **81** (2009) 9643
- [11] T. Suzuki, M. Hirokatsu, N. Takashi, K. Kazuyuki, *J. Phys. Chem. C*, **112** (2008) 1831
- [12] P. K. Sekhar, N. S. Ramgir , Shekhar. B, *J. Phys. Chem. C*, **112** (2008) 1729
- [13] K. Praveen, B. Shekhar. B, *Materials Letters*, **64** (2010) 729.
- [14] Y. Wang, A. Brunsen, U. Jonas, J. Dostálek and W. Knoll, *Anal. Chem.* **81** (2009) 9625

- [15] M. Woo, S.M. Lee, G. Kim, J. Baek, M.S. Noh, J.E. Kim, S.J. Park, M.H. Cho, *Anal. Chem.* 81 (2009) 1008
- [16] A.S. Liu a, B.X. Zhang, A.Y. Wu a, Y, L. He , *Clin. Chim. Acta.* 395 (2008) 51
- [17] P. Sarkar, P. Pal, D. Ghosh, S. Setford, I. Tothill. *Int. J. Pharm.* 238 (2002) 1
- [18] J.H. Kim, J.S. Kim, H. Choi, S. M. Lee, B.H. Jun, K.N. Yu, E. Kuk, Y.K Kim, D. H. Jeong, M.H. Cho, Y.S. Lee, *Anal. Chem.* 78 (2006) 6967
- [19] K. E. Shafer, C. L. Haynes, M. R. Glucksberg, R. P. Van Duyne, *J. Am. Chem. Soc.* 125, (2003) 588
- [20] D. Graham, K. Faulds, D. Thompson, F. McKenzie, R. Stokes, C. Dalton, R. Stevenson, J. Alexander, P. Garside and E. McFarlane, *Biochem. Soc. Trans.* 37 (2009) 697
- [21] J. D. Driskell, K. M. Kwart, R. J Lipert, M. D. Porter, J. D. Neill, J. F. Ridpath, *Anal. Chem.* 77 (2005) 6147
- [22] H. Lilja, H, A. Christensson, U. Dahlen, M. Matikainen, O. Nilsson, K. Pettersson, T. Lovgren, *Clin. Chem.* **37**, 161 (1991) 8
- [23] V. Mani, B. Chikkaveeraiah, V. Patel, J. Gutkind, J. Rusling, *ACS Nano* (2009) 585
- [24] T. J. Polascik, J. E. Oesterling, A.W. Partin, *J. Urol.* 162 (1999) 293
- [25] Sun, Z. *Appl. Phys. Lett.* 91 (2007) 221106
- [26] A. Ward, J. Catto, F. Hamdy. *C. Ann. Clin. Biochem.* (2001) 38
- [27] Chen, L.; Luo, L.; Chen, Z.; Zhang, M.; Zapien, J.; Lee, Ch and Lee, S. *J. Phys. Chem. C*, **114** (2010) 93
- [28] C. L. Haynes, A.D. McFarland, R. Van Duyne, **77** (2005) 338 A.
- [29] M. Bruchez, J. Moronne, P. Gin, P, P. Weiss, A.P. Alivisatos, W.Chan, S. Nie, *Science*, **281** (1998) 2016

- [30] K. Yang, CH, She, H, Wang, X. Ou, X. Zhang. C.H. Lee, CH, S. Lee. S. *Phys. Chem. C*, 113 (2009) 20169
- [31] C.H. Sun, S. Kai, J. Valentine, J. Bauza, J. Ellman, O. Elboudwarej, B. Mukherjee, C.H Craik, M. Shuman. F. Chen, X. Zhang. *ACS Nano* **4** (2) (2010) 978.
- [32] T. Yu Liu, *Langmuir*. **22** (2006) 5804.
- [33] X. Wang, *J. Phys. Chem. C*. **111** (2007) 3836
- [34] L. Chen, L. Luo, Z. Chen, M. Zhang, J. Zapien, Ch. Lee, S. Lee, *J. Phys. Chem. C*, 114 (2010), 93
- [35] CH. Ching, *Chemical Physical Letter*. 404 (2005) 30
- [36] G.T Hermanson, A.K. Mallia, P.J. Smith, Techniques, Academic Press Inc. (1992), 59.
- [37] S. Ordonez, E. Fabregas, E. *Biosens. Bioelectron* 22 (2007) 965
- [38] W. C. Chan, S. Nie, S. Science 281 (1998) 2016.
- [39] H. Lilja, H, D. Ulmert, A. Vickers, J. Nat. Rev. Cancer 8 (2008) 268
- [40] Z. Dai, F. Yan, J. Chen, H. X Ju, *Anal Chem*. 75 (2003) 5429
- [41] A. Ward, J. Catto, F. Hamdy, *Ann. Clin. Biochem*. (2001) 38
- [42] J. Lin, F. Yan, X. Hu, H.X. Ju. *J. Immunol Methods*. 291(2004) 165
- [43] A. M. Ward, J. Catto, F. Hamdy, *Ann. Clin. Biochem*. 38 (2001) 633
- [44] G. K. Lee, R. Wi, M. Imran, T. J. Park, J. Lee, S. Y. Lee, D. H. Kim. *Nano*, 4 (2010) 3933
- [45] S. Stewart. P.M Fredericks, *Spectrochimica Acta Part A* 55 (1999) 1641.
- [46] W. Zhang, J. Leinonen, N. Kalkkinen, B. Dowell, U. Stenman, *Clin. Chem*. 41, (1995), 567

[47] E. Sutra, B.Muller, M.Bossus, S. Michael, C. Jolivet, F. Duncancel. *J.Mol. Biol.* 414, (2011), 530.